

ABSTRACT

Title of dissertation: CATASTROPHE MODEL FOR
THE ONSET OF FAST
MAGNETIC RECONNECTION

Paul Adam Cassak
Doctor of Philosophy, 2006

Dissertation directed by: Professor James Drake
Department of Physics

Solar flares, magnetic substorms and sawtooth crashes in fusion devices are explosive events in which magnetic reconnection facilitates the rapid release of energy stored in stressed magnetic fields into the surrounding plasma. Much effort has gone into understanding how the energy is released so fast. Collisional (Sweet-Parker) reconnection, based on resistive magnetohydrodynamics (MHD), is a successful physical model but is far too slow to explain observed energy release rates. In collisionless (Hall) reconnection, dispersive waves introduced by the Hall effect lead to energy release rates fast enough to explain observations. However, the steady-state description does not address why reconnection is explosive. We present a fully nonlinear model for the dynamics of magnetic reconnection. Using scaling arguments and resistive Hall-MHD numerical simulations, we show that the Sweet-Parker solution only exists when the current sheet is thick enough, while the Hall solution only exists when the resistivity is small enough. Furthermore, we show that reconnection is bistable, *i.e.*, both the Sweet-Parker and Hall solutions can exist for the same set

of control parameters. The disappearance of steady-state solutions as a control parameter varies is interpreted as a saddle-node bifurcation. Three signatures of this model are verified with numerical simulations, including the existence of a heretofore unidentified unstable steady-state reconnection solution. We present a theoretical model motivating that the existence of saddle-node bifurcations is intimately related to the presence of dispersive waves caused by the Hall effect.

This result has a potentially profound impact on the long-standing “Onset Problem”, *i.e.*, explaining how large amounts of free magnetic energy can be stored for a long time before being explosively released. During Sweet-Parker reconnection, magnetic energy accumulates because the energy release is very slow. When the thickness of the current sheet decreases past a critical value, the Sweet-Parker solution catastrophically disappears, causing a sudden transition to Hall reconnection which begins the fast release of the stored energy. We delineate scenarios for the catastrophic onset of Hall reconnection and discuss the impact of this model on observations of magnetic explosions, showing in particular that it is consistent with observations of reconnection events in the solar corona.

CATASTROPHE MODEL FOR THE ONSET
OF FAST MAGNETIC RECONNECTION

by

Paul Adam Cassak

Dissertation submitted to the Faculty of the Graduate School of the
University of Maryland, College Park in partial fulfillment
of the requirements for the degree of
Doctor of Philosophy
2006

Advisory Committee:

Professor James F. Drake, Chair/Adviser

Professor Thomas M. Antonsen Jr.

Senior Research Scientist Parvez N. Guzdar

Associate Professor Eve Ostriker

Visiting Assistant Professor Michael A. Shay

© Copyright by
Paul Adam Cassak
2006

Dedication

This thesis is dedicated to three very special people.

To Bill Dorland, whose accomplishments in Physics are matched only by his efforts outside of Physics, overcoming adversity and giving of himself at the same time. He is an inspiration to us all.

To my mother, Kit Cassak, who has given of herself completely to the well-being of her children. She has given me every opportunity to succeed, and is supportive of my efforts whether I succeed or not. She has instilled in me the importance of being educated and of educating others.

Finally, to my wife, Julie Bryan, who has selflessly sacrificed so much of herself to help my career. She has been there for me through good times and bad, encouraging me and being supportive all the while. She has taught me as much about life as anybody ever has, and keeps me smiling.

May this dedication be a small contribution toward the honors you deserve.

Acknowledgments

I am grateful to the incomparable Jim Drake and Mike Shay for their support and patience. They have given me the gift of knowledge, which can never be taken away. I would like to thank Jan Egedal, Ed Lazarus, and Dana Longcope for providing data used in the thesis. I have benefited from helpful discussions with Bill Dorland, Bruno Eckhardt, Parvez Guzdar, Bob Kleva, and Marc Swisdak. I thank Spiro Antiochos, Amitava Bhattacharjee, Allen Flora, Jim Klimchuk, and Misha Sitnov for their advice, and Thomas Antonsen and Eve Ostriker for sitting on my committee.

Thanks to my past advisers for everything they did for me to get me to this point: Stephen Kukolich, Brian Drouin, Michael Shupe, Baha Balantekin, Leslie Smith, and Thanos Tzavaras. To my past coworkers - Pollyanna Wikrent, Jon Fetter, Armando Aleixo, the late Marco Ribeiro, Magda Gonzalez, and Brian Jemella, my present co-workers Haihong Che, Kevin Schoeffler, Yi-Hsin Liu, Ray Fermo, and Andrey Divin, and my colleagues past and present Ram Sriharsha, Carlo Oleari, Jason Crain, Amihan Heusmann, Joe Sylvester, Sheung Wah Ng, Andy Tillotsen, Jon Palastro, Kyle Gustafson, Michael Barnes, Ingmar Broemstrup, Tomo Tatsuno, George Stantchev - thank you for making the educational experience truly educational. The staff at IREAP, Mohini, Janet, Nancy, Dottie, Margaret, Janice, and Carol, and the staff at Physics, Jane and Linda, have been great. Computer guru Ed Condon has bailed me out many times. Special thanks to Nick Chant for “taking a chance” on me.

My love goes out to my family - Julie, Mom, Pop and Georgia, Todd and Emma, “Dad Sir” and Diane, the Bryan brothers and their families - for their support. I also thank my friends - Eric Bycer, Brian Gilbert, Jason Zuffranieri, Keith Aspinall, Damian Schumm and especially Jason Posey and Andrew Klein, two of the most loyal friends a guy could ask for.

Finally, I would like to thank four very special people whose friendships have influenced me more than they probably realize. Just by being themselves, they have inspired - and continue to inspire - me to be a better person. Their friendships mean more to me than I could ever tell them in person. To Tony Gerig, Ayush Gupta, Andy Plumb, and Murali Yeddulla, I offer you my sincerest gratitude for touching my life in the ways you have. Thank you.

Table of Contents

List of Figures	vii
1 Introduction	1
1.1 Magnetic Reconnection: Early History and Applications	1
1.2 Statement of the “Onset Problem”	10
1.3 Summary of Results	12
1.4 Observations of Magnetic Reconnection Onset	15
1.4.1 Onset of Solar Eruptions	15
1.4.2 Onset of Magnetic Substorms	18
1.4.3 The Sawtooth Crash	20
1.4.4 Spontaneous Onset in a Laboratory Plasma	21
1.4.5 Summary	22
2 Magnetic Reconnection in the Steady-State	23
2.1 The Physics of Magnetic Reconnection	23
2.1.1 How Magnetic Energy Is Released	24
2.1.2 How Magnetic Topology Changes	25
2.1.3 Putting It Together - How Reconnection Persists	28
2.1.4 Analytical Treatment	29
2.2 Collisional (Sweet-Parker) Reconnection	32
2.3 Collisionless (Hall) Reconnection	35
2.3.1 Anti-parallel Hall Reconnection	40
2.3.2 Component Hall Reconnection	44
2.4 Magnetic Reconnection and Linear Wave Analysis	48
2.4.1 Linear Waves in MHD	50
2.4.2 Linear Waves in Hall-MHD	52
2.4.3 Linear Waves in Hall-MHD with a Strong Guide Field	55
2.4.4 The Relation of Dispersive Waves to Fast Reconnection	59
2.5 Summary	61
3 Dynamics of Magnetic Reconnection	63
3.1 Validity Conditions of Steady-State Reconnection Models	64
3.2 Bistability and Hysteresis of Magnetic Reconnection	67
3.3 Description of Numerics	70
3.4 Numerical Simulations of Bistability	74
3.4.1 Anti-parallel Reconnection	74
3.4.2 Component Reconnection	81
3.5 Experimental Results from Magnetic Reconnection Experiment (MRX)	86
3.6 Summary	86

4	Nonlinear Dynamics of Magnetic Reconnection	88
4.1	Bifurcation Model of Magnetic Reconnection Dynamics	89
4.2	Additional Predictions of the Bifurcation Model	91
4.2.1	Time Evolution of the Current Sheet Thickness	91
4.2.2	The Transition Time From Sweet-Parker to Hall Reconnection	92
4.3	Simulation Results	93
4.3.1	Time Evolution of the Current Sheet Thickness	94
4.3.2	The Transition Time from Sweet-Parker to Hall Reconnection	96
4.3.3	The Unstable Steady-State Reconnection Solution	97
4.4	Linear Properties of the Unstable Solution	103
4.5	Summary	106
5	Toward an Analytical Theory	107
5.1	Dynamical Model of Magnetic Reconnection	108
5.2	Existence of Saddle-Node Bifurcations	113
5.3	Linear Analysis	114
5.3.1	Sweet-Parker Regime	114
5.3.2	Hall Regime	115
5.4	Comparison to Numerical Results	117
5.5	Summary	120
6	Catastrophic Onset of Fast Magnetic Reconnection	121
6.1	Conditions Under Which a Transition Occurs	122
6.2	Spontaneous Onset Simulation Results	126
6.3	Observational Evidence for Spontaneous Catastrophic Onset	130
6.3.1	Spontaneous Onset at the Versatile Toroidal Facility (VTF)	131
6.3.2	Flux Emergence Reconnection in the Solar Corona	131
6.4	Applications To Reconnection Events in Nature	132
6.4.1	Onset of Solar Eruptions	133
6.4.2	Self-Organized Criticality Models of the Solar Corona	137
6.4.3	Onset of the Sawtooth Crash	138
6.4.4	Onset of Magnetic Substorms	139
6.5	Summary	139
7	Summary and Limitations	140
7.1	Summary of Results	140
7.1.1	The Dynamics of Magnetic Reconnection	141
7.1.2	The Onset Problem of Magnetic Reconnection	142
7.2	Limitations of the Model	143
A	The Tearing Mode - A Primer	145
A.1	Physics of the Resistive Tearing Mode	145
	Bibliography	154

List of Figures

1.1	A solar flare with an erupting prominence.	2
1.2	Sweet’s model of a solar flare.	3
1.3	The Sweet-Parker and Petschek configurations.	4
1.4	Reconnection in the Earth’s magnetosphere.	7
1.5	The sawtooth crash.	9
1.6	Schematic representation of a two ribbon solar flare.	17
1.7	X-ray light curve during a solar flare.	18
1.8	Auroral electrojet index during a magnetic substorm.	19
1.9	Current and voltage during a spontaneous reconnection event at VTF.	22
2.1	“Squashed bubble” model of magnetic energy release.	24
2.2	Canonical reconnection geometry.	27
2.3	Reconnection geometry with a guide field.	28
2.4	Two scale structure during Hall reconnection.	38
2.5	Quadrupolar out of plane magnetic field during Hall reconnection.	40
2.6	Quadrupolar density configuration during component Hall reconnection.	45
2.7	Motivation of role of waves in mediating outflow.	49
2.8	Dispersion relation for Hall-MHD waves with no guide field.	54
2.9	Dispersion relation for Hall-MHD waves with a large guide field.	58
2.10	Correlation between dispersive waves and fast reconnection.	60
3.1	Schematic bifurcation diagram for reconnection.	69
3.2	Initial double tearing mode configuration used in the simulations.	72
3.3	Simulation results showing bistability of anti-parallel reconnection.	76

3.4	Current sheet profiles for Hall and Sweet-Parker configuration with same parameters during anti-parallel reconnection.	77
3.5	Bifurcation diagram for anti-parallel reconnection from results of numerical simulations.	79
3.6	Simulation results demonstrating hysteresis.	80
3.7	Simulation results demonstrating bistability of component reconnection.	82
3.8	Current sheet profiles for Hall and Sweet-Parker configuration with same parameters during component reconnection.	83
3.9	Bifurcation diagram for component reconnection from results of numerical simulations.	84
4.1	Schematic phase portrait for reconnection.	89
4.2	Bifurcation diagram of phase portrait in Fig. 4.1.	90
4.3	Schematic phase portrait showing ghost and bottleneck behavior.	92
4.4	Simulation results of the evolution of current sheet thickness during transition to Hall reconnection.	94
4.5	Simulation results for phase portrait during transition to Hall reconnection.	95
4.6	Simulation results of the transition time scaling with resistivity.	96
4.7	Schematic diagram of iteration scheme to find the unstable solution.	98
4.8	Process for getting initial conditions for iteration scheme.	99
4.9	Simulation results of iteration scheme to find unstable reconnection solutions.	100
4.10	Current sheet profile of the unstable solution.	102
4.11	Simulation results showing exponential growth of a perturbation to the unstable solution.	104
4.12	Simulation results of the structure of the most unstable eigenmode of the unstable solution.	105
5.1	Test of analytical model using simulation data.	110

5.2	Relevant quantities for the analytical model.	111
5.3	Phase portrait of analytical model.	118
6.1	Schematic diagram of two possible onset mechanisms.	123
6.2	Model for the spontaneous catastrophic onset of fast magnetic reconnection.	125
6.3	Simulation results showing spontaneous catastrophic onset of fast magnetic reconnection.	127
6.4	Current sheet at early and late times for spontaneous onset simulations.	129
A.1	Harris sheet equilibrium.	146
A.2	Outer solution of tearing mode for various Δ'	151

Chapter 1

Introduction

1.1 Magnetic Reconnection: Early History and Applications

The development of the theory of magnetic reconnection began in the middle of the 20th century, sparked by attempts to understand solar flares. Solar flares, first reported independently by Carrington and Hodgson in 1859 [Carrington, 1859, Hodgson, 1859], are enormous bursts of radiation often accompanied by the ejection of a large amount of material from the solar atmosphere, or “corona”, as shown in Fig. 1.1. Large flares release up to 10^{32} ergs (the equivalent of 40 *billion* atomic bombs) over a time span of about 2 to 20 minutes. Many excellent reviews of evidence for reconnection in the solar corona (see section 10.6 of [Aschwanden, 2005]) and solar flare modeling ([Priest and Forbes, 2002, Lin et al., 2003] for example) have been written.

Where does all the energy released by the solar flare come from? As emphasized by Priest and Forbes [Priest and Forbes, 2002], it must come from the Sun’s magnetic field. With coronal densities and temperatures of $n \sim 3 \times 10^9 \text{ cm}^{-3}$ and $T \sim 10^6 \text{ K}$ and tubes of length $H \sim 10^{10} \text{ cm}$ and radius $L \sim 10^9$, the thermal ($n\pi L^2 HT \sim 10^{28} \text{ erg}$) and gravitational ($mgh \sim m_H n\pi L^2 H g_\odot R_\odot \sim 10^{28} \text{ erg}$) energy content are inadequate¹. However, an active region magnetic field of $B \sim 100 \text{ G}$

¹Here, m_H is the mass of a hydrogen atom, g_\odot is the acceleration due to gravity at the solar

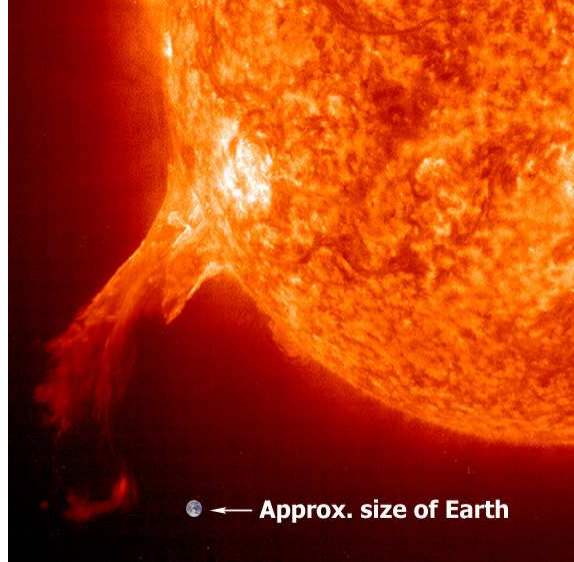


Figure 1.1: A solar flare with an erupting prominence, with the Earth inset for scale. Image taken on July 1, 2002. Courtesy of SOHO/EIT consortium. SOHO is a project of international cooperation between ESA and NASA.

has energy content $B^2\pi L^2 H/8\pi \sim 10^{31}$ erg, close to the amount released during a large solar flare.

How is this magnetic energy liberated? A first guess might be magnetic diffusion, but the time it would take to diffuse away the magnetic field (based on a classical resistivity of $\eta \sim 2 \times 10^{-16}$ s; see Sec. 1.4.1) would be $\tau_R \sim 4\pi L^2/\eta c^2 \sim 7 \times 10^{13}$ s, *i.e.*, about 2 million years, much longer than the observed few minutes!

The first step toward a solution came when Ron Giovanelli [Giovanelli, 1947] observed that solar flares always occur in regions where the magnetic field has a null point, *i.e.*, the magnetic field changes directions. Giovanelli discussed the problem with the famous astronomer Fred Hoyle [Hoyle, 1949], who gave it to his gradu-

surface and R_\odot is the radius of the sun.

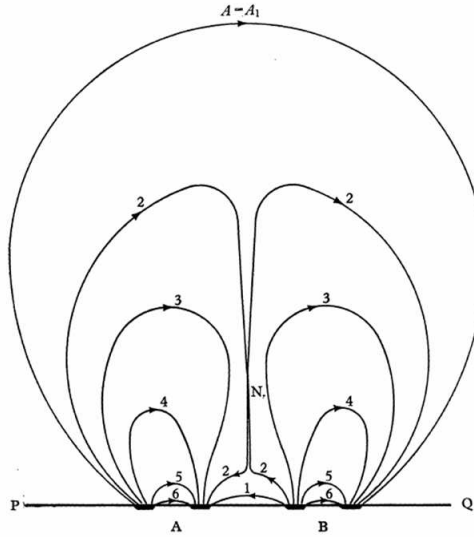


Figure 1.2: Sweet's model of a solar flare via magnetic reconnection. A long, thin current sheet forms when two bipolar regions (A and B) come together, squeezing plasma out from the ends. More modern solar flare models will be discussed in Sec. 6.4.1. Reprinted with permission from Ref. [Sweet, 1958]. ©1958, International Astronomical Union, Cambridge University Press.

ate student James Dungey. Dungey studied the properties of oppositely directed magnetic fields and showed that magnetic field lines would break apart and cross connect due to diffusion, forming a thin current sheet [Dungey, 1953, Dungey, 1958], a process he later dubbed magnetic reconnection.

The first self-consistent model of magnetic reconnection came soon after, when in 1956, Peter Sweet presented a paper [Sweet, 1958] at a conference which modeled a solar flare as the approach of two bipolar magnetic field configurations as shown in Fig. 1.2. As the bipolar regions come together, oppositely directed magnetic fields are driven together, where Dungey's diffusive reconnection occurs (at the point labeled N in Fig. 1.2). Sweet said that the external forcing would cause the plasma to

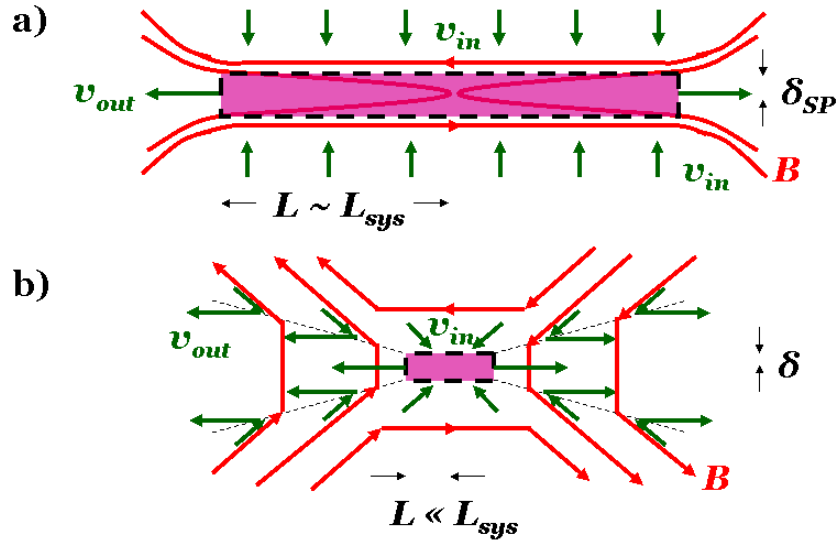


Figure 1.3: (a) Current sheet configuration and flow pattern in the Sweet-Parker and (b) Petschek models of magnetic reconnection. The purple box denotes the dissipation region where field lines break apart and cross connect.

be ejected from the ends of the current sheet, thereby converting the magnetic energy into plasma flows². The key point is that without reconnection to break the field lines, the plasma could not be ejected. Eugene Parker saw Sweet's talk and, on the way home from the conference, performed a steady-state scaling analysis of Sweet's mechanism [Parker, 1957] using the theory of resistive magnetohydrodynamics. This is the so-called Sweet-Parker model of collisional reconnection and it predicts a much faster energy release time than diffusion alone (of about 10^7 s - about four months - as we show in Sec. 2.2), but is still far too slow to explain the observed few minutes.

²Sweet's picture of reconnection caused many to believe that reconnection *only* occurs due to external forcing, a belief held by some in the solar physics community even today. That reconnection actually needs no external driving is discussed in Sec. 2.1.2.

Following the failure of Sweet-Parker reconnection to explain the energy release during a solar flare, various attempts to alter the Sweet-Parker model were made [Parker, 1963]. Undoubtedly, the most important contribution was due to Harry Petschek, who presented a model [Petschek, 1964] in which the long, thin (Y-type) Sweet-Parker current sheet (see Fig. 1.3a) is replaced by an open (X-type) configuration with a microscopic Sweet-Parker layer in the center (see Fig. 1.3b). The conversion of magnetic energy chiefly takes place due to standing slow shock waves outside the Sweet-Parker layer rather than diffusion inside it. This mechanism can proceed much faster than Sweet-Parker reconnection because only a small fraction of the plasma must go through the collisional region. Indeed, it was shown to be fast enough to explain the energy release rate observed in solar flares. This agreement led many to believe that the problem was solved. Unfortunately, it was discovered some 20 years later in numerical simulations by Dieter Biskamp [Biskamp, 1986] that a microscopic Sweet-Parker layer is not capable of supporting this open outflow geometry unless the resistivity is spatially non-uniform [Sato and Hayashi, 1979, Ugai and Tsuda, 1977, Scholer, 1989]. Attempts to explain why the resistivity in a collisional plasma is locally enhanced have not been completely successful. In collisionless plasmas, such as the Earth's magnetotail, there has been progress, with the onset of microinstabilities at small length scales, such as the lower hybrid drift instability [Huba et al., 1977] or Buneman instability [Drake et al., 2003], causing anomalous resistivity. However, in collisional plasmas such as the solar corona, no such progress has been made. It has been suggested that turbulence leads to enhanced resistivity, but the question remains open.

An unexpected breakthrough came when non-magnetohydrodynamic effects on reconnection were considered. The Hall effect, which describes the decoupling of ions from electrons, was studied [Sonnerup, 1979, Terasawa, 1983, Hassam, 1984]. Subsequent theoretical and numerical studies have found that the rate of energy release during Hall reconnection is fast enough to explain observed energy release times [Aydemir, 1992, Mandt et al., 1994, Horiuchi and Sato, 1994, Biskamp et al., 1995, Ma and Bhattacharjee, 1996, Shay et al., 1998, Birn et al., 2001, Shay et al., 2001]. The key to the rapidity of Hall reconnection is the existence of dispersive waves due to the Hall effect, which leads to the Petschek open outflow configuration [Mandt et al., 1994, Rogers et al., 2001]. This is important because it provides an explanation for why reconnection is so fast without invoking anomalous resistivity; it is entirely self-consistent. We discuss Hall reconnection further in Chapter 2.

Reconnection is not only relevant to solar flares. Dungey [Dungey, 1961] suggested that a similar process happens in the Earth's magnetosphere, as depicted in Fig. 1.4. The Earth's magnetic dipole field (in green) points northward at the equator. When the solar wind (in yellow) convects in an interplanetary magnetic field (in blue) with a component pointing southward, the fields will be oppositely directed and break and cross connect (at the gray box at the magnetopause). These "open" field lines (in red) are dragged by the solar wind over the poles and stretch out on the night side of the Earth, where they are again oppositely directed. When brought close enough to each other (in the gray box in the magnetotail), they cross connect again (hence *reconnecting*), causing a so-called magnetic substorm. Plasma is ejected toward the Earth and is deflected by the Earth's magnetic field (in green)

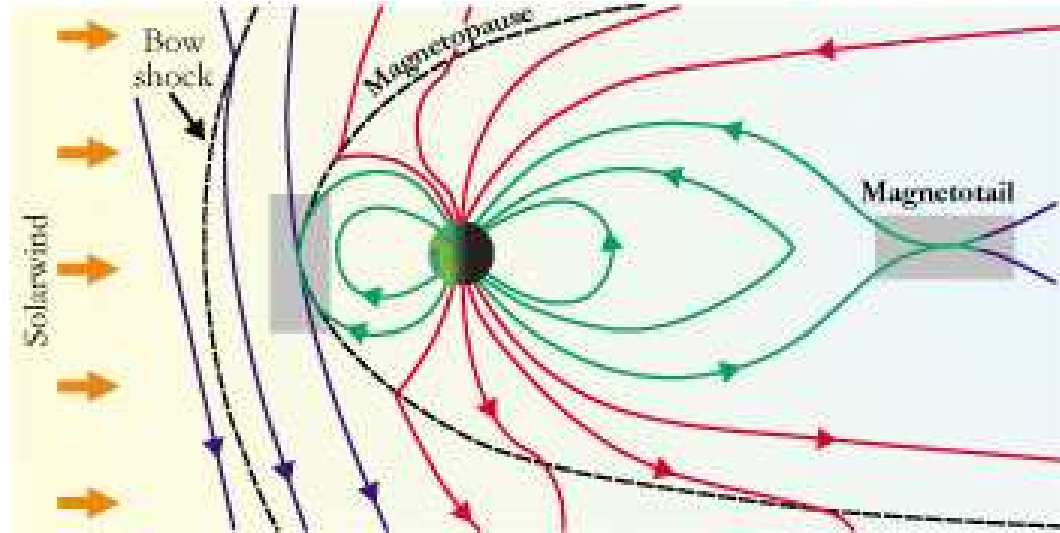


Figure 1.4: Schematic representation of magnetic reconnection in the Earth's magnetosphere, leading to a magnetic substorm. Reprinted with permission from C. Day, *Physics Today*, Vol. 54, Issue 10, pg. 16, 2001. Copyright 2001, American Institute of Physics.

toward the poles, which causes the auroral lights. This model was not widely accepted for nearly 20 years until terrestrial and satellite observations confirmed it. See [Kivelson and Russell, 1995, McPherron, 1999, Shay, 1998, Priest and Forbes, 2000] for reviews.

Reconnection is also thought to be a key ingredient in the so-called “coronal heating problem”, which asks why the temperature of the solar corona is ~ 100 times hotter than the chromosphere, the “crust” of the sun which produces the light seen at Earth (see [Klimchuk, 2006] for a review). It was suggested by Parker [Parker, 1983, Parker, 1988] that the same mechanism producing large flares also produces many small scale “nanoflares”, which release $\gtrsim 10^{24}$ erg each, and that the net effect of them is enough to heat the corona. Studies of the statistics of solar flares show

power law behavior over many orders of magnitude (see [Charbonneau et al., 2001] for a review), suggesting that this is indeed the case.

In addition to space physics, magnetic reconnection plays an important role in laboratory plasmas. Toroidal magnetic confinement devices (“tokamaks”) were constructed for the purposes of controlling fusion, but the magnetic configurations expected from theoretical considerations to stably confine the fusing plasma would often suddenly go unstable, destroying confinement and damaging the device in a process known as a “disruption”. This, spurred on by Dungey’s successes in space physics, prompted Furth, Killeen, and Rosenbluth [Furth et al., 1963] to study the effects of collisionality on stability theory. They found that oppositely directed magnetic field lines in a collisional plasma are actually linearly unstable to small perturbations, which they called the “tearing mode instability”. (See Appendix A for a primer on the tearing mode.) The nonlinear development of the tearing mode provides the framework for magnetic reconnection without external driving.

With progress in fusion research, knowledge of how to avoid disruptions was gained. However, it was observed that when the temperature in a tokamak was increased to induce fusion, the core temperature would suddenly crash down to a lower value before rising again [von Goeler et al., 1974]. A trace of the core temperature as a function of time would have a shape of a sawtooth, as seen in Fig. 1.5. The so-called “sawtooth crash” was explained as a reconnection event by Kadomtsev [Kadomtsev, 1975]. The theory was initially quite successful, with the Kadomtsev model agreeing with observed time scales of sawtooth crashes. However, as larger fusion devices were constructed, the Kadomtsev model was found to be too slow

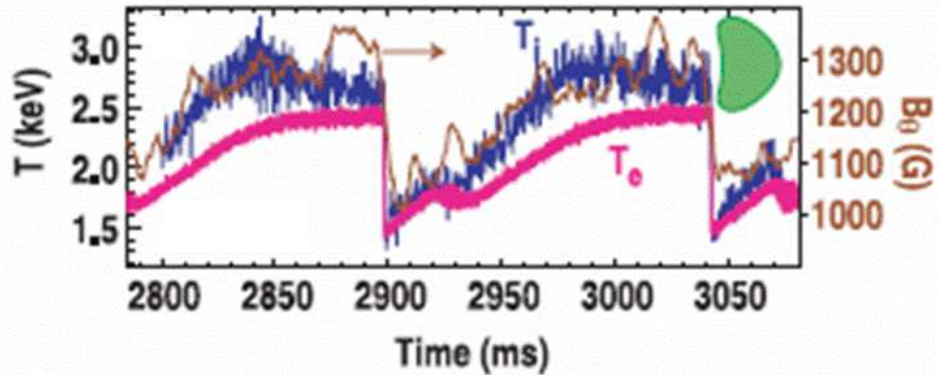


Figure 1.5: Core temperature of the DIII-D tokamak as a function of time during a sawtooth crash (in the bean configuration). Reprinted with permission from Ref. [Lazarus et al., 2006]. ©2006 Institute of Physics Publishing Ltd.

to explain the observed crash times [Edwards et al., 1986, Yamada et al., 1994]. A complete theory of the sawtooth crash remains elusive, though as in solar flares, collisionless effects are expected to be playing an important role (see, for example, [Biskamp, 2000]). Due to the importance of this problem and of magnetic reconnection in general, laboratory experiments solely devoted to the study of magnetic reconnection have become common.

Finally, reconnection is also being investigated in settings of astrophysical interest. Stellar (X-ray) flares exhibit similar light curves [Priest and Forbes, 2000] and power law statistics [Charbonneau et al., 2001] as solar flares, suggesting that the same mechanism causes solar and stellar flares. In addition, magnetic reconnection is a leading candidate for a mechanism for the dissipation of angular momentum in accretion disks surrounding massive compact objects (see [Quataert, 2006, Priest and Forbes, 2000] for reviews). A class of objects called “soft gamma re-

peaters” (SGRs) release $\sim 10^{45}$ erg in a time span of 200 s, and it is thought [Duncan and Thompson, 1992] that these could be reconnection events on magnetars, which are supernova remnant neutron stars threaded by super-strong magnetic fields of $B \sim 10^{15}$ G . Many other interesting astrophysical applications exist, from reconnection in the interstellar medium [Zweibel, 2006] to the dynamo [Biskamp, 2000] to stellar wind driven reconnection [ud Doula et al., 2006], and many others [Priest and Forbes, 2000].

In summary, magnetic reconnection is a ubiquitous physical process which converts magnetic energy into particle and flow energy of the surrounding plasma, creating outflow jets and energizing particles. It is capable of releasing large amounts of magnetic energy in a relatively short time. The Sweet-Parker model of collisional reconnection is too slow to explain observed energy release rates, but (collisionless) Hall reconnection is fast enough. Hall reconnection is the most promising model of fast reconnection. Signatures of Hall reconnection have been observed in the Earth’s magnetosphere [Øieroset et al., 2001, Mozer et al., 2002, Scudder et al., 2002] and laboratory experiments [Ren et al., 2005, Cothran et al., 2005].

1.2 Statement of the “Onset Problem”

Each of the examples of energy conversion due to magnetic reconnection described in the previous section, namely eruptions in the solar corona, substorms in the Earth’s magnetosphere, and the sawtooth crash in fusion devices, occur as rapid explosive events rather than by gradual or continuous energy release. Since

these events are all mediated by magnetic reconnection, it stands to reason that the explosive nature of these events is, in fact, caused by the underlying physics of magnetic reconnection. The primary objective of this thesis is to understand why fast magnetic reconnection does not always proceed at a fast rate and why it begins abruptly.

In the previous section, we made the case that collisionless effects, namely the Hall effect, explain the observed rate of magnetic energy release, but this does not address the question of why these events are explosive. Of course, to have an explosion, there must be a trigger which abruptly starts fast reconnection, as if on a switch. However, a trigger is not sufficient; there must also be a large reservoir of free (magnetic) energy which is released when the trigger is set off. This free energy, which is introduced by an external source, must be stored without significant release before onset.

This raises questions which pose a significant challenge to theoretical modeling. 1) What suppresses fast reconnection before onset? In other words, how is it possible that the system can be loaded with large amounts of magnetic energy over an extended period of time without significant release of the energy and without triggering the onset? (If the trigger is set off too easily, large amounts of free magnetic energy would not be able to accumulate and a large solar flare, for example, would never occur.) 2) What is the trigger mechanism which switches fast magnetic reconnection on, and what are the critical conditions under which such a transition occurs? These questions comprise the so-called “Onset Problem” of magnetic reconnection.

Some progress in understanding this process has been made. An important contribution was made by Bhattacharjee and coworkers [Bhattacharjee et al., 1999, Bhattacharjee, 2004], who showed that the time scale of the onset of Hall reconnection makes it a viable candidate to explain observed trigger times (*i.e.* the time between the trigger and when a peak is reached). But what turns the Hall effect on? It has long been known that collisionless effects are important when the thickness of the current sheet is smaller than the ion Larmor radius [Vasyliunas, 1975, Drake and Lee, 1977, Sonnerup, 1979, Terasawa, 1983, Hassam, 1984]. Hall reconnection simulations have been observed to undergo an extended growth phase where reconnection is slow and Sweet-Parker like (Y-type) when the current sheet is thick followed by a rapid onset of fast Petschek-like (X-type) reconnection when the sheet is thin [Aydemir, 1992, Horiuchi and Sato, 1994, Ma and Bhattacharjee, 1996, Shay et al., 2004]. However, a dynamical understanding of this process has been elusive, as most of the work on reconnection has concentrated on the steady-state. Understanding how Hall reconnection begins requires a dynamical theory of magnetic reconnection.

1.3 Summary of Results

In this thesis, we present a fully nonlinear model for the dynamics of magnetic reconnection and its potential solution to the Onset Problem in weakly collisional plasmas. After reviewing models of steady-state reconnection (in Chapter 2), we investigate the conditions under which these steady-state solutions exist. We show

that the Sweet-Parker solution exists only if the dissipation region is wider than a critical thickness at which the Hall effect becomes important. Meanwhile, the Hall solution exists only if the resistivity is not large enough to dominate the Hall effect in the dissipation region. Interestingly, since the resistive scales at which one or the other solution ceases to exist are vastly different, both the Sweet-Parker and Hall solutions can exist for the same set of parameters (*i.e.*, reconnection is bistable) for a wide range of values of a control parameter we call η' . Therefore, the steady-state solution the system evolves toward depends on the history of the system, *i.e.*, there is hysteresis. Past critical values of η' , only one of the two solutions exists. In Chapter 3, we present scaling arguments motivating bistability and hysteresis, and confirm the results with numerical simulations. We also discuss recent experimental results which agree with the simulations.

The finding that reconnection is bistable has two very important consequences. First, bistability has been well studied by the dynamics community, so information about the nonlinear dynamics of magnetic reconnection can be inferred. In particular, we interpret the catastrophic disappearance of a steady-state solution as η' is varied past a critical value as a saddle-node bifurcation. Then, we show that there are three signatures of the saddle-node bifurcation model which should be observable, including the existence of a heretofore unidentified unstable steady-state reconnection solution. In Chapter 4, we discuss the bifurcation model and confirm that the signatures of the bifurcation model are borne out by numerical simulations. In Chapter 5, we present a simple theoretical model which motivates the existence of saddle-node bifurcations, showing that it is the existence of dispersive waves

caused by the Hall effect which introduces saddle-node bifurcations into magnetic reconnection.

The second important consequence of the bistability of magnetic reconnection is that the result potentially has a profound impact on the Onset Problem. The bifurcation model offers a natural explanation of how the Hall effect can remain dormant while magnetic energy accumulates before turning on abruptly. Namely, magnetic energy can accumulate during Sweet-Parker reconnection because the energy release is so slow. Hall reconnection does not begin because of the history dependence of magnetic reconnection - if the Hall effect is unimportant initially, it will remain so. As reconnection progresses, the control parameter η' dynamically decreases. Once it crosses a critical value, the Sweet-Parker solution catastrophically disappears in a saddle-node bifurcation. A sudden transition to Hall reconnection ensues, which abruptly begins the fast release of the stored magnetic energy. In Chapter 6, we delineate possible scenarios under which the catastrophic onset of Hall reconnection in a weakly collisional plasma occurs, and discuss relevant observations in laboratory experiments and non-eruptive events in the solar corona. In addition, we apply the bifurcation model to solar flares and sawtooth crashes, showing in particular that predictions of time scales are consistent with observations of reconnection events in the solar corona. (We emphasize that the present onset mechanism is not expected to apply to a purely collisionless plasma, such as in the Earth's magnetosphere.)

1.4 Observations of Magnetic Reconnection Onset

Before reviewing magnetic reconnection theory, we discuss observations of onset of solar eruptions, magnetic substorms, and the sawtooth crash, as well as one example in a laboratory experiment. Relevant plasma parameters at onset are gathered, which we will use to make quantitative comparisons of our model to events in Nature. Table 1.1 shows directly measured plasma parameters in addition to observed time scales of the explosion process, namely the quiet time before onset during which magnetic energy accumulates, the onset time lasting from when the trigger is set off until peak values are seen, and the energy release time over which the accumulated energy is released. Table 1.2 has quantities derived from those in Table 1.1, including length scales that will be important in the remainder of this thesis (see the caption of Table 1.2 for definitions). We will see that the thickness of the Sweet-Parker dissipation region δ_{SP} is the length scale at which collisional effects become important, while the ion skin depth d_i and the ion Larmor radius based on the sound speed ρ_s are length scales at which the Hall effect becomes important.

1.4.1 Onset of Solar Eruptions

In this section, we discuss observations of the onset of solar eruptions. The generic term “solar eruptions” refers to solar flares and/or coronal mass ejections (CMEs). CMEs occur when a loop of magnetic field lines initially attached to the chromosphere (the solar surface) is ejected into interplanetary space, taking with it large amounts of solar material. Observations show that large solar flares (which

Table 1.1: Measured plasma parameters at reconnection onset for solar eruptions [Priest and Forbes, 2002], magnetic substorms [Kivelson and Russell, 1995, McPherron, 1999], the sawtooth crash at DIII-D [Lazarus et al., 2006], and in the VTF laboratory experiment [Egedal et al., 2006]. Values are the system size L_{sys} , the density n , the electron temperature T_e (note, 100 eV $\sim 10^6$ K), the strength of the reconnecting magnetic field B_{up} , the strength of the out of plane (guide) magnetic field B_{guide} , and the ion mass m_i . (Note, the effective degree of ionization at DIII-D is $Z_{eff} \simeq 2$.) Also listed are observed time scales of the quiet time before onset, the time of the onset itself, and the time it takes for the energy to be released.

	Solar Corona Active Region	Magnetosphere Magnetotail	Sawtooth Crash DIII-D	Experiment VTF
L_{sys} (cm)	10^9	10^9	40	20
n (cm^{-3})	3×10^9	0.1	4×10^{13}	2×10^{12}
T_e (eV)	100	150	2,500	60
B_{up}	<100 G	20 nT	<250 G	40 G
B_{guide}	100 G	5 nT	18,800 G	520 G
m_i (m_H)	1	1	2 (Deuterium)	40 (Argon)
τ_{quiet}	hours-days	1 hr	140 ms	80 μs
τ_{onset}	sec-min	2 min	$\ll 40 \mu\text{s}$	5 μs
$\tau_{release}$	2-20 min	30 min	< 40 μs	20 μs

release up to 10^{32} erg) are generally accompanied by CMEs of $\sim 10^{16}$ g of solar material. CMEs also occur without flares as so-called “prominence eruptions”, in which a prominence (a long lived loop of high density plasma extending from the solar surface into the corona) in the quiet sun is ejected, but observations suggest that the physical features of such eruptions are very similar to large solar flares. (See Ref. [Priest and Forbes, 2002] for a review.)

We confine this discussion to large so-called “two-ribbon” solar flares and their accompanying CMEs. Before the onset of a large solar flare, a prominence which straddles the line in an active region at which the magnetic field changes directions is formed over time spans of hours or even days [Aschwanden, 2005]. The pre-

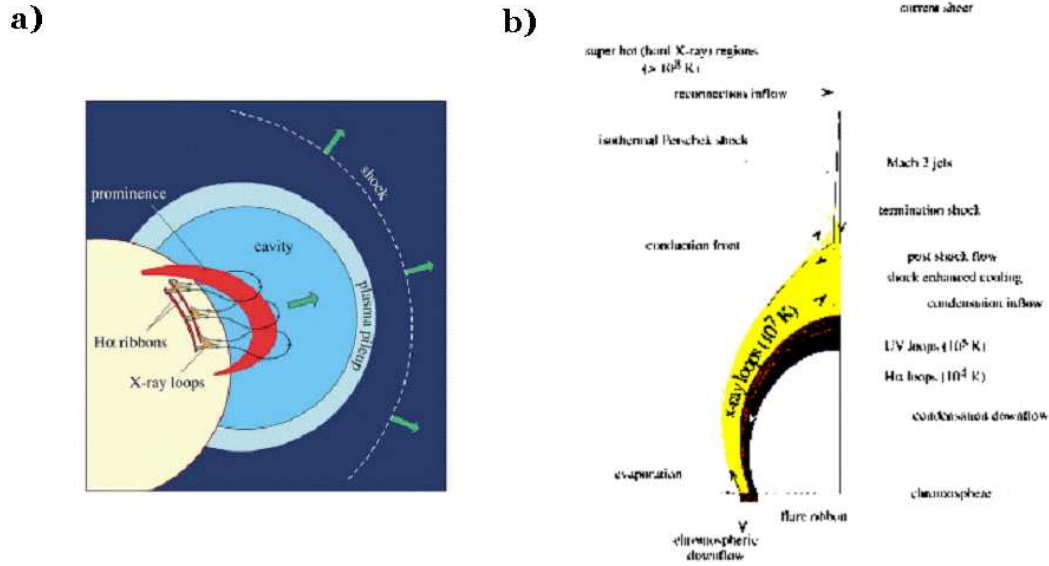


Figure 1.6: (a) Schematic representation of a two ribbon solar flare, showing a rising prominence and the generation of X-rays and two H α ribbons and (b) the radiation observed from the magnetic loops during a flare. Reprinted with permission from Terry Forbes as published in [Lin et al., 2003]. ©2002 Elsevier Science B. V.

flare configuration is pictured in Fig. 1.6a, where the prominence threads loops of magnetic field. How magnetic energy accumulates during the quiet time before a flare is still up for debate, though leading models [Parker, 1983, Mikic et al., 1988, Antiochos et al., 1999] suggest that it arises from shearing of magnetic fields due to motion of footpoints of flux tubes tied to the chromosphere.

When the eruption onsets, the prominence begins to rise and a burst of radiation from many different wavelength bands is observed from various places in the magnetic loops (see Fig. 1.6b). For example, hard X-rays are seen due to bremsstrahlung of energetic particles accelerated during the reconnection process. As shown in Fig. 1.7, the hard X-ray signal rises from pre-flare levels to peak level

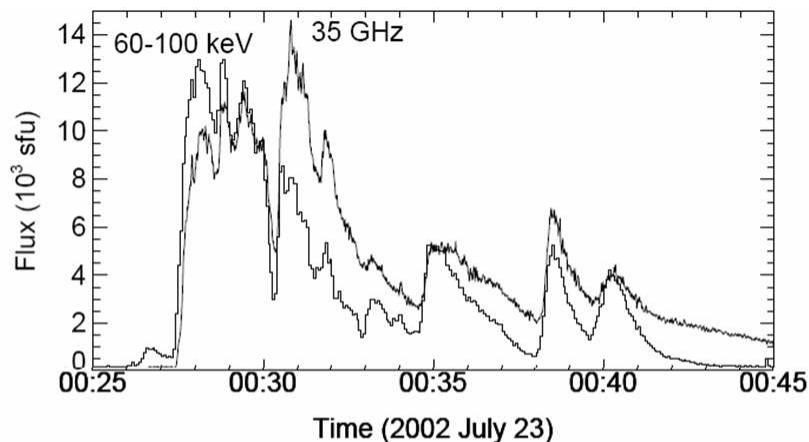


Figure 1.7: X-ray light curve during a solar flare. Reprinted with permission from Ref. [White et al., 2003]. ©2003 by The American Astronomical Society.

in the matter of minutes [Priest and Forbes, 2002], sometimes even in a matter of seconds [Miller et al., 1997]. As alluded to earlier, the hard X-ray signal dies out over a time span of about 2 to 20 minutes. (Soft X-ray and $H\alpha$ emission due to matter “evaporated” from the chromosphere into the corona can continue for hours or even days.) Relevant parameters from the pre-flare active regions of the solar corona are shown in Tables 1.1 and 1.2.

1.4.2 Onset of Magnetic Substorms

As discussed in Sec. 1.1, important changes to the Earth’s magnetosphere occur when the interplanetary magnetic field (IMF) turns southward. Reconnection between the IMF and the Earth’s dipole field is driven by the solar wind. The solar wind convects the reconnected field line over the poles of the Earth and stretches

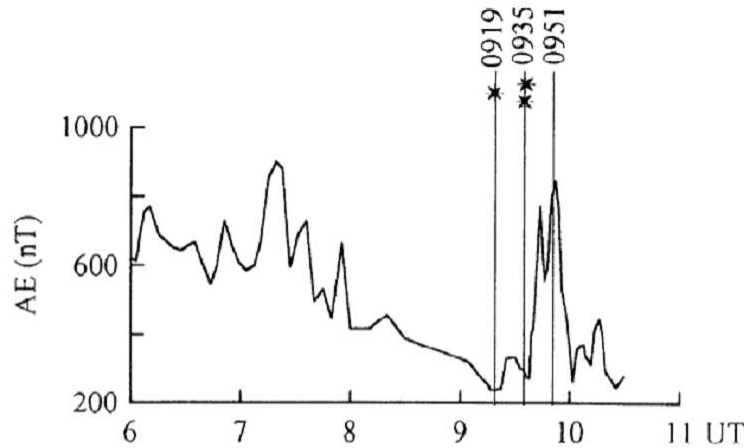


Figure 1.8: Auroral electrojet index during a magnetic substorm. Reprinted with permission from Ref. [Mishin et al., 1997]. ©1997 by the American Geophysical Union.

them out in the magnetotail. This process converts kinetic energy of the solar wind into stored magnetic energy in the magnetotail during what is called the “growth phase”, which lasts about an hour. As the energy accrues, the magnetotail thins [Mitchell et al., 1990, Asano et al., 2003]. Then, in the course of a couple of minutes, the substorm onsets, thought to be triggered by the onset of microinstabilities when the thickness of the plasma sheet becomes of the order of the ion skin depth d_i . The stored energy is released during the so-called “expansion phase”, lasting about 20 minutes. The outflow jets from reconnection shoot plasma toward the earth, generating current in the ionosphere above the auroral zones (called the “auroral electrojet”), which is measurable using magnetometers from Earth. The auroral electrojet (AE) index is, therefore, a measure of substorm activity. A trace of AE during a substorm is shown in Fig. 1.8. Relevant parameters in the pre-substorm magnetotail are in Tables 1.1 and 1.2. Note, in particular, that the density in

the magnetotail is very small, making the magnetotail essentially collisionless. We reiterate that the model for the catastrophic onset of fast reconnection presented in this thesis is not expected to apply to the onset of magnetic substorms.

1.4.3 The Sawtooth Crash

As discussed in Sec. 1.1 and shown in Fig. 1.5, the sawtooth crash is marked by a sudden decrease in the core temperature of a tokamak plasma. Unlike *in-situ* measurements in the magnetosphere and remote observations of the solar corona, diagnostics with high spatial and temporal resolution of sawtooth crashes are possible. In early tokamaks, such as the ST tokamak at Princeton, the sawtooth crash displayed a precursor oscillation during the rise phase [von Goeler et al., 1974]. This is consistent with a stable oscillating mode progressing through marginal stability, as in Kadomtsev’s model [Kadomtsev, 1975]. In later tokamaks such as the Joint European Torus (JET) [Edwards et al., 1986], the Tokamak Fusion Test Reactor (TFTR) [Yamada et al., 1994], and DIII-D [Lazarus et al., 2006], precursorless sawtooth crashes with a crash time of, for example, $\sim 40 \mu\text{s}$ at DIII-D [Lazarus et al., 2006], have been observed, which is faster than the Kadomtsev time of $\sim 1 \text{ ms}$. Relevant measured and derived parameters for the DIII-D tokamak are displayed in Tables 1.1 and 1.2.

Table 1.2: Plasma parameters derived from those in Table 1.1. The quantities are the ion cyclotron frequency $\Omega_{ci} = eB_{tot}/m_i c$ (where $B_{tot} = (B_{up}^2 + B_{guide}^2)^{1/2}$), the classical (Spitzer) resistivity [Krall and Trivelpiece, 1973] $\eta_{Sp} = (16\sqrt{\pi}Z_{eff}e^2 \ln \Lambda/3m_e)(m_e/2T)^{3/2}$ (where Z_{eff} is the effective ion charge, m_e is the electron mass, and $\ln \Lambda$ is the Coulomb logarithm [Krall and Trivelpiece, 1973]), the speed of sound $c_s = (Z_{eff}T_e/m_i)^{1/2}$, the Alfvén speed based on the reconnecting magnetic field $c_{Aup} = B_{up}/(4\pi m_i n)^{1/2}$, and the Alfvén speed based on the total magnetic field $c_A = B_{tot}/(4\pi m_i n)^{1/2}$. Also listed are relevant length scales, namely the theoretical thickness of the Sweet-Parker layer $\delta_{SP} = L_{sys}(\eta c^2/4\pi c_{Aup} L_{sys})^{1/2}$, the ion skin depth $d_i = (m_i c^2/4\pi n e^2)^{1/2} = c_A/\Omega_{ci}$, the ion Larmor radius based on the sound speed $\rho_s = c_s/\Omega_{ci}$, and the electron skin depth $d_e = (m_e c^2/4\pi n e^2)^{1/2}$.

	Solar Corona Active Region	Magnetosphere Magnetotail	Sawtooth Crash DIII-D	Experiment VTF
Ω_{ci} (s ⁻¹)	10 ⁶	1.9	9.1×10^7	1.25×10^5
η_{Sp} (s)	2×10^{-16}	2×10^{-16}	1.1×10^{-18}	4×10^{-16}
c_s (cm/s)	9×10^6	1.2×10^7	6.3×10^7	1.2×10^6
c_{Aup} (cm/s)	$< 4 \times 10^8$	1.4×10^8	$< 6.4 \times 10^6$	10 ⁶
c_A (cm/s)	4×10^8	1.4×10^8	4.8×10^8	1.2×10^7
δ_{SP} (cm)	> 200	320	> 0.02	0.75 ^a
d_i or ρ_s (cm)	$d_i \simeq 400$	$d_i \simeq 7.2 \times 10^7$	$\rho_s \simeq 0.69$	$\rho_s \simeq 10$
d_e (cm)	10	1.7×10^6	0.08	0.4

^a The measured resistivity η was $\sim 10\eta_{Sp}$, giving $\delta_{SP} \sim 2.4$ cm.

1.4.4 Spontaneous Onset in a Laboratory Plasma

Most laboratory experiments devoted to the study of magnetic reconnection initiate it with external driving in order to study it in a controlled manner. While properties of reconnection can be studied in this way, questions of onset are not addressed. Recent experiments at the Versatile Toroidal Facility (VTF) at Massachusetts Institute of Technology, however, have been able to address the question of onset [Egedal et al., 2006]. After a plasma is generated, external driving is used to create a tearing configuration. The reconnection is slow for 80 μ s before fast reconnection suddenly begins (over a time span of about 5 μ s), lasting for about

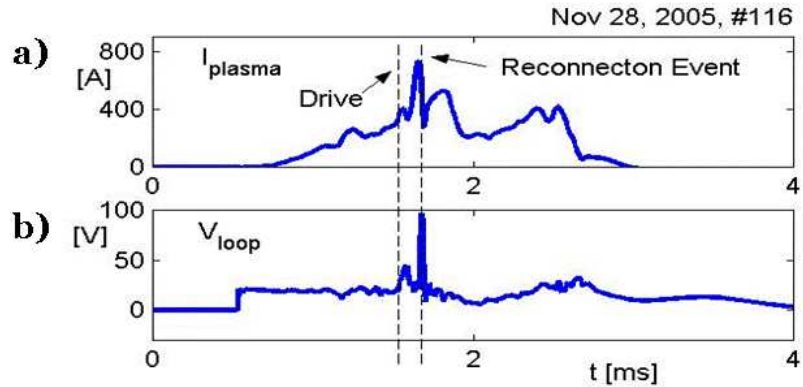


Figure 1.9: Current and voltage during a spontaneous reconnection event at VTF. The first vertical line is when the driving took place, the second where the onset occurred. Reprinted with permission from [Egedal et al., 2006].

$20 \mu\text{s}$. See Fig. 1.9. These bursts of fast reconnection occur in only about 10% of experimental trials, and thus are starting spontaneously after the driving has taken place and only if the conditions are right. This raises the exciting possibility that the conditions required for fast reconnection may soon be studied experimentally. Relevant parameters for the VTF experiment are listed in Table 1.1 and 1.2.

1.4.5 Summary

The four examples of reconnection events described in this section quantify the Onset Problem discussed in Sec. 1.2. Namely, in all four examples, a sudden onset of fast magnetic reconnection comes after a quiet time of energy accumulation lasting from 1 to 4 orders of magnitude longer than the onset time, showing that the dynamics happens on vastly different time scales. In what follows, we attempt to understand this intriguing behavior.

Chapter 2

Magnetic Reconnection in the Steady-State

Before discussing magnetic reconnection as a dynamical process, we review reconnection in the steady-state. Although reconnection in the solar corona, the magnetosphere, and laboratory plasmas is explosive (which prompted some to suggest that reconnection is inherently bursty), steady-state reconnection is not purely academic! Recent observations [Phan et al., 2006] showed that *undriven* magnetic reconnection in the solar wind is quasi-steady for a long time and over large scale spatial scales.

In Sec. 2.1, we describe the physics of reconnection in general. Then, we discuss collisional (Sweet-Parker) and collisionless (Hall) reconnection in the steady-state in Secs. 2.2 and 2.3. Finally, despite the fact that reconnection is manifestly nonlinear, we discuss the surprising importance of the underlying linear wave structure on reconnection in Sec. 2.4.

2.1 The Physics of Magnetic Reconnection

There are two parts to steady-state magnetic reconnection - the release of magnetic energy and the change in magnetic topology. We discuss how each of these takes place, and how the two processes feed off of each other to produce self-driven and self-sustaining magnetic reconnection.

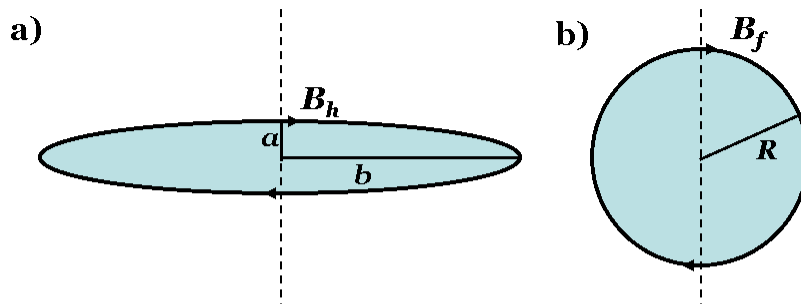


Figure 2.1: (a) A “squashed bubble” of magnetic flux. (b) The bubble after it has become round.

2.1.1 How Magnetic Energy Is Released

Magnetic energy is converted to flow and particle energy during magnetic reconnection. How does this happen? Consider a squashed bubble¹ of magnetic flux of width a and length b (with $a \ll b$) immersed in a stationary plasma, as pictured in Fig. 2.1a. When released, the elongated ends of the bubble will sling inwards to minimize the tension in the magnetic field, ending up as a circle of radius R , shown in Fig. 2.1b. If the plasma is incompressible, the area of the bubble will not change as it becomes round, so that $\pi ab \sim \pi R^2$. Also, the magnetic flux through a surface along the vertical axis (the dashed lines in Fig. 2.1) is conserved, so $B_h a \sim B_f R$, where B_h is the horizontal magnetic field of the squashed bubble and B_f is the magnetic field in the final state after the bubble has become round. The magnetic energy \mathcal{E}_f in the final state can be related to the initial magnetic energy in the

¹I thank Jim Drake for this example.

squashed bubble \mathcal{E}_i :

$$\mathcal{E}_f = \frac{B_f^2}{8\pi} \pi ab \sim \left(\frac{a^2}{R^2} \right) \frac{B_h^2}{8\pi} \pi R^2 \sim \left(\frac{a}{b} \right) \mathcal{E}_i. \quad (2.1)$$

Thus, for even a moderately squashed bubble, the final magnetic energy is much less than the initial magnetic energy; most of the magnetic energy is released.

Where does the energy go? To a first order approximation, the plasma moves with the magnetic field (see the discussion of the frozen-in law in the next section), so the magnetic energy is converted into kinetic energy of the initially stationary plasma. Equating the final kinetic energy density $m_i n v_f^2 / 2$ of the plasma, where m_i is the mass of the ions, n is the plasma density, and v_f is the final flow speed, to the initial magnetic energy density $B_h^2 / 8\pi$ gives

$$v_f \sim \frac{B_h}{\sqrt{4\pi m_i n}} = c_A, \quad (2.2)$$

i.e., the final flow speed is the Alfvén speed c_A based on the initial *horizontal* magnetic field strength. In summary, merely allowing a strongly bent magnetic field line to become round converts nearly all of the magnetic energy into plasma energy.

2.1.2 How Magnetic Topology Changes

When a bent field line becomes round, nearly all of the magnetic energy is released, but how do bent field lines come about? We now show that bent field lines are a natural consequence of the change in topology of the magnetic field during magnetic reconnection.

In the simplest description of a plasma, a change in the topology of the magnetic field cannot occur. In this simple model, ideal magnetohydrodynamics (MHD),

the plasma is assumed to be a perfect conductor. Loosely speaking, a change of topology of the magnetic field requires an electric field, known from Faraday’s Law. However, the electric field in a reference frame moving with a perfect conductor must vanish, precluding a change in the magnetic field.

More formally, the so-called “frozen-in law” asserts that the magnetic flux through any closed surface moving with the plasma cannot change². Choosing a surface that closely surrounds a particular magnetic field line shows that the field line cannot break. As a corollary, two fluid elements connected by a magnetic field line at a given time will be connected by a field line for all future times, *i.e.*, the plasma is constrained to move with the magnetic field.

However, a real plasma cannot be a *perfect* conductor. As such, the frozen-in law is not exact, and the topology of the magnetic field can change. Where does this occur? It typically occurs at the boundary layer between oppositely directed magnetic fields, where intense thin current sheets form. The canonical geometry for reconnection is depicted in Fig. 2.2, where the current flows in the z direction. From the right hand rule, there must be oppositely directed magnetic field lines in the $\pm x$ direction (shown in red and blue). To sustain the current, there must be an electric field E_z in the z direction. A generalization of this planar (anti-parallel magnetic

²The frozen-in law is the direct analog of the Kelvin vorticity theorem in fluid mechanics, proven by Helmholtz in 1858 and Kelvin in 1868. In general, for any field \mathbf{Q} satisfying $\partial\mathbf{Q}/\partial t = \nabla \times (\mathbf{v} \times \mathbf{Q})$, where \mathbf{v} is the bulk flow velocity, the flux of \mathbf{Q} through any surface S , $\int \mathbf{Q} \cdot d\mathbf{S}$, is convected unchanged with the flow, where $d\mathbf{S}$ is an element of surface area. See Refs. [Axford, 1984, Choudhuri, 1998, Shay, 1998] for a proof.

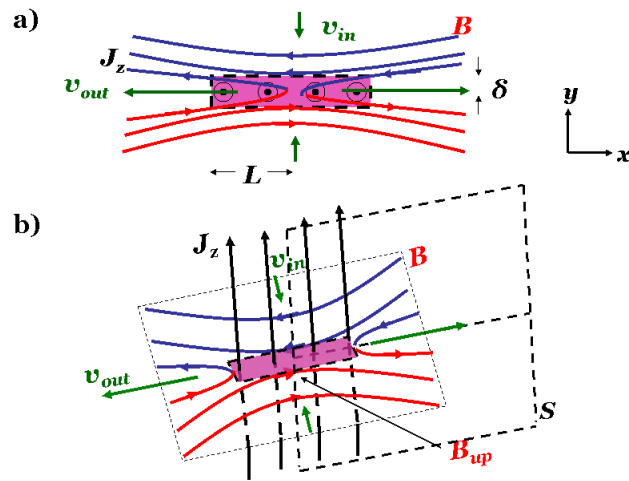


Figure 2.2: (a) Canonical geometry for anti-parallel reconnection. (b) View at an angle.

field) configuration is to add a uniform magnetic field in the z direction called a “guide field”, pictured in Fig. 2.3. In this configuration, only the component of the magnetic field in the $x - y$ plane reconnects. A projection onto the $x - y$ plane looks just like the anti-parallel case of Fig. 2.2a.

Far from the center of the current sheet, outside the so-called “dissipation region” shown as the shaded box in Figs. 2.2 and 2.3, ideal-MHD is an excellent approximation. Inside the dissipation region, the frozen-in law is invalid and the magnetic field lines break at a point called the “X-line”. To maintain Gauss’ Law which states that magnetic field lines cannot end, they cross connect to a field line pointing the opposite direction, sketched as the half red, half blue magnetic field lines in Fig. 2.2a. The newly reconnected field lines look just like half of a squashed bubble - the change in topology has generated strongly bent magnetic field lines.

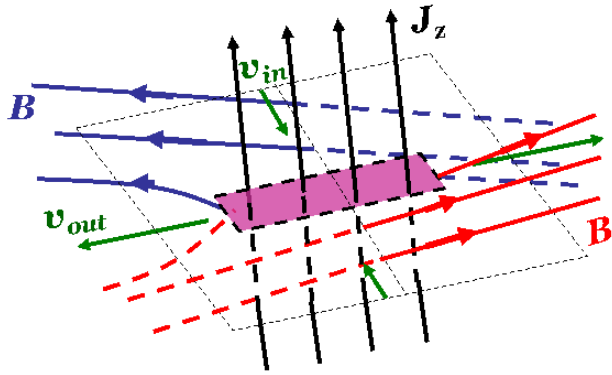


Figure 2.3: Geometry for reconnection with a guide field, shown at an angle. The projection into a plane is identical to that in Fig. 2.2a.

2.1.3 Putting It Together - How Reconnection Persists

We can now see how magnetic reconnection works. Magnetic energy is stored in stressed magnetic fields. Small scale dissipation allows for the field lines to break and cross-connect. In the new configuration, magnetic energy release through the straightening of bent field lines is energetically favorable, so the magnetic energy is released.

If only one field line reconnects, not much energy would be released and reconnection could not explain observed magnetic explosions. However, reconnection is a self-driven process. As the newly reconnected field lines straighten, they move in the $\pm x$ direction, accelerating plasma as they do. This leads to collimated out-flow jets with a speed of v_{out} , as shown in Fig. 2.2. Since plasma has been ejected from the center of the current sheet, there remains a lower pressure at the X-line. A pressure gradient force in the $\pm y$ direction drives flow into the dissipation region, labeled by v_{in} in Fig. 2.2. Since the plasma outside the dissipation region is

essentially frozen-in, the incoming plasma brings magnetic field lines into the dissipation region. These field lines reconnect, and the entire process continues until the available magnetic flux upstream of the dissipation region has been spent. Thus, magnetic reconnection is self-driven. When the rate at which magnetic flux enters the dissipation region is exactly balanced by the rate of diffusion of magnetic flux inside the layer, reconnection proceeds in a steady-state.

2.1.4 Analytical Treatment

We now quantify the steady-state reconnection process. We confine our treatment to the fluid model of magnetic reconnection³. The evolution equations of ideal-MHD are (see, for example Ref. [Chen, 1974]) Faraday's Law for the magnetic field \mathbf{B} , the continuity equation for the density n , and the momentum equation for the plasma bulk flow velocity \mathbf{v} :

$$\frac{\partial \mathbf{B}}{\partial t} = -c \nabla \times \mathbf{E}, \quad (2.3)$$

$$\frac{\partial n}{\partial t} + \nabla \cdot (n\mathbf{v}) = 0 \quad (2.4)$$

$$m_i n \left[\frac{\partial \mathbf{v}}{\partial t} + (\mathbf{v} \cdot \nabla) \mathbf{v} \right] = -\nabla p + \frac{1}{c} \mathbf{J} \times \mathbf{B}, \quad (2.5)$$

where \mathbf{E} is the electric field, c is the speed of light, and p is the plasma pressure. For simplicity, we take $p = nT$, where T is a constant and uniform temperature. The current density \mathbf{J} is defined using Ampère's Law, assuming that flows are non-relativistic so that the displacement current can be neglected,

$$\nabla \times \mathbf{B} = \frac{4\pi}{c} \mathbf{J}. \quad (2.6)$$

³For a kinetic approach, see Ref. [Drake and Shay, 2006].

Using Eq. 2.6, one can write $\mathbf{J} \times \mathbf{B} = (c/4\pi)[-\nabla(\mathbf{B} \cdot \mathbf{B}/2) + (\mathbf{B} \cdot \nabla)\mathbf{B}]$ in the momentum equation, Eq. 2.5, the two terms of which are interpreted as a magnetic pressure gradient force and a magnetic field line curvature force, respectively.

These equations are closed by assuming a form of the electric field. In ideal-MHD, the assumption of perfect conductivity means that the electric field in a reference frame moving with the plasma vanishes [Choudhuri, 1998], so

$$\mathbf{E} + \frac{\mathbf{v} \times \mathbf{B}}{c} = 0. \quad (2.7)$$

(This equation makes it apparent that ideal-MHD breaks down at current sheets, where \mathbf{B} goes through zero but the electric field does not.) Different equations for \mathbf{E} will be used in the sections to follow.

The most important descriptor of reconnection is the instantaneous rate of reconnection, *i.e.*, the amount of magnetic flux Φ being reconnected per unit time, which is a measure of how fast the reconnection process is going. The amount of reconnected magnetic flux through the semi-infinite $x-z$ plane S going through the X-line and infinite in extent in z (see the thick dashed line of Fig. 2.2b) is, using the integral form of Faraday's Law,

$$\frac{d\Phi}{dt} = -c \oint_C \mathbf{E} \cdot d\mathbf{l} \quad (2.8)$$

where $d\mathbf{l}$ is a line element along the boundary of S , in the z direction through the X-line and closing at infinity. Thus, the out of plane component of the electric field E_z (which drives the current J_z) is the rate that flux gets reconnected per unit length in the out of plane direction, referred to as the "reconnection rate" E .

We now develop scaling laws which hold in general for reconnection in the steady-state. Let δ and L be the half thickness and half length of the dissipation region, as depicted in Fig. 2.2a. Compressibility effects are usually negligible, so we take the density of the plasma to be a uniform n_0 . In the steady state, $\partial/\partial t = 0$, so Eq. 2.4 gives $\nabla \cdot \mathbf{v} = 0$, which scales like

$$\frac{v_x}{L} \sim \frac{v_y}{\delta} \Rightarrow v_{in} \sim \frac{\delta}{L} v_{out}, \quad (2.9)$$

where $v_y \sim v_{in}$ is the inflow speed and $v_x \sim v_{out}$ is the outflow speed. Similarly, from Gauss' Law, $\nabla \cdot \mathbf{B} = 0$,

$$\frac{B_x}{L} \sim \frac{B_y}{\delta} \Rightarrow B_{down} \sim \frac{\delta}{L} B_{up}, \quad (2.10)$$

where $B_x \sim B_{up}$ is the horizontal component of the magnetic field immediately upstream of the dissipation region and $B_y \sim B_{down}$ is the vertical component of the magnetic field at the outflow edge of the dissipation region. The outflow is generated by the magnetic curvature, so balancing the convection term $(\mathbf{v} \cdot \nabla)\mathbf{v}$ with the magnetic curvature term $(\mathbf{B} \cdot \nabla)\mathbf{B}$ in the outflow (x) component of the momentum equation, Eq. 2.5, gives $m_i n_0 v_x (v_x/L) \sim (1/4\pi) B_y (B_x/\delta)$. Using Eq. 2.10, this gives

$$v_{out} \sim c_{Aup}, \quad (2.11)$$

where $c_{Aup} = B_{up}/(4\pi m_i n_0)^{1/2}$. Thus, the outflow speed scales like the Alfvén speed based on the horizontal (x) component of the magnetic field strength immediately upstream of the dissipation region, which meets the expectations of Eq. 2.2.

It remains to determine v_{in} , or equivalently from Eq. 2.9, δ and L . Note that in the steady-state, Faraday's Law (Eq. 2.3) requires that the electric field is

uniform. In particular, the reconnection electric field $E_z = E$ is independent of space. Directly upstream of the dissipation region, ideal-MHD is valid, so from the ideal-MHD Ohm's Law (Eq. 2.7),

$$E \sim \frac{v_{in} B_{up}}{c}, \quad (2.12)$$

which shows that v_{in} is also a measure of the reconnection rate. This makes sense physically because it is the inflow that convects magnetic field lines into the dissipation region. The reconnection rate E is usually presented as a normalized quantity E' . It is normalized to the upstream magnetic field strength B_{up} and to the outflow speed $v_{out} \sim c_{Aup}$, *i.e.*,

$$E' = \frac{cE}{c_{Aup} B_{up}}. \quad (2.13)$$

Using Eqs. 2.9 and 2.12, the following quantities are all equivalent measures of the normalized reconnection rate in the steady-state:

$$E' \sim \frac{v_{in}}{v_{out}} \sim \frac{\delta}{L}. \quad (2.14)$$

Eqs. 2.9 - 2.12 are general results describing steady-state reconnection. The inflow speed v_{in} , and thus the reconnection rate E , depends heavily on what causes the ideal-MHD Ohm's Law to break down. We discuss two important classes of effects in the following two sections.

2.2 Collisional (Sweet-Parker) Reconnection

The simplest effect that invalidates the assumptions of ideal-MHD is that real plasmas are not perfect conductors. Just like when passing a current through a

wire, finite conductivity can be caused by resistivity η (due to collisions between electrons and ions) and a non-zero electron mass m_e (which makes the reaction time of the electrons to short any electric field not infinitely fast). In the Sweet-Parker model [Sweet, 1958, Parker, 1957], electron-ion collisions break the frozen-in law. The electric field is given by the microscopic form of Ohm's Law, which in the laboratory frame is (see, for example, [Griffiths, 1998])

$$\mathbf{E} + \frac{\mathbf{v} \times \mathbf{B}}{c} = \eta \mathbf{J}. \quad (2.15)$$

When Eq. 2.15 is used in place of Eq. 2.7 with the other equations of ideal-MHD (Eqs. 2.3 - 2.6) unchanged, the theory is referred to as resistive-MHD. Substituting Eq. 2.15 into Eq. 2.3 gives

$$\frac{\partial \mathbf{B}}{\partial t} = \nabla \times (\mathbf{v} \times \mathbf{B}) + \frac{\eta c^2}{4\pi} \nabla^2 \mathbf{B}. \quad (2.16)$$

In order to find the inflow speed v_{in} for Sweet-Parker reconnection, consider the evolution of the reconnecting magnetic field, described by the x component of this equation. In an incompressible plasma,

$$\frac{\partial B_x}{\partial t} = (\mathbf{B} \cdot \nabla) v_x - (\mathbf{v} \cdot \nabla) B_x + \frac{\eta c^2}{4\pi} \nabla^2 B_x. \quad (2.17)$$

Immediately upstream of the dissipation region, the flow is nearly vertical, so v_x is negligible, leaving

$$v_y \frac{\partial B_x}{\partial y} = \frac{\eta c^2}{4\pi} \nabla^2 B_x \quad (2.18)$$

in the steady-state. This equation says that when the rate of convection of magnetic field lines into the dissipation region is equal to the rate of diffusion of magnetic field

lines within the dissipation region, a steady-state is reached. A scaling analysis gives

$$\frac{v_{in}}{\delta} \sim \frac{\eta c^2}{4\pi\delta^2}. \quad (2.19)$$

Using Eqs. 2.9 and 2.11 to eliminate v_{in} and δ in turn gives the Sweet-Parker reconnection rate E'_{SP} as

$$E'_{SP} \sim \frac{v_{in}}{v_{out}} \sim \frac{\delta}{L} \sim \sqrt{\frac{\eta c^2}{4\pi c_{Aup} L}}. \quad (2.20)$$

The only unknown that remains is the dissipation region length L . Results of numerical simulations [Biskamp, 1986, Scholer, 1989, Uzdensky and Kulsrud, 2000, Jemella et al., 2003, Jemella et al., 2004] have shown that the length of the Sweet-Parker current sheet scales with the system size L_{sys} . Thus, for two colliding flux tubes, the length scale is on the order of the radius of the flux tube. This completely specifies the famous Sweet-Parker model.

Parker immediately recognized [Parker, 1957, Parker, 1963] its downfall as a potential explanation of magnetic explosions such as solar flares, which release their energy in a few minutes. Using the values of parameters in solar active regions presented in Sec. 1.4, we find $E' \sim 2 \times 10^{-7}$, corresponding to an inflow speed of only $v_{in} \sim 80$ cm/s. To reconnect a flux tube of radius $L_{sys} \sim 10^9$ cm, it would take $\tau \sim L_{sys}/v_{in} \sim 10^7$ s, which is about four orders of magnitude too long.

There are two reasons that Sweet-Parker reconnection is too slow. First, the Sweet-Parker reconnection rate E'_{SP} scales like $\eta^{1/2}$ and the (classical) resistivity of plasmas of interest are very small. Second, E'_{SP} scales like $L_{sys}^{-1/2}$, and global length scales are very large. Physically, since the outflow nozzle has a thickness of $\delta_{SP} \sim E'_{SP} L_{sys}$, the dissipation region is very thin compared to its length (see

Fig. 1.3a). Since the outflow speed is fixed at the Alfvén speed and the inflow is entering the dissipation region along its entire length, it must be coming in very slowly to obey continuity.

While the Sweet-Parker model does not account for the rate of energy release during a solar flare, laboratory experiments both without [Trintchouk et al., 2003] and with [Furno et al., 2005] a guide field have shown that the Sweet-Parker scaling result (based on a classical resistivity) successfully accounts for observations in collisional plasmas. Therefore, the Sweet-Parker model is a physically viable model, but additional physics is required to explain the magnetic energy conversion as fast as observed in, for example, solar flares.

2.3 Collisionless (Hall) Reconnection

Even in the absence of collisions, ideal-MHD breaks down due to finite Larmor radius effects. In ideal-MHD, particles gyrate around the same magnetic field line for all time due to the frozen-in law. However, if a particle sees vastly different magnetic field strengths during one gyro-orbit, ideal-MHD is not valid. In particular, if a particle sees a magnetic field pointing in the opposite direction during a gyro-orbit, it will start to gyrate in the opposite direction, thereby dissociating from its original magnetic field line. (See Fig. 1.15 of Ref. [Shay, 1998].) This motion is called “meandering”. Interestingly, ion meandering alone does not allow for a change in topology of the magnetic field but has a profound effect on the rate at which reconnection proceeds.

Non-ideal-MHD effects can be captured at once using the electron equation of motion,

$$m_e \frac{d\mathbf{v}_e}{dt} = -\frac{1}{n} \nabla \cdot \mathbf{P}_e - e \left(\mathbf{E} + \frac{\mathbf{v}_e \times \mathbf{B}}{c} \right) + m_e \nu_{ei} (\mathbf{v}_e - \mathbf{v}_i), \quad (2.21)$$

where m_e is the electron mass, $\mathbf{v}_e(\mathbf{v}_i)$ is the electron (ion) bulk flow velocity, \mathbf{P}_e is the electron pressure tensor, e is the magnitude of the electron charge, and ν_{ei} is the electron-ion collision frequency. The explicit appearance of the electron velocity can be eliminated using the definition of \mathbf{J} ,

$$\mathbf{v}_e = \mathbf{v}_i - \frac{\mathbf{J}}{ne}. \quad (2.22)$$

We will show later that the left hand side of Eq. 2.21 is only important at small length scales where the ion bulk flow can be approximated as $\mathbf{v}_i \simeq 0$, so it is a good approximation to neglect the ion motion in this term, giving

$$\frac{d\mathbf{v}_e}{dt} = \left[\frac{\partial}{\partial t} + \mathbf{v}_e \cdot \nabla \right] \mathbf{v}_e \simeq \left[\frac{\partial}{\partial t} - \frac{\mathbf{J}}{ne} \cdot \nabla \right] \left(-\frac{\mathbf{J}}{ne} \right). \quad (2.23)$$

Solving Eq. 2.21 for the electric field gives

$$\mathbf{E} + \frac{\mathbf{v}_i \times \mathbf{B}}{c} = \eta \mathbf{J} + \frac{1}{nec} \mathbf{J} \times \mathbf{B} - \frac{1}{ne} \nabla \cdot \mathbf{P}_e + \frac{m_e}{e^2} \frac{d\mathbf{J}/n}{dt}, \quad (2.24)$$

where $\eta = \nu_{ei} m_e / ne^2$ is the resistivity and it is to be understood that $d/dt \simeq \partial/\partial t - (\mathbf{J}/ne) \cdot \nabla$. The four terms on the right hand side are called the resistive term, the Hall term, the electron pressure gradient term, and the electron inertia term, respectively. When written in this form, it is called the ‘‘generalized Ohm’s Law’’ [Rossi and Olbert, 1970] because when the three right-most terms are neglected, it reduces to the Ohm’s Law in Eq. 2.15. When Eq. 2.24 is used in place of Eq. 2.7

with the other equations of ideal-MHD (Eqs. 2.3 - 2.6), the set of equations is called “Hall-MHD”⁴.

The resistive term, the electron inertia term, and the off diagonal elements of the electron pressure gradient term describe dissipative mechanisms which break the frozen-in law. The Hall term and the diagonal elements of the electron pressure gradient term describe finite Larmor radius effects. To see this, consider the Hall and scalar part p_e of the electron pressure gradient terms alone, giving

$$\mathbf{E} + \frac{\mathbf{v}_e \times \mathbf{B}}{c} = -\frac{1}{ne} \nabla p_e. \quad (2.25)$$

Inserting this into Faraday’s Law (Eq. 2.3) and assuming $p_e = nT_e$ for a constant and uniform electron temperature T_e gives $\partial \mathbf{B} / \partial t = \nabla \times (\mathbf{v}_e \times \mathbf{B})$. For the same reason Eq. 2.7 in ideal-MHD implies the magnetic field is frozen-in to the plasma moving with velocity \mathbf{v} , this equation implies the magnetic field is frozen-in to the *electron* fluid moving with velocity \mathbf{v}_e . Thus, by themselves, the Hall effect and scalar part of the electron pressure gradient do not allow reconnection⁵. While the electrons are frozen-in to the magnetic field, the ions are not. The ions are said to be “demagnetized” and to have “decoupled” from the electrons and the magnetic field.

⁴Technically, Hall-MHD was defined [Huba, 1995] having the electron mass $m_e = 0$, while “two-fluid theory” refers to the same equations with a non-zero electron mass. In keeping with current conventions, we use the two terms interchangeably.

⁵That the electron pressure gradient term does not break the frozen-in law even when T_e is not constant and uniform is less obvious [Cowley, 2006]. Under the safe assumption that $(\mathbf{B} \cdot \nabla) T_e = 0$, one can show that $\mathbf{E} + \tilde{\mathbf{v}} \times \mathbf{B} / c = -(1/e) \nabla [T_e (1 + \ln n)]$ where $\tilde{\mathbf{v}} = \mathbf{v}_e - (c/eB^2) \ln n (\mathbf{B} \times \nabla T_e)$. Thus, $\partial \mathbf{B} / \partial t = \nabla \times (\tilde{\mathbf{v}} \times \mathbf{B})$, which is of the form required for the frozen-in condition to hold.

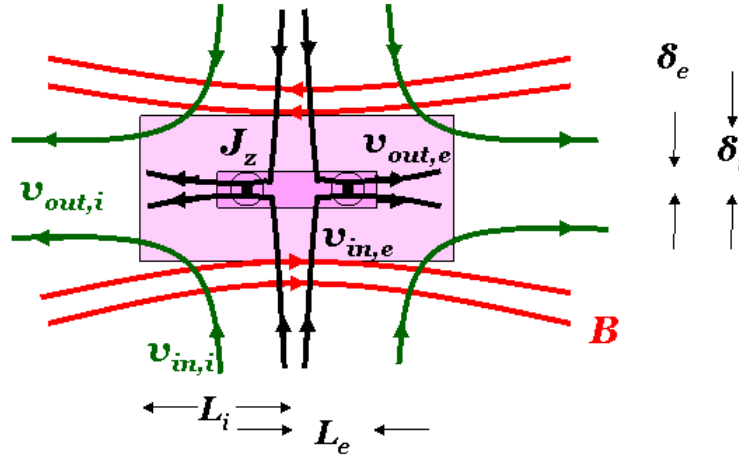


Figure 2.4: Two scale structure during Hall reconnection. Adapted from Ref. [Drake and Shay, 2006].

Why do the ions decouple from the field but not the electrons? When electrons and ions move together, both gyrate about magnetic field lines whether due to thermal or inertial effects. Since the ions are heavier, their radius of gyration is larger. When a magnetic field line in the upstream region gets within one ion gyro-radius of the X-line, the ions see a magnetic field pointing in the opposite direction and demagnetize. Since the electron gyro-orbits are smaller, the electrons remain frozen-in. Only when the fields are within one electron gyro-radius of the X-line do the electrons demagnetize due to electron inertia, which breaks the electron frozen-in law and allows reconnection to proceed. Thus, Hall reconnection takes on a qualitatively different character than Sweet-Parker reconnection. There is a two-scale structure, as depicted in Fig. 2.4, with an ion dissipation region of thickness δ_i and length L_i surrounding an electron dissipation region of thickness δ_e and length L_e .

The decoupling of ions from the magnetic field due to the Hall effect has profound implications. The Hall effect is important in the region outside the electron dissipation region but inside the ion dissipation region. Therefore, the Hall effect controls the straightening of the magnetic field lines which generates the outflow from the dissipation region. The outflow is generated differently than in MHD because the wave structure is altered by the presence of the Hall term. Interestingly, the nature of Hall-MHD waves makes Hall reconnection open out into the Petschek configuration pictured in Fig. 1.3b, meaning that Hall reconnection is fast. We discuss the wave structure of Hall-MHD and why Hall-MHD waves lead to the Petschek configuration while MHD waves do not in Sec. 2.4.

Hall reconnection has an important observational signature. Between distances of the ion and electron gyro-radii from the X-line, the electrons are frozen-in but the ions are not. The meandering motion of the ions means that their bulk flow speed is small, $\mathbf{v}_i \simeq 0$, while the bulk flow of the electrons is significant. From Eq. 2.22, an in-plane ($x - y$) current density points away from the X-line in the upstream direction (and toward the X-line in the downstream direction), as depicted by the dashed lines in Fig. 2.5. From the right-hand rule, this current produces an out of plane magnetic field with the quadrupole structure shown. This quadrupolar out of plane magnetic field was noted in Refs. [Sonnerup, 1979, Terasawa, 1983, Hassam, 1984] and related to the physics of the whistler wave (see Sec. 2.4.2) in Ref. [Mandt et al., 1994]. It has now been observed during reconnection in the magnetosphere [Øieroset et al., 2001, Mozer et al., 2002, Scudder et al., 2002, Runov et al., 2003] and in laboratory experiments [Ren et al., 2005, Cothran et al., 2005].

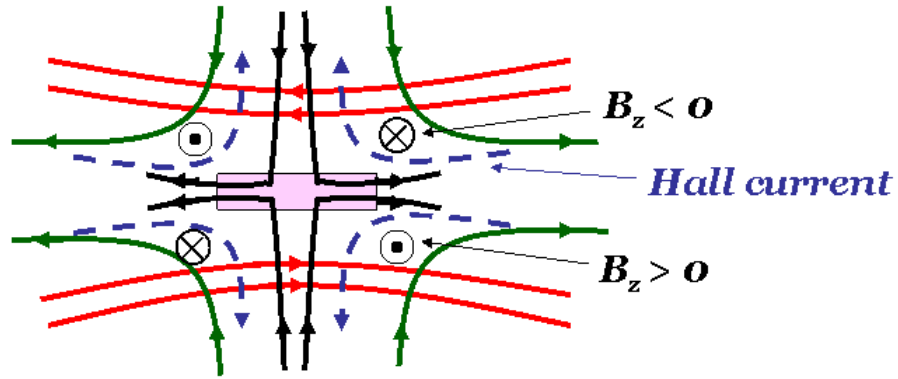


Figure 2.5: Quadrupolar out of plane magnetic field during Hall reconnection. Adapted from Ref. [Sonnerup, 1979].

Just how fast is Hall reconnection in the steady-state? Unfortunately, no first principles theory (or even scaling argument!) can successfully answer this question. However, much has been learned using large scale numerical simulations. We now summarize results of theory and simulations of Hall reconnection, concentrating on the steady-state reconnection rate E and important length and velocity scales specifying the geometry. Because there are important differences, we treat anti-parallel and component reconnection separately.

2.3.1 Anti-parallel Hall Reconnection

First and foremost, Hall reconnection is not subject to the two downfalls of the Sweet-Parker model, namely strong dependence of the reconnection rate E' on the dissipation mechanism and global length scales. In the GEM Challenge study (Ref. [Birn et al., 2001] and references therein), it was found that the Hall reconnection rate E'_H is insensitive to the dissipation mechanism. Identical simula-

tions were performed using particle, hybrid, Hall-MHD, and resistive-MHD codes. With the exception of the resistive-MHD simulations for which reconnection was very slow, the reconnection rate was fast, with similar rates whether electron inertia, numerical (fourth order) dissipation, or off diagonal elements of the pressure tensors broke the electron frozen-in law. This showed that the essential requirement for fast reconnection is the presence of the Hall effect, since the only difference between the resistive-MHD and Hall-MHD simulations is the inclusion of the Hall effect in the latter. In addition, it has been shown [Shay and Drake, 1998, Hesse et al., 1999, Pritchett, 2001, Ricci et al., 2002] that E'_H is independent of the magnitude of the electron mass, which sets the radius of the electron gyro-orbit. We motivate why E'_H is independent of the dissipation mechanism in Sec. 2.4.4. As for dependence on the system size, it has been shown using numerical simulations [Shay et al., 1999, Huba and Rudakov, 2004] that the Hall reconnection rate is independent of the system size.

The lack of dependence of the steady-state Hall reconnection rate on any of the system parameters led Shay et al. [Shay et al., 1999] to assert that E'_H is a constant⁶ of order 0.1 [Shay et al., 1999, Huba and Rudakov, 2004]. Using the parameters for an active region of the solar corona given in Sec. 1.4, the inflow

⁶The independence of E'_H on seemingly any system parameters is a matter of contentious debate. Many authors [Grasso et al., 1999, Wang et al., 2001, Porcelli et al., 2002, Fitzpatrick, 2004, Bhattacharjee et al., 2005] have claimed to see a dependence on the reconnection rate, though it has been suggested [Shay et al., 2004] that these results were not in the long time asymptotic steady-state or were not being properly normalized following Eq. 2.13. The debate continues.

speed is $v_{in} \sim E' c_{Aup} \sim 4 \times 10^7$ cm/s, so the time it would take to reconnect a flux tube of radius $L_{sys} \sim 10^9$ cm is $\tau \sim L_{sys}/v_{in} \sim 25$ s. This is certainly fast enough to explain observed times of a few minutes.

The thickness of the ion dissipation region can be estimated by finding the distance from the X-line where the ions decouple from the electrons, *i.e.*, where the Hall effect becomes important. Substituting the generalized Ohm's Law (Eq. 2.24) into Faraday's Law (Eq. 2.3) and assuming a scalar electron pressure p_e gives

$$\frac{\partial \mathbf{B}}{\partial t} = \nabla \times \left[\mathbf{v}_i \times \mathbf{B} - \frac{\mathbf{J} \times \mathbf{B}}{ne} - \frac{m_e c}{e^2} \frac{d\mathbf{J}/n}{dt} \right]. \quad (2.26)$$

The Hall term becomes important when the convection of field lines (B_x) into the dissipation region is balanced by the Hall effect,

$$(\mathbf{v}_i \cdot \nabla) B_x \sim \frac{1}{ne} (\mathbf{J} \cdot \nabla) B_x. \quad (2.27)$$

We perform a scaling analysis, first applied to reconnection in Ref. [Vasyliunas, 1975]. Since the flow is nearly vertical in the upstream region, $\mathbf{v}_i \cdot \nabla \sim v_{in}/\delta$ and $\mathbf{J} \cdot \nabla \sim J_y/\delta$. From Ampère's Law (Eq. 2.6), $J_y \sim cB_z/4\pi L$, so using Eqs. 2.9 and 2.11 gives

$$\frac{\delta}{L} c_{Aup} \sim \frac{cB_z}{4\pi n_0 e L}. \quad (2.28)$$

In the next section, we will show that $B_z \sim B_{up}$, so the length scale δ at which the Hall effect becomes important is

$$\delta \sim d_i, \quad (2.29)$$

where $d_i = c_A/\Omega_{ci} = c/\omega_{pi} = (m_i c^2/4\pi n_0 e^2)^{1/2}$ is the ion Larmor radius based on the Alfvén speed, called the ion skin depth or ion inertial length. Here, $\Omega_{ci} = eB/m_i c$ is

the ion cyclotron frequency and $\omega_{pi} = (4\pi n_0 e^2 / m_i)^{1/2}$ is the ion plasma frequency. This length scale is extremely small compared to the global length scale L_{sys} in systems of interest, as can be seen in Table 1.2 in Sec. 1.4. Numerical simulations [Shay et al., 1998] and laboratory experiments [Yamada et al., 2006] have confirmed that the thickness of the ion dissipation region is of order d_i .

Similarly, we can find the thickness of the electron dissipation region when electron inertia breaks the electron frozen-in law. This occurs when the z component of the electric field due to the electron inertia term in Eq. 2.24 becomes of the same order as the Hall electric field,

$$\frac{J_y B_x}{nec} \sim \frac{m_e}{e^2} \left(\frac{\mathbf{J}}{ne} \cdot \nabla \right) \frac{J_z}{n}. \quad (2.30)$$

A scaling analysis with $B_x \sim B_{up}$, $J_z \sim cB_{up}/4\pi\delta$ and $\mathbf{J} \cdot \nabla \sim J_y/\delta$ gives

$$\delta \sim d_e, \quad (2.31)$$

where $d_e = c/\omega_{pe} = (m_e c^2 / 4\pi n_0 e^2)^{1/2}$ is called the electron skin depth or electron inertial length⁷. Numerical simulations have confirmed [Shay et al., 1998] that the thickness of the electron dissipation region scales like d_e for anti-parallel Hall reconnection.

Other parameters describing Hall reconnection can readily be found. Since the outflow from the ion dissipation region is at the ion Alfvén speed c_{Aup} (from Eq. 2.11), the inflow speed is

$$v_{in} \sim E'_H v_{out} \sim 0.1 c_{Aup}. \quad (2.32)$$

⁷That the electron inertia term is only appreciable at length scales of d_e and below justifies the approximation used in Eq. 2.23.

By continuity (see Eq. 2.14), the length of the ion dissipation region is $L_i \sim \delta/E'_H \sim 10d_i$. For the electron layer, numerical simulations have shown [Shay et al., 2001, Hoshino et al., 2001] that the outflow speed is the *electron* Alfvén speed $c_{Aup,e} = B_{up,e}/(4\pi m_e n_0)^{1/2}$ based on the magnetic field strength upstream of the *electron* dissipation region. Until recently, it was thought that the electron inflow speed was $v_{in,e} \sim 0.1c_{Ae}$ [Shay et al., 1999, Huba and Rudakov, 2004] corresponding to $L_e \sim 10d_e$, but new results [Daughton et al., 2006, Shay et al., 2006] suggest that the electron dissipation region extends all the way to the edge of the *ion* dissipation region, $L_e \sim 10d_i$. Observations [Runov et al., 2003] in the magnetotail with the Cluster spacecraft may support this result.

2.3.2 Component Hall Reconnection

Less is known about component Hall reconnection than anti-parallel because the simulations are computationally more expensive. Simulation results suggest that guide field Hall reconnection is still fast [Kleva et al., 1995, Hesse et al., 1999, Pritchett, 2001, Rogers et al., 2001, Hesse et al., 2002, Huba, 2005] (subject to a few constraints we discuss in Sec. 2.4.3) and independent or only weakly dependent on the dissipation mechanism [Pritchett, 2001, Ricci et al., 2004]. A careful study of the dependence of the reconnection rate on the system size has yet to be undertaken.

There is an important piece of additional physics for Hall reconnection with a strong guide field $B_{z0} \gg B_{up}$ that is not present in anti-parallel Hall reconnection.

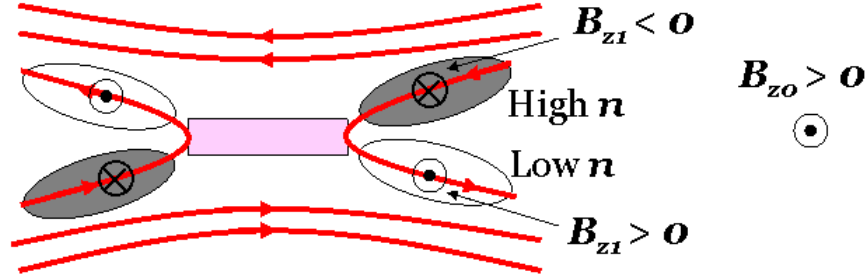


Figure 2.6: Quadrupolar density configuration during component Hall reconnection. Adapted from Ref. [Drake and Shay, 2006].

Just as in the anti-parallel case, the decoupling of ions from electrons due to the Hall effect leads to a quadrupolar structure in the out of plane magnetic field, as shown in Fig. 2.5. However, because of the strong guide field, even a small out of plane magnetic disturbance B_{z1} creates a sizable difference in magnetic pressure⁸. To maintain a steady-state, this change in magnetic pressure must be balanced by a change in the plasma density n_1 , given by

$$n_1 T = -\frac{1}{4\pi} B_{z0} B_{z1}. \quad (2.33)$$

Thus, where the component of the quadrupole out of plane magnetic field enhances the guide field, the density must become smaller, while the density must become larger where the quadrupole field diminishes the guide field (see Fig. 2.6).

A quadrupolar structure in the density, including two density cavities, is formed, which is an important observational signature of Hall reconnection with a strong

⁸The change in magnetic pressure δP_m due to a perturbation \mathbf{B}_1 on a field of \mathbf{B}_0 is $\delta P_m = (1/8\pi)(\mathbf{B}_0 + \mathbf{B}_1)^2 - (1/8\pi)\mathbf{B}_0^2 \simeq (1/4\pi)\mathbf{B}_0 \cdot \mathbf{B}_1$, which is appreciable for large \mathbf{B}_0 .

guide field [Kleva et al., 1995, Drake, 1995, Tanaka, 1996]. Most of the current is contained in the high density areas, so the current sheet takes on a twisted appearance, another signature of component Hall reconnection.

At what length scale does the Hall effect become important? Surprisingly, the answer is different than in anti-parallel reconnection, where it was d_i . We present a scaling argument here, though the physics will be clearer when we treat linear waves in Sec. 2.4.3. Beginning from Eq. 2.26, we find the length scale at which the Hall effect is the same order as the MHD term. In the x direction, as in the anti-parallel case, we have

$$(\mathbf{v}_i \cdot \nabla)B_x \sim \frac{1}{ne}(\mathbf{J} \cdot \nabla)B_x, \quad (2.34)$$

which using $J_y \sim cB_{z1}/4\pi L$ and $v_y \sim v_x\delta/L$ gives $v_x \sim cB_{z1}/4\pi ne\delta$. However, in the z component of Faraday's Law, the compression term $B_{z0}(\nabla \cdot \mathbf{v}_i)$ is more important than the convection term $(\mathbf{v}_i \cdot \nabla)B_{z1}$, so

$$B_{z0}(\nabla \cdot \mathbf{v}_i) \sim (\mathbf{B} \cdot \nabla)\frac{J_z}{ne}. \quad (2.35)$$

Using the continuity equation, $\nabla \cdot \mathbf{v}_i = -(1/n)dn/dt$, the previous equation becomes

$$\frac{B_{z0}}{n_0} \frac{dn_1}{dt} \sim \frac{cB_x B_y}{4\pi ne\delta^2}, \quad (2.36)$$

where we used $J_z \sim cB_x/4\pi\delta$ and $\mathbf{B} \cdot \nabla \sim B_y/\delta$. From Eq. 2.33, we get

$$\frac{B_{z0}^2}{4\pi n_0 T} \frac{dB_{z1}}{dt} \sim \frac{cB_x B_y}{4\pi ne\delta^2}. \quad (2.37)$$

From the relation for v_x following Eq. 2.34, this gives

$$\frac{4\pi n_0 e\delta}{c\beta} \frac{dv_x}{dt} \sim \frac{cB_x B_y}{4\pi ne\delta^2}, \quad (2.38)$$

where we defined the plasma $\beta = 4\pi nT/B^2 \simeq 4\pi n_0T/B_{z0}^2$. Lastly, from the x component of the equation of motion,

$$\frac{dv_x}{dt} \sim \frac{1}{4\pi m_i n_0} (\mathbf{B} \cdot \nabla) B_x \sim \frac{B_y}{4\pi m_i n_0 \delta} B_x, \quad (2.39)$$

which when inserted into Eq. 2.38 gives

$$\delta \sim \rho_s, \quad (2.40)$$

where $\rho_s = \sqrt{\beta} d_i = c_s / \Omega_{ci}$ is the ion Larmor radius based on the sound speed $c_s = (T/m_i)^{1/2}$. Simulation results have confirmed this scaling [Kleva et al., 1995].

The thickness of the electron dissipation region is somewhat ambiguous, in that it depends on the dissipation mechanism. In a fluid model that does not include off diagonal (non-gyrotropic) elements of the electron pressure tensor, the effect which breaks the frozen-in law is the electron inertia. As such, for the same reason as in the anti-parallel case, the thickness of the electron layer is d_e . However, in a more realistic kinetic model, non-gyrotropic effects are automatically included, and numerical simulations suggest [Hesse et al., 2002, Hesse et al., 2004, Ricci et al., 2004, Swisdak et al., 2005] that the thickness of the electron layer can be smaller than d_e .

Simulations of strong guide field Hall reconnection suggest that the normalized reconnection rate E' is of the order of 0.1, just like in the anti-parallel case, but its scaling with system parameters has not been fully explored. Numerical simulations have found only a weak dependence on the reconnection rate for small guide fields [Hesse et al., 1999, Pritchett, 2001], but larger guide fields ($B_{z0} \sim 5B_{up}$) decrease the reconnection rate by a factor of 2 or 3 [Pritchett and Coroniti, 2004, Ricci et al., 2004, Huba, 2005].

Numerical simulations [Swisdak et al., 2005] have found that a guide field of only $B_{z0} \sim 0.1B_{up}$ is sufficient to make component reconnection effects important. Table 1.1 in Sec. 1.4 shows that fusion devices have a large guide field, while the magnetotail is close to the cross-over point between anti-parallel and component reconnection. The situation is not clear in the solar corona, where the conditions before onset are not well constrained by measurements. Laboratory experiments at VTF have a large guide field, while experiments at the Magnetic Reconnection Experiment (MRX) at the Princeton Plasma Physics Laboratory are anti-parallel.

2.4 Magnetic Reconnection and Linear Wave Analysis

As hinted at in Sec. 2.3, the generation of outflow due to the straightening of newly reconnected magnetic field lines is the driver of reconnection and controls how it proceeds. In Sec. 2.1.1, we motivated this process as a stretched field line reducing its tension. This process, just as in the straightening of a taut rubber band, is fundamentally a wave phenomenon. This is emphasized for the reconnection geometry in Fig. 2.7, which shows that a newly reconnected magnetic field line can be thought of as a half wavelength of an infinitely long standing wave train in the y direction [Drake and Shay, 2006] with a wavenumber $k \sim \pi/2\delta$ where δ is the half thickness of the dissipation region. Notice the flow generated by the wave corresponds to the outflow from reconnection, furthering the analogy. It is important to emphasize that the wave mediating the outflow is a standing wave, not a propagating one.

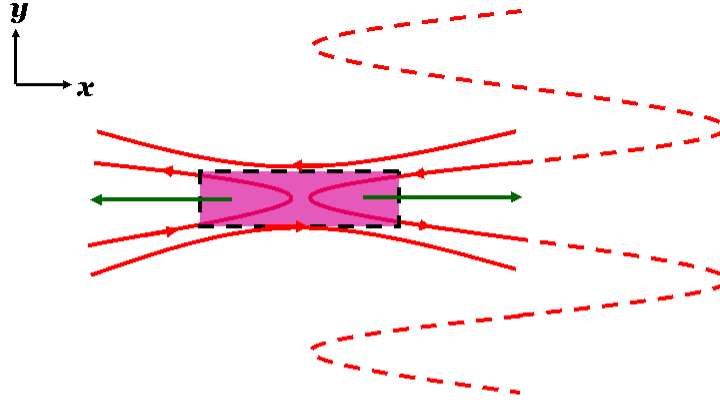


Figure 2.7: Motivation of reconnection outflow being mediated by waves, adapted from Ref. [Drake and Shay, 2006]. Note, the wavelength $\lambda \sim 4\delta$, so the wavenumber $k \sim \pi/2\delta$.

What is the nature of the waves mediating the outflow? In this section, we perform a linear wave analysis of the relevant governing equations. First, we consider waves in MHD, showing that the only waves available to generate outflow are Alfvén waves. This is appropriate for Sweet-Parker reconnection, where the dissipation region is wide enough for the MHD theory to be valid. However, if the thickness of the current sheet is small enough, the MHD description is no longer valid. A proper description of the waves generating the outflow from a dissipation region with a small thickness requires inclusion of the Hall effect. We analyze the waves in Hall-MHD, showing that the Hall effect introduces linear waves that are not present in MHD, namely the “whistler” and “kinetic Alfvén” waves, both of which are dispersive. These waves describe the generation of outflow from the dissipation region when the length scales are comparable to or smaller than the ion skin depth d_i and the ion Larmor radius ρ_s .

Recall that the Petschek open outflow configuration does not occur in MHD, but does occur in Hall-MHD. Is this difference due to the underlying wave structure of Hall-MHD? If so, what physically enables the open outflow? We discuss findings [Mandt et al., 1994, Rogers et al., 2001] that it is the existence of dispersive waves (introduced by the Hall effect) which plays a key role in setting up the Petschek open outflow configuration and, therefore, enabling fast reconnection.

2.4.1 Linear Waves in MHD

The governing equations of ideal-MHD, using Eqs. 2.3-2.7, can be written as

$$\frac{\partial n}{\partial t} + \nabla \cdot (n\mathbf{v}) = 0 \quad (2.41)$$

$$m_i n \left[\frac{\partial \mathbf{v}}{\partial t} + (\mathbf{v} \cdot \nabla) \mathbf{v} \right] = -\nabla \left(nT + \frac{1}{8\pi} \mathbf{B} \cdot \mathbf{B} \right) + \frac{1}{4\pi} (\mathbf{B} \cdot \nabla) \mathbf{B} \quad (2.42)$$

$$\frac{\partial \mathbf{B}}{\partial t} = \nabla \times (\mathbf{v} \times \mathbf{B}), \quad (2.43)$$

where we use $p = nT$ with a constant and uniform temperature T for simplicity. We linearize about a stationary ($\mathbf{v}_0 = 0$) plasma of uniform density n_0 with a uniform and constant magnetic field \mathbf{B}_0 by replacing n by $n_0 + n_1$, etc., in Eqs. 2.41 - 2.43 and ignoring terms of second order smallness in the perturbed quantities, giving

$$\frac{\partial n_1}{\partial t} + n_0 \nabla \cdot \mathbf{v}_1 = 0 \quad (2.44)$$

$$m_i n_0 \frac{\partial \mathbf{v}_1}{\partial t} = -\nabla \left(T n_1 + \frac{1}{4\pi} \mathbf{B}_0 \cdot \mathbf{B}_1 \right) + \frac{1}{4\pi} (\mathbf{B}_0 \cdot \nabla) \mathbf{B}_1 \quad (2.45)$$

$$\frac{\partial \mathbf{B}_1}{\partial t} = (\mathbf{B}_0 \cdot \nabla) \mathbf{v}_1 - \mathbf{B}_0 (\nabla \cdot \mathbf{v}_1). \quad (2.46)$$

From our expectations pictured in Fig. 2.7, we take $\mathbf{B}_0 = B_{y0} \hat{\mathbf{y}}$ and consider perturbed quantities depending only on y , with flow and field perturbations in the x

direction⁹, ($\mathbf{v}_1 = v_{x1}(y)\hat{\mathbf{x}}$, $\mathbf{B}_1 = B_{x1}(y)\hat{\mathbf{x}}$). This velocity perturbation is incompressible ($\nabla \cdot \mathbf{v}_1 = 0$), so Eq. 2.44 immediately gives $n_1 = 0$. The equation of motion and Faraday's Law give

$$\frac{\partial v_{x1}}{\partial t} = \frac{B_{y0}}{4\pi m_i n_0} \frac{\partial B_{x1}}{\partial y} \quad (2.47)$$

$$\frac{\partial B_{x1}}{\partial t} = B_{y0} \frac{\partial v_{x1}}{\partial y}. \quad (2.48)$$

Solving by Fourier Transform with the ansatz of a standing wave

$$v_{x1} = \frac{1}{2} \tilde{v}_x [\exp(ik_y y - i\omega t) + \exp(ik_y y + i\omega t)] \quad (2.49)$$

$$B_{x1} = \frac{1}{2} \tilde{B}_x [\exp(ik_y y - i\omega t) + \exp(ik_y y + i\omega t)] \quad (2.50)$$

yields a dispersion relation of

$$\omega^2 = k_y^2 c_{Ay}^2, \quad (2.51)$$

where $c_{Ay} = B_{y0}/(4\pi m_i n_0)^{1/2}$ is the Alfvén speed based on the equilibrium (vertical) magnetic field. The phase speed $v_{ph} = \omega/k_y$ is just the Alfvén speed, independent of the wavelength, so these waves are non-dispersive. Substituting Eq. 2.51 into the Fourier Transform of Eq. 2.47 yields the important result

$$\tilde{v}_x = -\frac{\tilde{B}_x}{\sqrt{4\pi m_i n_0}}, \quad (2.52)$$

namely, the amplitude of the velocity perturbation is the Alfvén speed based on the horizontal (x) component of the magnetic field. This is consistent with the

⁹Taking the equilibrium field in the y direction may seem counterintuitive, as the reconnecting field is in the x direction. However, to create the wave train in Fig. 2.7, one needs a field in the y direction with a perturbation in the x direction.

interpretation that the outflow from the X-line is generated by the straightening of magnetic field lines, as this is the same result obtained in Eqs. 2.2 and 2.11.

We note in passing that the inclusion in the equilibrium of a uniform guide field of any size, $\mathbf{B}_0 = B_{y0}\hat{\mathbf{y}} + B_{z0}\hat{\mathbf{z}}$, does not alter the above analysis; the outflow speed is still the Alfvén speed based on the *horizontal* component of the magnetic field B_x . This is in agreement with the observation that a guide field does not play a role in Sweet-Parker reconnection.

2.4.2 Linear Waves in Hall-MHD

We repeat the analysis of the previous section using the equations of Hall-MHD. First, we consider the case of no guide field. The governing equations are again Eqs. 2.3-2.6, but the Ohm's Law in Eq. 2.7 is replaced by Eq. 2.24, giving

$$\frac{\partial n}{\partial t} + \nabla \cdot (n\mathbf{v}) = 0 \quad (2.53)$$

$$m_i n \left[\frac{\partial \mathbf{v}}{\partial t} + (\mathbf{v} \cdot \nabla) \mathbf{v} \right] = -\nabla \left(nT + \frac{1}{8\pi} \mathbf{B} \cdot \mathbf{B} \right) + \frac{1}{4\pi} (\mathbf{B} \cdot \nabla) \mathbf{B} \quad (2.54)$$

$$\frac{\partial \mathbf{B}}{\partial t} = \nabla \times \left[\mathbf{v} \times \mathbf{B} - \frac{\mathbf{J} \times \mathbf{B}}{ne} - \frac{m_e c}{e^2} \frac{d\mathbf{J}/n}{dt} \right], \quad (2.55)$$

where we have dropped the resistive and off diagonal pressure tensor terms and the scalar electron pressure term is annihilated by the curl in Faraday's Law. As in the previous section, we linearize about $n_0, \mathbf{v}_0 = 0$ and \mathbf{B}_0 , giving

$$\frac{\partial n_1}{\partial t} + n_0 \nabla \cdot \mathbf{v}_1 = 0 \quad (2.56)$$

$$m_i n_0 \frac{\partial \mathbf{v}_1}{\partial t} = -\nabla \left(T n_1 + \frac{1}{4\pi} \mathbf{B}_0 \cdot \mathbf{B}_1 \right) + \frac{1}{4\pi} (\mathbf{B}_0 \cdot \nabla) \mathbf{B}_1 \quad (2.57)$$

$$(1 - d_e^2 \nabla^2) \frac{\partial \mathbf{B}_1}{\partial t} = (\mathbf{B}_0 \cdot \nabla) \mathbf{v}_1 - \mathbf{B}_0 (\nabla \cdot \mathbf{v}_1) - \frac{1}{n_0 e} (\mathbf{B}_0 \cdot \nabla) \mathbf{J}_1, \quad (2.58)$$

where $d_e = \sqrt{m_e c^2 / 4\pi n_0 e^2}$ is the electron skin depth and $\mathbf{J}_1 = (c/4\pi)\nabla \times \mathbf{B}_1$ from Eq. 2.6. The only changes from MHD are in the third equation which includes corrections due to the Hall effect and electron inertia. As in the previous section, take $\mathbf{B}_0 = B_{y0}\hat{\mathbf{y}}$ and consider y dependent perturbations. However, using the same perturbations as in the previous section does not work. Why? In the z component of Eq. 2.58, if $\mathbf{B}_1 = B_{x1}(y)\hat{\mathbf{x}}$, then J_{z1} is non-zero, leading to the generation of a B_{z1} from the Hall effect. Physically, the Hall term is generating an out of plane magnetic field B_{z1} , as described in Sec. 2.3 (see Fig. 2.5). Thus, the perturbations must have z components, *i.e.*, $\mathbf{B}_1 = B_{x1}(y)\hat{\mathbf{x}} + B_{z1}(y)\hat{\mathbf{z}}$ and $\mathbf{v}_1 = v_{x1}(y)\hat{\mathbf{x}} + v_{z1}(y)\hat{\mathbf{z}}$. With this ansatz, the perturbation is again incompressible, $n_1 = 0$. The standing wave Fourier Transform of Eqs. 2.57 and 2.58 reduce to

$$\omega \mathbf{v}_1 = -\frac{k_y B_{y0}}{4\pi m_i n_0} \mathbf{B}_1 \quad (2.59)$$

$$\omega(1 + k_y^2 d_e^2) \mathbf{B}_1 = -k_y B_{y0} \mathbf{v}_1 + i k_y^2 c_{Ay} d_i (\hat{\mathbf{y}} \times \mathbf{B}_1) \quad (2.60)$$

where $d_i = \sqrt{m_i c^2 / 4\pi n_0 e^2}$ is the ion skin depth. This gives a dispersion relation of [Wang et al., 2000, Rogers et al., 2001]

$$\omega^2 = \frac{k_y^2 c_{Ay}^2}{D} \left(1 + \frac{k_y^2 d_i^2}{2D} + \sqrt{\frac{k_y^2 d_i^2}{D} + \frac{k_y^4 d_i^4}{4D^2}} \right) \quad (2.61)$$

where $D = 1 + k_y^2 d_e^2$.

The dispersion relation $\omega(k_y)$ is plotted in Fig. 2.8a. For long wavelengths ($k_y d_i \ll 1$), this is just the Alfvén wave with $\omega^2 = k_y^2 c_{Ay}^2$, plotted as the straight dashed line. For intermediate wavelengths ($k_y d_e \ll 1 \ll k_y d_i$), this is the whistler wave with $\omega = k_y^2 c_{Ay} d_i$, plotted as the dashed curve. Whistler waves are circularly

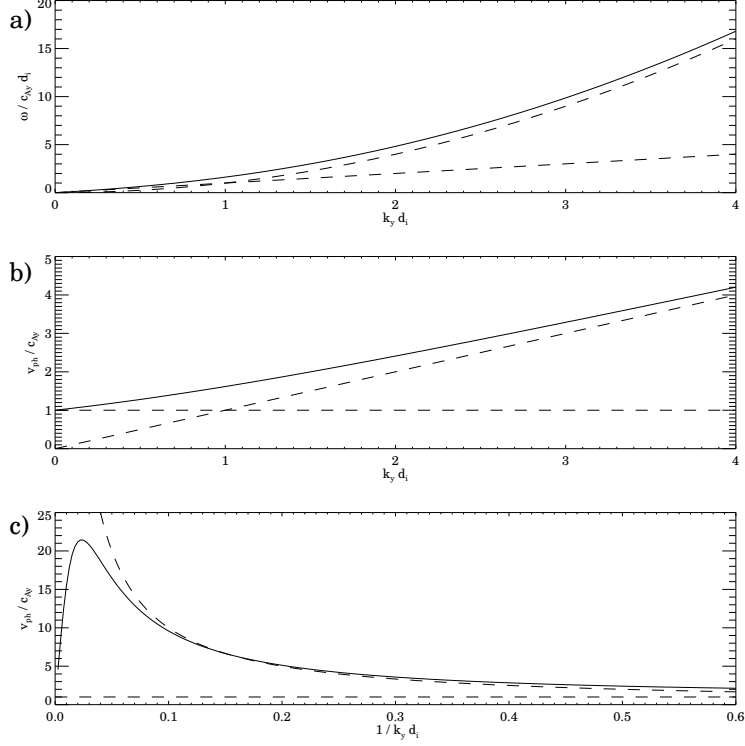


Figure 2.8: (a) Dispersion relation and phase speed as a function of (b) wavenumber and (c) inverse wavenumber for Hall-MHD waves. Dashed lines are pure Alfvén and whistler waves.

polarized waves with $|B_{x1}| = |B_{z1}|$. (See Ref. [Shay, 1998] for a more thorough description of whistler physics.) Note, since ω/k_y for the whistler wave is proportional to k_y , it is dispersive. Non-MHD effects become important at a length scale of d_i , in agreement with the scaling analysis of Sec. 2.3.1. For very short wavelengths ($k_y d_e \gg 1$), the Hall-MHD waves become electron cyclotron waves with $\omega = \Omega_{ce} = eB_{y0}/m_e c$, not shown in Fig. 2.8a. The phase speed $v_{ph} = \omega(k_y)/k_y$ is plotted as a function of wavenumber in Fig. 2.8b and length scale (inverse wavenumber) in Fig. 2.8c. It is Alfvénic for long wavelengths and increases for length scales below d_i , reaching a peak of half the electron Alfvén speed $c_{Ae}/2$ at a length scale

of $1/k \sim d_e$.

Substituting Eq. 2.61 into Eq. 2.59 gives

$$\tilde{v}_x = -\frac{k_y B_{y0}}{4\pi m_i n_0 \omega(k_y)} \tilde{B}_x = -\frac{c_{Ay}}{v_{ph}(k_y)} \frac{\tilde{B}_x}{\sqrt{4\pi m_i n_0}}. \quad (2.62)$$

As with MHD waves, the amplitude of the velocity perturbation corresponds to the outflow speed of reconnection. The expected outflow speed from the ion dissipation region of thickness d_i is (using $k_y \sim 1/d_i$) $\tilde{v}_x \sim c_{Ax} = \tilde{B}_x / (4\pi m_i n_0)^{1/2}$, the Alfvén speed based on the horizontal magnetic field. For the outflow from the electron dissipation region, one must find the electron flow perturbation using $\tilde{v}_{ex} = \tilde{v}_x - \tilde{J}_x / n_0 e$. From Eqs. 2.59 and 2.60, one gets

$$\tilde{v}_{ex} = -\frac{\omega(k_y) D}{k_y c_{Ay}} \frac{\tilde{B}_x}{\sqrt{4\pi m_i n_0}}. \quad (2.63)$$

Evaluating this at the electron dissipation thickness scale of $k_y \sim 1/d_e$ gives $\tilde{v}_{ex} \sim c_{Aex} = \tilde{B}_x / (4\pi m_e n_0)^{1/2}$, *i.e.*, the electron Alfvén speed based on the horizontal (x) component of the magnetic field. These conclusions agree with the outflow speeds from the ion and electron dissipation regions during Hall reconnection as discussed in Sec. 2.3.1.

2.4.3 Linear Waves in Hall-MHD with a Strong Guide Field

Consider the effect of a guide field on Hall-MHD waves, *i.e.*, let $\mathbf{B}_0 = B_{y0} \hat{\mathbf{y}} + B_{z0} \hat{\mathbf{z}}$. The linearized equations of the previous section, Eqs. 2.56 - 2.58, still hold. However, if we use the same perturbations as in the previous section, the analysis does not work. Why? In the y component of the equation of motion, the $\mathbf{B}_0 \cdot \mathbf{B}_1$

term vanishes in the zero guide field case, *i.e.*, the perturbation B_{z1} does not alter the magnetic pressure to first order. However, with a guide field of B_{z0} , the B_{z1} perturbation *does* alter the magnetic pressure to first order. Thus, the y component of the equation of motion cannot be consistent with the perturbation used in the previous section. In particular n_1 must be non-zero; waves in Hall-MHD with a guide field are compressible. (This is the same effect discussed in Sec. 2.3.2 which leads to density cavities during component Hall-MHD reconnection.) The velocity perturbation must be of the form $\mathbf{v}_1 = v_{x1}(y)\hat{\mathbf{x}} + v_{y1}(y)\hat{\mathbf{y}} + v_{z1}(y)\hat{\mathbf{z}}$ to satisfy Eq. 2.56. The magnetic field perturbation still only has x and z components¹⁰.

Since these waves are complicated, we treat a special case to elucidate the minimal physics required. Consider the large guide field limit, $B_{z0} \gg B_{y0}$, where $c_A \simeq c_{Az}$ is the largest speed in the system, *i.e.*, the plasma $\beta = c_s^2/c_A^2 \simeq 4\pi n_0 T/B_{z0}^2 \ll 1$. For compressibility in the y direction to dominate magnetic effects normal to the guide field, we require $c_s \gg c_{Ay}$, *i.e.*, that the plasma β based on the in-plane magnetic field $\beta_{rec} = c_s^2/c_{Ay}^2 = 4\pi n_0 T/B_{y0}^2 \gg 1$. In this limit, we can ignore the ion inertia term in the y component of the equation of motion (Eq. 2.57) relative to the pressure term, giving

$$n_1 = -\frac{B_{z0}}{4\pi T} B_{z1}, \quad (2.64)$$

just like Eq. 2.33. The x component of the equation of motion (Eq. 2.57) is

$$\omega v_{x1} = -\frac{\mathbf{k} \cdot \mathbf{B}_0}{4\pi m_i n_0} B_{x1}, \quad (2.65)$$

the same as it was in Eq. 2.59 without a guide field. Since the wave is compressible,

¹⁰If there was a y component, $\nabla \cdot \mathbf{B}_1 = 0$ would not be satisfied.

we need the continuity equation, Eq. 2.56, the Fourier Transform of which gives

$$\omega n_1 = n_0 \mathbf{k} \cdot \mathbf{v}_1. \quad (2.66)$$

The final two equations come from Faraday's Law, Eq. 2.58. The x component gives

$$\omega DB_{x1} = -(\mathbf{k} \cdot \mathbf{B}_0) v_{x1} + \frac{ic}{4\pi n_0 e} (\mathbf{k} \cdot \mathbf{B}_0) k_y B_{z1}, \quad (2.67)$$

where $D = 1 + k_y^2 d_e^2$, just like Eq. 2.60 without a guide field. Finally, in the z component, we again use that the guide field is large, which allows us to ignore the $(\mathbf{B} \cdot \nabla) v_{z1}$ term relative to the compression term $B_{z0}(\nabla \cdot \mathbf{v}_1)$ term, leaving

$$\omega DB_{z1} = B_{z0} (\mathbf{k} \cdot \mathbf{v}_1) - \frac{ic}{4\pi n_0 e} (\mathbf{k} \cdot \mathbf{B}_0) k_y B_{x1}. \quad (2.68)$$

Eliminating the perturbations from Eqs. 2.64 - 2.68 yields a dispersion relation of

$$\omega^2 = \frac{k_y^2 c_{Ay}^2}{D} \left(1 + \frac{k_y^2 \rho_s^2}{1 + \beta D} \right), \quad (2.69)$$

where $\rho_s = c_s / \Omega_{ci} = \beta^{1/2} d_i$ is the ion Larmor radius based on the sound speed.

The dispersion relation $\omega(k_y)$ is plotted in Fig. 2.9a for $\beta = 0.1$. For long wavelengths ($k_y \rho_s \ll 1$), this is just the Alfvén wave with $\omega^2 = k_y^2 c_{Ay}^2$, plotted as the straight dashed line in Fig. 2.9a. For intermediate wavelengths ($k_y d_e \ll 1 \ll k_y \rho_s$), this is the kinetic Alfvén wave with $\omega = k_y^2 c_{Ay} \rho_s$, plotted as the dashed curve. The kinetic Alfvén wave, just like the whistler, is dispersive with $v_{ph} \propto k_y$. Non-MHD effects become important at a length scale of ρ_s , in agreement with the scaling argument in Sec. 2.3.2. For short wavelengths ($k_y d_e \gg 1$), this is the electron cyclotron wave with $\omega = \Omega_{ce} = eB_{y0}/m_e c$, just as in Hall-MHD without the guide field.

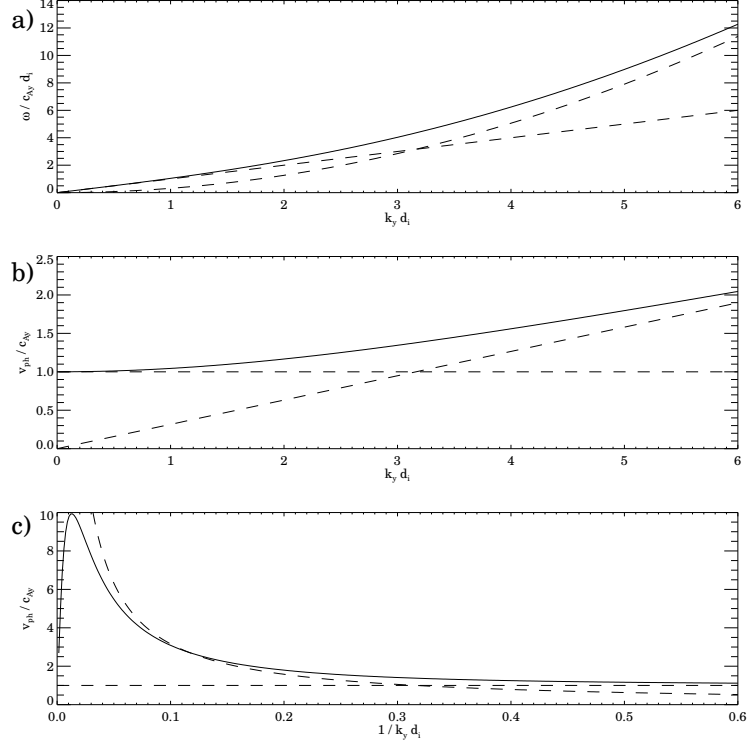


Figure 2.9: (a) Dispersion relation and phase speed as a function of (b) wavenumber and (c) inverse wavenumber for Hall-MHD waves with a strong guide field. Dashed lines are pure Alfvén and kinetic Alfvén waves. This plot has $\beta = 0.1$, which gives $\rho_s \simeq 0.32d_i$.

The phase speed $v_{ph} = \omega(k_y)/k_y$ is plotted as a function of wavenumber in Fig. 2.9b and length scale (inverse wavenumber) in Fig. 2.9c. It is Alfvénic for long wavelengths, and increases for length scales below ρ_s , reaching a peak of $v_{ph} = (\beta d_i^2/2d_e^2)^{1/2} c_{Ay}$ at $kd_e \sim 1$. Just as in the no-guide field case, the ion and electron velocity perturbations satisfy Eq. 2.62 and 2.63. The ion outflow at $k \sim 1/\rho_s$ is $\tilde{v}_x \sim c_{Ax} = \tilde{B}_x/(4\pi m_i n_0)^{1/2}$, the Alfvén speed based on the horizontal magnetic field, in agreement with simulation results. The outflow speed from an electron layer of thickness d_e is $\tilde{v}_{ex} \sim (2\beta)^{1/2} \tilde{B}_x/(4\pi m_e n_0)^{1/2}$. This would suggest that the

outflow speed from an electron layer of thickness d_e has this velocity. A thorough testing in a kinetic model has not yet been completed.

It is important to remember that both the Hall and electron pressure gradient terms must be present to capture kinetic Alfvén physics. It is the Hall effect which generates the out of plane magnetic field perturbation, and if the electrons and ions were cold, there could be no compression and, therefore, no way to balance the change in magnetic pressure due to the perturbation from the Hall effect.

2.4.4 The Relation of Dispersive Waves to Fast Reconnection

Why is Sweet-Parker slow but Hall reconnection fast? The importance of dispersive waves was pointed out in Ref. [Mandt et al., 1994]. In Sweet-Parker reconnection, the only waves available for mediating outflow are Alfvén waves, which are non-dispersive. Therefore, the outflow speed is the same for a sheet of any thickness. For thinner sheets, the mass flux out of the end of the layer, $v_{out}\delta$, becomes smaller, and the flow is held back. In Hall reconnection, the outflow is mediated by whistler or kinetic Alfvén waves, which are dispersive with $v_{out} \propto k_y$. Since $k_y \sim 1/\delta$ (see Fig. 2.7), the mass flux out of the dissipation region $v_{out}\delta \sim k_y\delta$ stays approximately constant as the layer gets thinner because the outflow gets faster. This makes the reconnection rate $v_{in} \sim v_{out}\delta/L$ independent of the thickness of the dissipation region and, therefore, independent of the dissipation mechanism itself, in agreement with the simulation results.

To test the hypothesis that the existence of dispersive waves is intimately re-

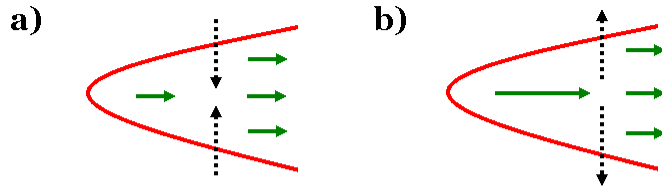


Figure 2.10: Motivation for why dispersive waves lead to Petschek's open outflow configuration yet non-dispersive waves do not.

lated to the realizability of fast reconnection, a careful study of the linear wave theory of Hall-MHD was performed for arbitrary B_{z0} and T in Ref. [Rogers et al., 2001]. It was found that the only dispersive waves available to Hall-MHD are whistler waves and kinetic Alfvén waves. Furthermore, numerical simulations confirmed that reconnection is fast in those regimes in which dispersive waves are present, and is slow and Sweet-Parker like in the other regimes.

Why do dispersive waves in Hall-MHD lead to the Petschek configuration and, thus, fast magnetic reconnection, and why does the absence of dispersive waves in MHD prevent it? A simple cartoon can help motivate the relevant physics [Drake and Shay, 2006]. Suppose one could set up Petschek's open outflow configuration in a system obeying MHD. Fig. 2.10a shows the region downstream of the dissipation region, with the outflow in green. The outflow is generated by non-dispersive Alfvén waves, so the outflow speed is the same at all vertical distances from the X-line. Since the outflow region opens out, there is more mass flux $v_{out}\delta$ further downstream, *i.e.*, $d(v_{out}\delta)/dx > 0$. From continuity, this requires an inflow, $d(v_{in}L)/dy < 0$, shown as the dashed black line in Fig. 2.10a. This in-

flow pulls the fields in, collapsing the open outflow region into a long thin layer, leading to the Sweet-Parker configuration, as observed in numerical simulations [Biskamp, 1986, Scholer, 1989, Uzdensky and Kulsrud, 2000].

In contrast, the waves mediating the outflow in Hall reconnection are whistler or kinetic Alfvén waves at length scales below the ion dissipation region. Since these waves are dispersive, the outflow speed is faster closer to the X-line where the sheet is thinner and slower further downstream where the sheet is thicker, as depicted in Fig. 2.10b. Thus, the outflow gets smaller as one goes further downstream $dv_{out}/dx < 0$, and continuity requires a vertical outflow away from the neutral line $dv_{in}/dy > 0$, as shown by the black dashed line in Fig. 2.10b. It is this upflow of the electron fluid which supports the Petschek open outflow configuration, leading to fast magnetic reconnection.

2.5 Summary

In summary, magnetic reconnection is the process by which small scale dissipation facilitates the release of magnetic energy by allowing a change in topology of the magnetic field into a configuration in which energy conversion is energetically favorable. The outflow generated by the energy conversion process generates inflow of more magnetic fields into the dissipation region, which makes magnetic reconnection self-driven. A steady-state is reached when the rate at which magnetic field lines convected toward the X-line is balanced by the rate of diffusion of field lines within the dissipation region.

In the Sweet-Parker model, magnetic diffusion provides the dissipation which allows the magnetic field lines to break. The reconnection is exceedingly slow because the collisionality in plasmas of interest is low and a high aspect ratio nozzle forms, throttling the process. In Hall reconnection, the outflow is mediated by dispersive waves introduced by the Hall effect, which opens the outflow region into the Petschek configuration, leading to fast reconnection. In the next chapter, we begin the discussion of reconnection dynamics by determining under what conditions the Sweet-Parker and Hall models can achieve a steady-state.

Chapter 3

Dynamics of Magnetic Reconnection

In the previous chapter, we discussed the Sweet-Parker and Hall models of steady-state magnetic reconnection. However, it was not discussed under what conditions these solutions can exist. Clearly, the collisional Sweet-Parker solution is valid for large enough resistivity η , while the collisionless Hall solution is valid for small enough η . What happens as one varies η ? When does reconnection switch from Sweet-Parker to Hall and vice versa? Is the transition from one to the other smooth or abrupt? These questions were answered in Ref. [Cassak et al., 2005].

In Sec. 3.1, we determine the parameter regimes in which the Sweet-Parker and Hall solutions can exist. The results imply that the two solutions are independently valid for a given value of a control parameter (reconnection is bistable) for a wide range of parameter space, as discussed in Sec. 3.2. Resistive Hall-MHD numerical simulations are used to verify the theory. The numerics are described in Sec. 3.3 and the results for anti-parallel and component reconnection are discussed in Sec. 3.4. Finally, recent relevant experimental results at the Magnetic Reconnection Experiment (MRX) are discussed in Sec. 3.5.

3.1 Validity Conditions of Steady-State Reconnection Models

In Sec. 2.1.2, we showed that magnetic reconnection is manifestly a non-ideal-MHD phenomenon. Non-ideal effects are described by the generalized Ohm's Law, Eq. 2.24, in which the resistive, Hall, electron pressure gradient, and electron inertia terms contribute to the electric field. The validity of the steady-state Sweet-Parker (Hall) model, then, requires that the dominant contribution to the reconnection electric field E is the resistive (Hall) term.

In Sweet-Parker reconnection, it was shown in Eq. 2.20 that the thickness δ_{SP} of the Sweet-Parker dissipation region is

$$\delta_{SP} = L_{SP} \sqrt{\frac{\eta c^2}{4\pi c_{Aup} L_{SP}}}. \quad (3.1)$$

where L_{SP} is the half-length of the Sweet-Parker dissipation region. In Secs. 2.3 and 2.4, we showed that the Hall effect becomes important at a length scale of the ion skin depth d_i for anti-parallel reconnection and the ion Larmor radius ρ_s for component reconnection. Thus, quite simply, the Sweet-Parker solution is valid provided the Sweet-Parker dissipation region is thicker than the appropriate length scale,

$$\begin{aligned} \delta_{SP} > d_i & \quad \text{for anti-parallel,} \\ \delta_{SP} > \rho_s & \quad \text{for component.} \end{aligned} \quad (3.2)$$

Using Eq. 3.1, this can be written as

$$\frac{\eta c^2}{4\pi} > \frac{d_i^2 c_{Aup}}{L_{SP}} \quad \text{for anti-parallel,} \quad (3.3)$$

and

$$\frac{\eta c^2}{4\pi} > \frac{\rho_s^2 c_{Aup}}{L_{SP}} \quad \text{for component,} \quad (3.4)$$

which quantifies the statement that Sweet-Parker reconnection is valid for large enough resistivities. It also implies that if a system is undergoing Sweet-Parker reconnection and the resistivity is decreased, Sweet-Parker reconnection will continue as long as this condition is satisfied.

Physically, if one were to try to make a Sweet-Parker layer thinner than the appropriate length scale (d_i for anti-parallel, ρ_s for component), the ions outside the layer would decouple from the magnetic field, allowing the fields to move faster and creating an in-plane current. The Hall electric field would overpower the resistive electric field, driving the system to the Hall solution. This can also be interpreted in terms of the underlying waves. For waves with wavelengths longer than d_i and ρ_s , Hall-MHD waves are simply Alfvén waves (see Sec. 2.4), so reconnection will be just as in resistive-MHD. For shorter wavelengths, the dispersiveness of the whistler or kinetic Alfvén waves sets up the Petschek open outflow configuration (see Sec. 2.4.4).

In contrast, Hall reconnection is valid if the Hall electric field in Eq. 2.24 is larger than the resistive term,

$$\eta J_z < \frac{J_y B_x}{nec} \sim \frac{v_{in,e} B_x}{c}, \quad (3.5)$$

where $J_y \sim v_{in,e}/ne$ where $v_{in,e}$ is the inflow speed of electrons into the electron dissipation region because the ions are demagnetized during Hall reconnection. Since the current is carried by the electrons, $J_z \sim cB_{up,e}/4\pi\delta_e$ where δ_e is the thickness of the electron dissipation region and $B_{up,e}$ is the magnetic field strength immediately upstream of the electron dissipation region, so Hall reconnection is valid provided

$$\frac{\eta c^2}{4\pi} < v_{in,e} \delta_e, \quad (3.6)$$

as was first stated in Ref. [Shay et al., 2001].

How do δ_e and $v_{in,e}$ scale with system parameters? In the Hall reconnection simulations to be discussed in this thesis, the electron frozen-in condition is broken by the electron inertia term in Eq. 2.24, so the dissipation region has a thickness of the electron skin depth $\delta_e \sim d_e$. During anti-parallel reconnection, the inflow speed scales like $v_{in,e} \sim 0.1c_{Aeup}$ [Shay et al., 1999, Huba and Rudakov, 2004], where c_{Aeup} is the electron Alfvén speed based on the magnetic field $B_{up,e}$ immediately upstream of the electron dissipation region. As discussed in Sec. 2.4.2, this speed is also the electron flow speed of the whistler wave evaluated at $k_y \sim 1/d_e$. For component reconnection, the scaling of the inflow speed with system parameters has not been fully explored. By analogy with the anti-parallel result, one might expect the outflow speed for component reconnection to be the electron flow speed of the kinetic Alfvén wave evaluated at $\delta_e \sim d_e$, which scales like $\beta^{1/2}c_{Aeup}$ where $\beta = c_s^2/c_A^2$ is the plasma β , as discussed in Sec. 2.4.3. While this result has not been established numerically, results of a benchmark simulation are consistent with this scaling. Taking the inflow speed $v_{in,e}$ to scale like 0.1 of the electron flow speed, Eq. 3.6 can be written as

$$\frac{\eta c^2}{4\pi} < 0.1c_{Aup,e}d_e \sim 0.1c_{Aup}d_i \frac{B_{up,e}}{B_{up}} \quad \text{for anti-parallel,} \quad (3.7)$$

and

$$\frac{\eta c^2}{4\pi} < 0.1\beta^{1/2}c_{Aup,e}d_e \sim 0.1\beta^{1/2}c_{Aup}d_i \frac{B_{up,e}}{B_{up}} \quad \text{for component,} \quad (3.8)$$

where c_{Aup} is the ion Alfvén based on the magnetic field B_{up} upstream of the *ion* dissipation region. It is difficult to predict what $B_{up,e}/B_{up}$ will be, but it is expected to be greater than $d_e/d_i = (m_e/m_i)^{1/2}$ and less than 1. Equations 3.7 and 3.8

quantify the statement that Hall reconnection is valid provided the resistivity is small enough. It also implies that if a system is undergoing Hall reconnection and the resistivity is increased, it will remain in the Hall configuration as long as Eq. 3.7 or 3.8 is satisfied.

Physically, if one were to try to set up a Hall layer in a system where the resistivity is too large, the electron dissipation region would diffuse out to the ion layer, and the ions and electrons would no longer be decoupled. The dispersive waves required for Hall reconnection would not exist, and the dissipation region would collapse into a Sweet-Parker layer. We will see in the next section that the right hand sides of Eqs. 3.7 and 3.8 are exceedingly large, so the resistivity would have to be unrealistically large for it to play any role whatsoever during Hall reconnection¹.

3.2 Bistability and Hysteresis of Magnetic Reconnection

There is a very interesting consequence of the validity conditions found in the previous section. Since the Hall term is many orders of magnitude larger during Hall reconnection than it is during Sweet-Parker reconnection, dominance of the resistive term happens at vastly different values for the two reconnection configurations. Thus, it is possible to have a resistivity that simultaneously satisfies both Eq. 3.3 and 3.7 during anti-parallel reconnection or Eqs. 3.4 and 3.8 for component reconnection.

¹Eq. 3.7 can also be written as $\nu_{ei} \ll 0.1 \frac{B_{up,e}}{B_{up}} \Omega_{ce}$, where $\nu_{ei} = \eta m_e^2 / m_e$ is the electron-ion collision frequency and $\Omega_{ce} = eB / m_e c$ is the electron cyclotron frequency. This makes it more apparent that the condition is typically easily satisfied in Nature.

In this event, both the Sweet-Parker and Hall solutions independently exist. When a system can be in either of two stable steady-state solutions for a given value of a control parameter, the system is known as “bistable” or “bimodal”. We will see that there is a wide range of resistivities for which reconnection is bistable.

It is convenient to define a dimensionless parameter

$$\eta' = \frac{\eta c^2}{4\pi c_{Aup} d_i}, \quad (3.9)$$

a normalized resistivity which is an inverse Lundquist number based on the ion skin depth d_i and the Alfvén speed c_{Aup} based on the magnetic field upstream of the ion dissipation region. In terms of this quantity, the condition that the Sweet-Parker solution exists (Eqs. 3.3 and 3.4) becomes

$$\eta' > \eta'_{sf}, \quad (3.10)$$

where $\eta'_{sf} \sim d_i/L_{SP}$ is the critical value of η' at which the Sweet-Parker solution disappears for anti-parallel reconnection or $\eta'_{sf} \sim \rho_s^2/d_i L_{SP} = \beta d_i/L_{SP}$ for component reconnection. This is shown as the lower line in Fig. 3.1, a schematic plot of the normalized Sweet-Parker reconnection rate $E'_{SP} \propto (\eta')^{1/2}$ as a function of η' (see Eq. 2.20). When lowering η' from large values, η'_{sf} is the value of η' at which a slow-to-fast transition will occur.

The condition that the Hall solution exists (Eqs. 3.7 and 3.8) likewise becomes

$$\eta' < \eta'_{fs}, \quad (3.11)$$

where $\eta'_{fs} \sim 0.1 B_{up,e}/B_{up}$ is the critical value of η' at which the Hall solution disappears for anti-parallel reconnection or $\eta'_{fs} \sim 0.1 \beta^{1/2} B_{up,e}/B_{up}$ for component recon-

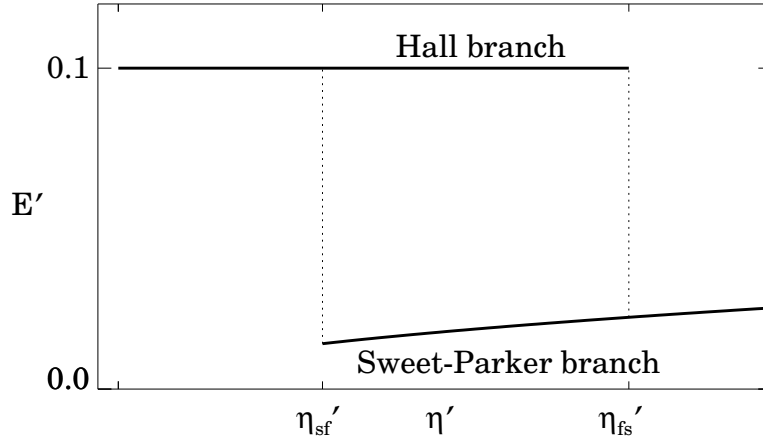


Figure 3.1: Schematic diagram of the steady-state normalized reconnection rate E' as a function of normalized resistivity η' for the Sweet-Parker and Hall reconnection models.

nection. When increasing η' from zero, η'_{fs} is the value of η' at which a fast-to-slow transition will occur. This is plotted as the upper line in Fig. 3.1, using $E'_H \sim 0.1$ independent of η' during Hall reconnection. The two curves in Fig. 3.1 taken together show that the system is bistable for η' between η'_{sf} and η'_{fs} , while only a single solution exists outside of this range. To get a feel for these scales, $\eta'_{sf} \simeq 4 \times 10^{-7}$ and $\eta'_{fs} \sim 2 \times 10^{-3}$ to 0.1 for the solar flare parameters listed in Table 1.1 in Sec. 1.4 assuming anti-parallel reconnection. Therefore, these scales are separated by four to six orders of magnitude, showing that a very large range of η' is bistable.

A corollary to the bistable nature of magnetic reconnection is that it is history dependent; a system undergoing magnetic reconnection can undergo hysteresis. Suppose a system is in the Sweet-Parker configuration with a normalized resistivity η' between η'_{sf} and η'_{fs} . If one lowers η' below η'_{sf} , the Sweet-Parker solution ceases

to exist and the system must make a transition to Hall reconnection. If η' is raised back to its original value, the system will remain in Hall reconnection. This is a classic example of hysteresis.

Why is it that reconnection is bistable instead of a hybrid of the two reconnection models? This can be motivated using the wave model. Hall reconnection is mediated by dispersive waves, either the whistler or kinetic Alfvén waves, with $\omega \propto k_y^2$. However, damping due to diffusion alone is given by $\omega = -ik_y^2 \eta c^2 / 4\pi$ (see Eq. 2.16 and drop the convection term). Since both effects scale like k_y^2 , whichever effect dominates at one spatial scale will dominate at all scales; the two effects cannot coexist [Birn et al., 2001].

The incompatibility of the two effects suggests that the transition between the two solutions is abrupt, as depicted schematically in Fig. 3.1. This has profound implications for the Onset Problem, as we discuss further in Chapter 6. Before exploring this interesting dynamics further, we show results of numerical simulations which verify the theory presented here.

3.3 Description of Numerics

All numerical simulations presented in this thesis were performed on 64 processors at the IBM SP machine, Seaborg, operated by the National Energy Research Scientific Computing Center (see <http://www.nersc.gov>) using the massively parallel code F3D [Shay et al., 2004]. The code solves the equations of resistive Hall-MHD, namely Eqs. 2.3 - 2.6, and 2.24. The time derivative in the electron inertia term

on the right hand side of Eq. 2.24 is handled by simultaneously advancing \mathbf{B} and \mathbf{J} . This is done by assuming the density in the electron inertia term is essentially a constant of $n \sim n_0$ under the action of the derivative, which gives

$$\frac{d}{dt} \left(\frac{\mathbf{J}}{n} \right) \simeq \frac{1}{n_0} \frac{\partial \mathbf{J}}{\partial t} - \frac{1}{n_0} \left(\frac{\mathbf{J}}{n_0} \cdot \nabla \right) \mathbf{J}. \quad (3.12)$$

When this expression is used in Eq. 2.24 and is substituted into Faraday's Law (Eq. 2.3), it can be written as

$$\frac{\partial \mathbf{B}'}{\partial t} = \nabla \times (\mathbf{v}_i \times \mathbf{B}) - \nabla \times \left(\frac{\mathbf{J} \times \mathbf{B}'}{nec} \right) + \frac{\eta c^2}{4\pi} \nabla^2 \mathbf{B} \quad (3.13)$$

where

$$\mathbf{B}' = (1 - d_e^2 \nabla^2) \mathbf{B} \quad (3.14)$$

is an ancillary variable. The code updates the quantity \mathbf{B}' using Eq. 3.13 and then the updated \mathbf{B} is found by solving the Helmholtz equation in Eq. 3.14 using Fourier Transforms with the updated \mathbf{B}' as the source term.

Time is stepped forward using the second order trapezoidal leapfrog method [Zalesak, 1979, Guzdar et al., 1993], a predictor-corrector scheme particularly well suited for handling convection. All spatial derivatives are fourth order finite difference. Fourth order diffusion is used in all of the equations to damp noise at the grid scale and small amplitude broadband noise is seeded initially to break the symmetry which allows flux bubbles to escape. The Hall effect and various parameters are on switches, so the code can be stopped and restarted with different parameters. Periodic boundary conditions are used in all directions, which requires simulating the double tearing mode configuration, whereby oppositely directed current sheets are

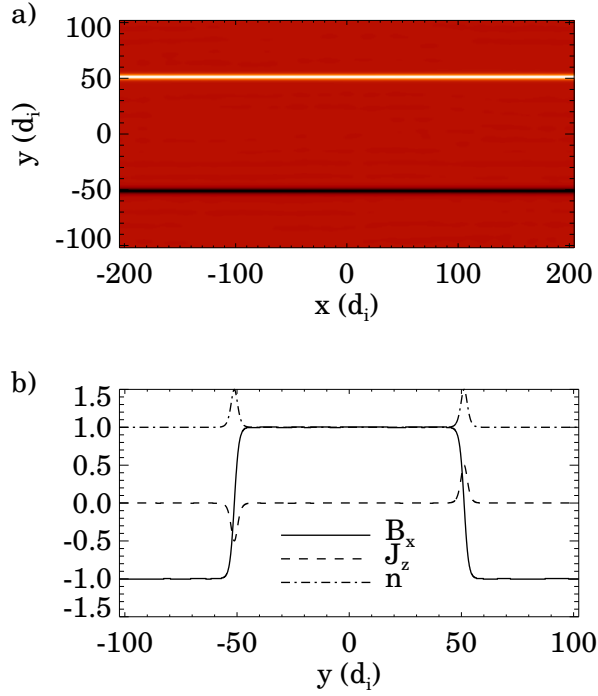


Figure 3.2: (a) Initial out of plane current density J_z for the double tearing mode configuration used in the simulations. (b) Cut in the y direction of B_x (solid line), J_z (dashed line), and n (dot-dashed line) in the initial configuration.

situated at $y = L_y/4$ and $-L_y/4$, where L_y is the size of the computational domain in the y direction, as pictured in Fig. 3.2a and the dashed line in Fig. 3.2b for the anti-parallel simulations. The resistivity is assumed constant and uniform.

All simulations discussed in this thesis are two-dimensional, with $\partial/\partial z = 0$. Unless otherwise noted, we use a Harris sheet initial equilibrium magnetic field configuration [Harris, 1962] with an optional uniform guide field B_{z0} ,

$$\mathbf{B}_0 = \hat{\mathbf{x}}B_0\{\tanh[(y + L_y/4)/w_0] - \tanh[(y - L_y/4)/w_0] - 1\} + \hat{\mathbf{z}}B_{z0}, \quad (3.15)$$

the x component of which is plotted as the solid line in Fig. 3.2b. The initial

pressure balance is enforced by a non-uniform density profile, $n(t = 0) = n_0 + (B_0^2/8\pi T_0)\{\text{sech}^2[(y + L_y/4)/w_0] + \text{sech}^2[(y - L_y/4)/w_0]\}$, plotted as the dot-dashed line in Fig. 3.2b. Here, n_0 is a constant corresponding to the density at the edge of the domain. An equation of state of $p = nT$ with a constant and uniform temperature $T = T_0$ is chosen for simplicity. The initial configuration for these simulations is unstable to the tearing mode, *i.e.*, we are in the large tearing parameter Δ' [Furth et al., 1963] limit (see the Appendix). Reconnection is initiated by a small coherent perturbation $\mathbf{B}_1 = (-B_1 L_y/2\pi)\hat{\mathbf{z}} \times \nabla[\sin(2\pi x/L_x) \sin^2(2\pi y/L_y)]$, where B_1 is a constant and L_x is the size of the computational domain in the x direction.

Lengths, magnetic field strengths, velocities, times, electric fields and resistivities are normalized to the ion skin depth d_{i0} based on n_0 , B_0 , the Alfvén speed c_{A0} based on B_0 and n_0 , the ion cyclotron time $\Omega_{ci0}^{-1} = (eB_0/m_i c)^{-1}$ based on B_0 , $E_0 = c_{A0}B_0/c$ and $\eta_0 = 4\pi c_{A0}d_{i0}/c^2$, respectively.

For the anti-parallel ($B_{z0} = 0$) reconnection simulations, the computational domain is of size $L_x \times L_y = 409.6d_{i0} \times 204.8d_{i0}$ with a cell size of $0.1d_{i0} \times 0.1d_{i0}$. The initial Harris sheet thickness is $w_0 = 2d_{i0}$. The temperature is $T_0 = B_0^2/4\pi n_0$ ($\beta = 1$ far from the sheet). The fourth order diffusion coefficient is $2 \times 10^{-5}d_{i0}^3 c_{A0}$. The size of the initial perturbation is $B_1 = 0.004B_0$. The electron mass is taken to be $m_e = m_i/25$ (*i.e.*, $d_e = 0.2d_i$). Although this value is unrealistic, the electron mass only controls dissipation at the electron scales, which as stated in Sec. 2.3, does not impact the rate of steady-state Hall reconnection [Shay and Drake, 1998, Hesse et al., 1999, Pritchett, 2001, Ricci et al., 2002].

For the simulations with a guide field, we use $B_{z0} = 5B_0$ with a computational

domain of size $L_x \times L_y = 204.8d_{i0} \times 102.4d_{i0}$ and a cell size of $0.05d_{i0} \times 0.05d_{i0}$. The initial Harris sheet thickness is $w_0 = 1d_{i0}$. The temperature is $T_0 = 5B_0^2/4\pi n_0$, making the total plasma $\beta = 5/26 \simeq 0.19$ far from the sheet and the in-plane $\beta_{rec} = 5$. These values were chosen to be in the kinetic Alfvén wave regime, as discussed in Sec. 2.4.3. The size of the initial perturbation is $B_1 = 0.002B_0$. The fourth order diffusion coefficient is $2 \times 10^{-5}d_{i0}^3c_{A0}$. The electron mass is again $m_e = m_i/25$.

3.4 Numerical Simulations of Bistability

In this section, we present the results of numerical simulations confirming the bistability of magnetic reconnection both without [Cassak et al., 2005] and with [Cassak et al., 2006a] a guide field.

3.4.1 Anti-parallel Reconnection

To demonstrate bistability of reconnection for resistivities satisfying $\eta'_{sf} < \eta' < \eta'_{fs}$, we perform two related sets of simulations. First, we show that a system undergoing Hall reconnection with a resistivity below η'_{fs} continues to do so for any value of resistivity below this value. Then, we show that a system undergoing Sweet-Parker reconnection with a resistivity above η'_{sf} will continue to do so for any value of resistivity above this value.

We can estimate η'_{sf} and η'_{fs} using Eqs. 3.10 and 3.11 for the computational domain described in the previous section. Since the Sweet-Parker current layer extends along half of the box in the x direction, the half-length L_{SP} of the Sweet-

Parker layer is $L_x/4 \simeq 100d_i$. Benchmark resistive-MHD simulations put the value closer to $L_{SP} \simeq 90d_i$. Thus,

$$\eta'_{sf} \sim \frac{d_i}{L_{SP}} \simeq 0.011. \quad (3.16)$$

From benchmark simulations of Hall reconnection, the magnetic field strength upstream of the electron and ion dissipation regions are $B_{up,e} \simeq 0.35B_0$ and $B_{up} \simeq 0.93B_0$, respectively, so

$$\eta'_{fs} \sim 0.1 \frac{B_{up,e}}{B_{up}} \simeq 0.032. \quad (3.17)$$

We emphasize that these scales differ by only a factor of 3 because of computational constraints; a larger domain would lead to a more realistic separation in scales because $\eta'_{fs}/\eta'_{sf} \propto L_{SP} \propto L_x$, but would be computationally prohibitive.

We start with a benchmark collisionless ($\eta = 0$) Hall-MHD simulation that is run from $t = 0$ until the rate of reconnection is steady. The reconnection rate E is shown as a function of island width w as the thick solid line in Fig. 3.3. Since the island width increases monotonically in time, w is a proxy for the time t . The reconnection rate is calculated from Eq. 2.8 as the time rate of change of magnetic flux between the X-line and O-line, the center of the magnetic island. The rate of reconnection jumps to $E \simeq 0.06E_0$ by the time the island width is $10d_i$, after which it remains steady. When $w \simeq 35d_i$, we enable a resistivity of $\eta = 0.015\eta_0$ (which lies between the predicted values of η_{sf} and η_{fs}) and continue the simulation until most of the available magnetic flux has been reconnected. For comparison, the thick dashed line shows the reconnection rate when we maintain $\eta = 0$. Clearly, the reconnection rate remains nearly unchanged after the inclusion of the resistivity.

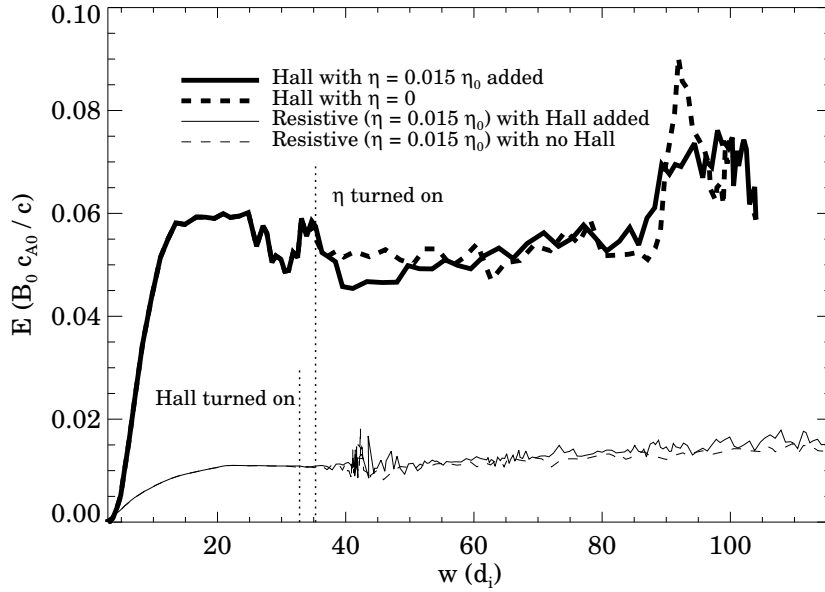


Figure 3.3: Reconnection rate E as a function of island width w for the two sets of anti-parallel reconnection simulations described in the text. The vertical dotted lines show when the added effects were enabled. Note that the final parameters of the two solid line simulations are identical.

For the second set of simulations, we perform a benchmark resistive-MHD simulation (with no Hall or electron inertia terms) with a resistivity of $\eta = 0.015\eta_0$. The reconnection rate is plotted in Fig. 3.3 as the thin solid line. The reconnection rate reaches a steady value of $E \simeq 0.01E_0$, a factor of six slower than the Hall case². Then, we enable the Hall and electron inertia terms when $w \simeq 33d_i$ and continue to advance the full equations. Even with the Hall and electron inertia terms enabled, the reconnection rate remains steady at $E \simeq 0.01E_0$. For comparison, the thin dashed line in Fig. 3.3 shows the reconnection rate for a system in which the Hall

²The separation of scales of the reconnection rate being only six is again an artifact of the simulations; for realistic parameters for a solar flare, the separation of scales is 10^6 .

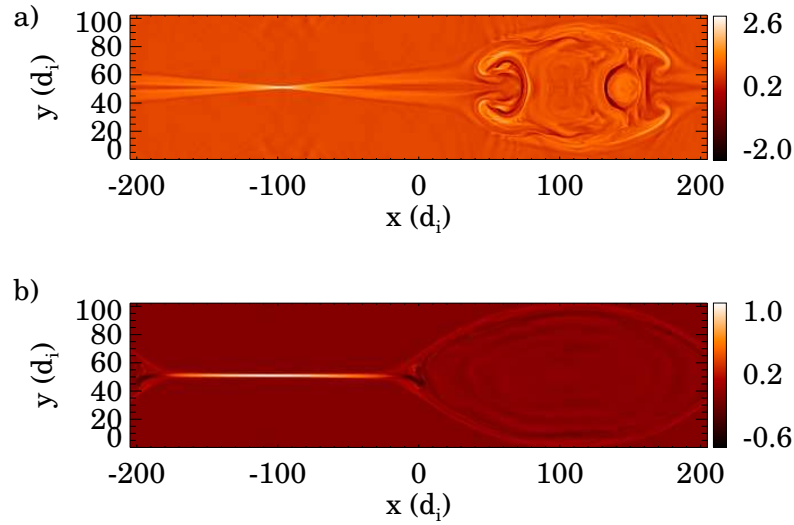


Figure 3.4: Out of plane current density J_z for late times from the two solid lines of Fig. 3.3. (a) Hall reconnection (the thick solid line). (b) Sweet-Parker reconnection (the thin solid line).

term is not enabled. The Hall and electron inertia terms clearly do not impact the rate of Sweet-Parker reconnection for these parameters.

The out of plane current density J_z is shown at late time in Fig. 3.4a for the system plotted as the thick solid curve in Fig. 3.3. The current sheet is short and opens wide into the Petschek configuration, as is expected in Hall reconnection [Shay et al., 1999, Horiuchi and Sato, 1997, Pritchett, 2001, Kuznetsova et al., 2001, Hesse et al., 2001, Porcelli et al., 2002]. Fig. 3.4b shows J_z for the system plotted as the thin solid curve in Fig. 3.3. The current sheet is long and thin as is expected in Sweet-Parker reconnection [Biskamp, 1986, Uzdensky and Kulsrud, 2000, Jemella et al., 2004]. Since the same equations govern the two sets of data and the value of the resistivity is the same, we conclude that the system is bistable at this

value of the resistivity.

Next, we test the predictions of η'_{sf} and η'_{fs} by changing the resistivities of the benchmark Hall and Sweet-Parker reconnection solutions of Fig. 3.3. For the case of Hall reconnection, we change η from 0.0 to 0.010, 0.013, 0.015, 0.0175, 0.020, 0.0225, 0.025 and $0.030\eta_0$ when $w \simeq 35d_i$. For the case of Sweet-Parker reconnection, we change η from $0.015\eta_0$ to 0.003, 0.007, 0.009, 0.011, 0.013, 0.0175, 0.020, 0.0225, 0.025 and $0.030\eta_0$ when $w \simeq 50d_i$ (a short time after the Hall and electron inertia terms are re-enabled). The asymptotic reconnection rate is computed as the time averaged reconnection rate once transients have died away.

The results are plotted in Fig. 3.5a, with the states starting from Hall reconnection plotted as open circles and the states starting from Sweet-Parker plotted as closed circles. The dashed line shows the prediction of the Sweet-Parker model based on $L_{SP} \simeq 90d_i$ and $B_{up} \simeq 0.93B_0$. The closed circles reveal that the disappearance of the Sweet-Parker solution occurs abruptly, with η_{sf} between 0.011 and $0.013\eta_0$. The open circles reveal the abrupt disappearance of the Hall solution, with η_{fs} between 0.020 and $0.0225\eta_0$. The error bars are due to random fluctuations in the reconnection rate.

Thus, the numerical simulations confirm that magnetic reconnection is bistable over a range of resistivities and that the edges of the bistable region are abrupt. Taking care to normalize to $B_{up} \simeq 0.93B_0$ and $d_i \simeq d_{i0}$, the simulations give η'_{sf} between 0.012 and 0.014 and η'_{fs} between 0.22 and 0.24, comparable to the scaling law predictions of $\eta'_{sf} \simeq 0.011$ and $\eta'_{fs} \simeq 0.032$ from Eqs. 3.16 and 3.17. The asymptotic steady-state current sheet thickness δ , measured as the half-width at

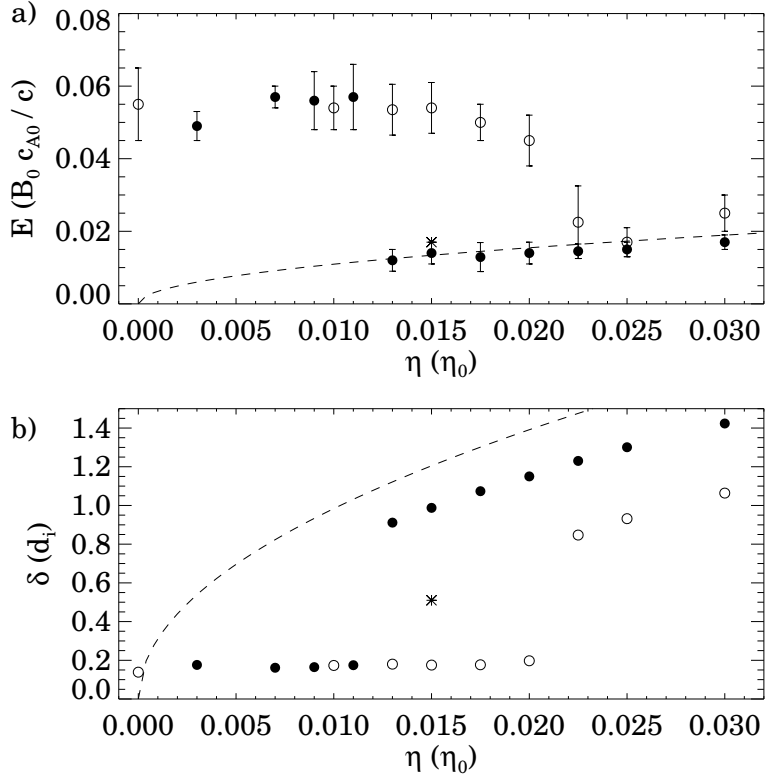


Figure 3.5: (a) Steady state reconnection rate E as a function of resistivity η for runs analogous to those in Fig. 3.3. (b) Current sheet thickness δ as a function of η for the simulations in (a).

half-maximum of $J_z(y)$ at the X-line, is plotted in Fig. 3.5b for each of the runs, with the Sweet-Parker prediction as the dashed line. (Note, the measured δ is found using the half-width at half-maximum of the current sheet, which underestimates the value.) As predicted by Eq. 3.2, the current sheet thickness δ is of order d_i when the Sweet-Parker solution ceases to exist, shown by the closed circles of Fig. 3.5b.

We emphasize that the results presented in Fig. 3.5, though generated by a specific numerical procedure, are not sensitive to the details of this procedure. To demonstrate this, we show that the key feature of Fig. 3.5, the boundary where the

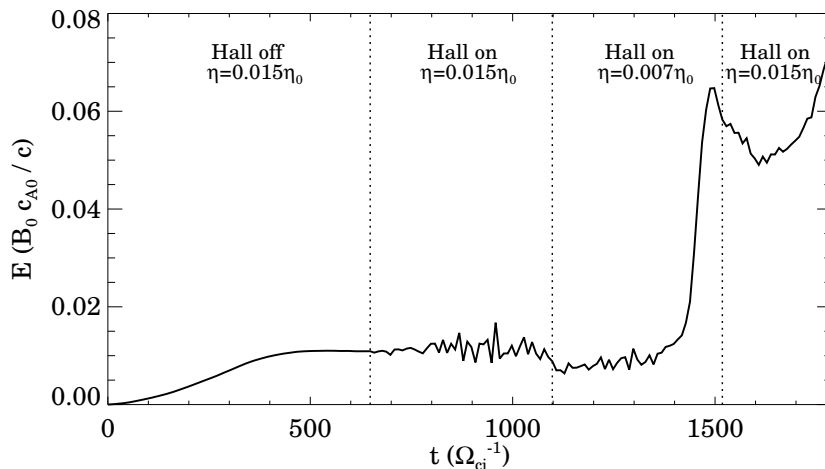


Figure 3.6: Reconnection rate E as a function of time t for the simulation which starts with $\eta = 0.015\eta_0$, is reduced to $0.007\eta_0$, then is increased back to $0.015\eta_0$.

slow reconnection solution disappears, can be reproduced through a hysteresis-like procedure: in the simulation corresponding to the thin solid line in Fig. 3.3, we first lower the resistivity from $\eta = 0.015\eta_0$ to $\eta = 0.007\eta_0$ at $t = 1098\Omega_{ci}^{-1}$ (when the island width is about $w \sim 50d_i$). As shown in Fig. 3.6, a transition from Sweet-Parker to Hall reconnection occurs. We then raise the resistivity back to $\eta = 0.015\eta_0$ (the original value) at $t = 1518\Omega_{ci}^{-1}$ (when the island width is about $w \sim 68d_i$). As shown in Fig. 3.6, fast reconnection continues, confirming that the system can be in either solution for the same set of parameters.

These simulations confirm that bistability (and hysteresis) occurs during anti-parallel reconnection and the abrupt disappearance of the Sweet-Parker solution occurs when $\delta \sim d_i$. Recent simulations [Knoll and Chacon, 2006] of the island coalescence instability in low- η resistive Hall-MHD have also found an abrupt tran-

sition from resistive-dominated to Hall-dominated reconnection when the current sheet thickness falls below the ion skin depth, in agreement with the present results.

3.4.2 Component Reconnection

The procedure described in the previous section is now used for component reconnection. We again estimate η'_{sf} and η'_{fs} using Eqs. 3.10 and 3.11 for the computational domain described in the previous section. The half-length L_{SP} of the Sweet-Parker layer is expected to be $L_x/4 \simeq 50d_i$. Benchmark resistive-MHD simulations put the value closer to $L_{SP} \simeq 38d_i$. Using $\beta \simeq 0.19$,

$$\eta'_{sf} \sim \frac{\rho_s^2}{d_i L_{SP}} \sim \frac{\beta d_i}{L_{SP}} \simeq 0.005. \quad (3.18)$$

From benchmark simulations of Hall reconnection in this domain, we find the magnetic field strength upstream of the electron and ion dissipation regions to be $B_{up,e} \simeq 0.35B_0$ and $B_{up} \simeq 0.8B_0$, respectively, so

$$\eta'_{fs} \sim 0.1\beta^{1/2} \frac{B_{up,e}}{B_{up}} \simeq 0.019. \quad (3.19)$$

As before, these scales differ by only a factor of 4 due to computational constraints.

A plot demonstrating bistability analogous to Fig. 3.3 is shown for component reconnection in Fig. 3.7. A benchmark collisionless ($\eta = 0$) simulation is evolved until a steady-state of Hall reconnection is reached, with a reconnection rate of $E \simeq 0.065E_0$, plotted as the thick solid line in Fig. 3.7 as a function of the island width w , again a proxy for time. Then, a resistivity of $\eta = 0.01\eta_0$ (which lies between the predicted values of η_{sf} and η_{fs}) is enabled when the island width $w \simeq 17d_i$ and

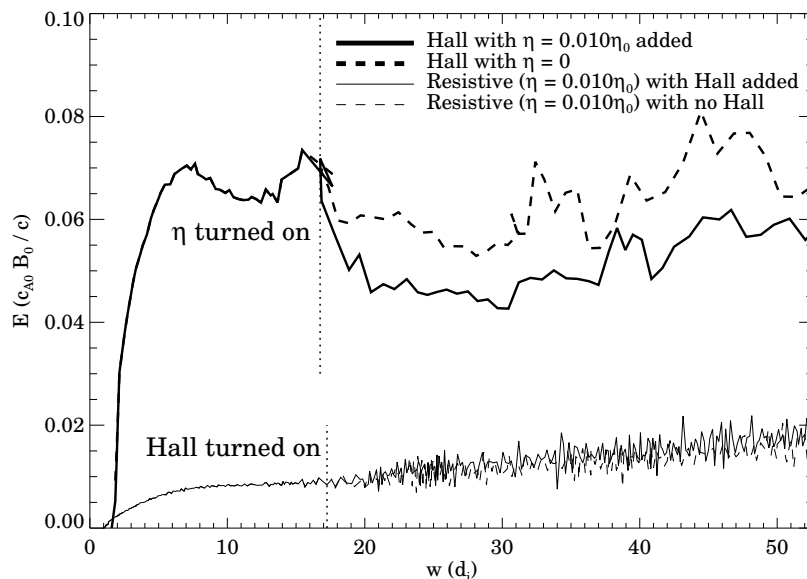


Figure 3.7: Reconnection rate E as a function of island width w for the two sets of component reconnection simulations described in the text, analogous to Fig. 3.3 for the anti-parallel case.

the simulation is continued. The thick dashed line shows the reconnection rate when $\eta = 0$ is maintained. A slight decrease in the reconnection rate is observed, but clearly it remains in the Hall solution.

Similarly, we perform a benchmark resistive-MHD simulation with $\eta = 0.01\eta_0$ (the same resistivity). As shown in the thin solid line of Fig. 3.7, the reconnection rate reaches a steady value at about $E \simeq 0.01E_0$. Then, we enable the Hall and electron inertia terms when $w \simeq 17d_i$ and continue to advance the full equations. The reconnection rate remains stationary with $E \simeq 0.01E_0$. For comparison, a simulation in which the Hall term is not enabled is shown as the thin dashed line. Clearly, the Hall and the electron inertia terms do not impact the rate of Sweet-Parker reconnection for these parameters. Since the thick and thin solid lines are

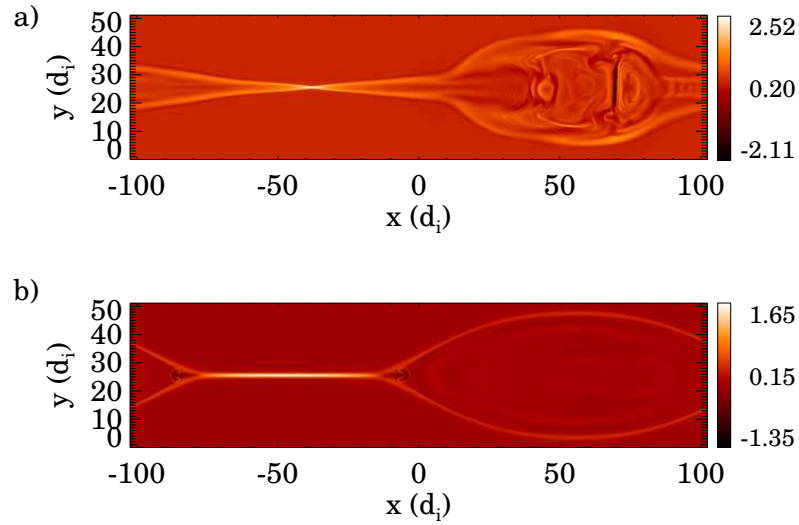


Figure 3.8: Out of plane current density J_z for late times from the two solid lines of Fig. 3.7. (a) Hall reconnection (the thick solid line). (b) Sweet-Parker reconnection (the thin solid line).

governed by the same equations and have the same resistivity, bistability for component reconnection has been demonstrated for this value of the resistivity. The out of plane current density J_z is shown at late time in Fig. 3.8 for the runs corresponding to the two solid curves in Fig. 3.7, with the run beginning in Hall reconnection in Fig. 3.8a and the run beginning in Sweet-Parker in Fig. 3.8b. As in the anti-parallel case, these configurations show the typical Hall open outflow and Sweet-Parker long dissipation region signatures.

The predictions of η'_{sf} and η'_{fs} are tested by varying the resistivities of the benchmark Hall and Sweet-Parker reconnection simulations of Fig. 3.7. For the case of Hall reconnection, we change η from 0.0 to 0.005, 0.007, 0.010, 0.0125, 0.015, 0.0175 and $0.020\eta_0$ when $w \simeq 17d_i$. For the case of Sweet-Parker reconnection, we

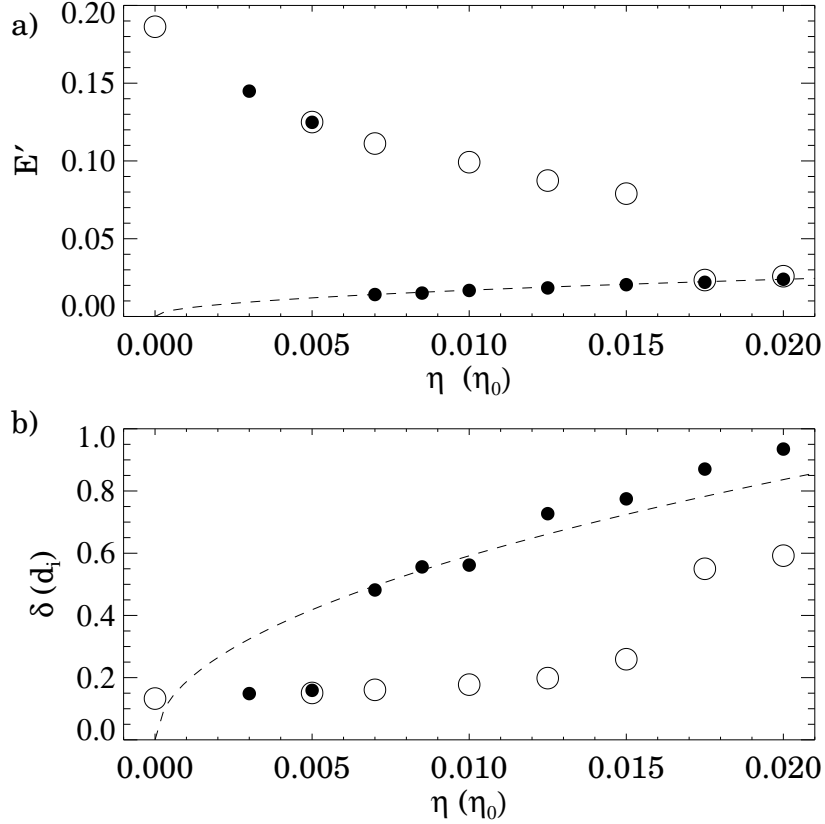


Figure 3.9: (a) Steady state normalized reconnection rate E' as a function of resistivity η for runs analogous to those in Fig. 3.7. (b) Current sheet thickness δ as a function of η for the simulations in (a).

change η from $0.010\eta_0$ to 0.003 , 0.005 , 0.007 , 0.0085 , 0.010 , 0.0125 , 0.015 , 0.0175 , and $0.020\eta_0$ when $w \sim 20.5d_i$ a short time after the Hall and electron inertia terms have been re-enabled.

The normalized asymptotic reconnection rate E' , computed as the time averaged reconnection rate once transients have died away and normalized to $B_{up}c_{Aup}/c$, is plotted in Fig. 3.9a. The simulations starting in Hall reconnection are the open circles, while the closed circles start in Sweet-Parker. The numerical simulations

confirm that magnetic reconnection is bistable over a range of resistivity from 0.007 to $0.015\eta_0$. The dashed line shows the prediction of the Sweet-Parker model based on $L_{SP} \simeq 38d_i$ and $B_{up} \simeq 0.8B_0$, showing excellent agreement with the results. (The apparent dependence on η of E' during Hall reconnection seen in Fig. 3.9a is unexpected and does not occur for anti-parallel reconnection. It is probably a numerical effect due to the fact that the ion and electron dissipation regions are not well separated in our simulations, as ρ_s is only twice as big as d_e .)

As in the anti-parallel case, the edge of the bistable region is observed to be abrupt with critical values of η_{sf} between 0.005 and $0.007\eta_0$ and η_{fs} between 0.015 and $0.0175\eta_0$. Normalizing using $B_{up} \simeq 0.8B_0$ and $d_i \simeq d_{i0}$ gives simulation values of η'_{sf} between 0.006 and 0.009 and η'_{fs} between 0.019 and 0.022, in good agreement with the predicted values of $\eta'_{sf} \sim 0.005$ and $\eta'_{fs} \sim 0.019$ from Eqs. 3.18 and 3.19.

The asymptotic steady-state current sheet thickness δ , measured as the half-width at half-maximum of $J_z(y)$ at the X-line, is plotted in Fig. 3.9b for each of the runs, with the Sweet-Parker prediction plotted as the dashed line. Note, with $\beta \simeq 0.19$, the ion Larmor radius is $\rho_s = \sqrt{\beta}d_i \sim 0.44d_i$. The transition from Sweet-Parker to Hall reconnection (shown in the closed circles in the figure) occurs when the thickness of the current sheet is approximately ρ_s , as predicted by Eq. 3.2. These simulations confirm that component reconnection is bistable, and that the Sweet-Parker solution disappears abruptly when $\delta \sim \rho_s$.

3.5 Experimental Results from Magnetic Reconnection Experiment (MRX)

A succession of laboratory experiments at the Magnetic Reconnection Experiment (MRX) have been able to study anti-parallel reconnection in a weakly collisional plasma. They found [Trintchouk et al., 2003] that when the thickness of the Sweet-Parker current sheet is larger than the ion skin depth, the Sweet-Parker model with classical Spitzer resistivity is valid, but it breaks down when the thickness falls below the ion skin depth, in agreement with the present simulations. When $\delta_{SP} < d_i$, the reconnection rate is greatly enhanced and the out of plane electric field due to the Hall effect is nearly equal to the reconnection electric field [Yamada et al., 2006]. In addition, during the faster reconnection, a quadrupolar out of plane magnetic field (a signature of Hall reconnection; see Sec. 2.3) was measured. Its strength is independent of η when reconnection is fast and greatly reduced when reconnection is slow [Ren et al., 2005, Yamada et al., 2006]. These results compare favorably with the present simulations³.

3.6 Summary

In this chapter, we have shown using theoretical considerations and numerical simulations that the Sweet-Parker solution only exists when the thickness of the collisional dissipation region is larger than the appropriate kinetic length scale (d_i for anti-parallel reconnection, ρ_s for component), while the Hall solution only exists

³At this time, it is not experimentally feasible to access the other branch of the bistable state.

when the resistivity is not large enough to destroy the electron dissipation region. As a result, magnetic reconnection is bistable for a wide range of the dimensionless parameter η' . In the next chapter, we attempt to gain a better understanding of this bistability, showing that it can be concisely described in the language of bifurcation theory.

Chapter 4

Nonlinear Dynamics of Magnetic Reconnection

The emerging picture of the dynamics of magnetic reconnection, with bistability and hysteresis as described in Chapter 3, is very rich. Bistability is well known in bifurcation theory of ordinary differential equations (see, for example, Ref. [Strogatz, 1994]). A bifurcation is an abrupt change in the stability of a steady-state solution which occurs as a control parameter is varied. Of particular interest to this study is the so-called “saddle-node bifurcation”, in which steady-state solutions are brought into or out of existence as a control parameter is varied, as observed when the normalized resistivity η' is varied for the Sweet-Parker and Hall reconnection solutions [Cassak et al., 2006c].

In Sec. 4.1, we describe the simplest bifurcation model which reproduces the results of Chapter 3. This model predicts the existence of a heretofore unknown unstable steady-state magnetic reconnection configuration. Additional predictions of the bifurcation model are discussed in Sec. 4.2. In Sec. 4.3, we verify the predictions of the model using numerical simulations, including the demonstration of the existence of the unstable solution. In Sec. 4.4, we probe the linear properties of the unstable solution numerically, finding the most unstable eigenmode and its growth rate.

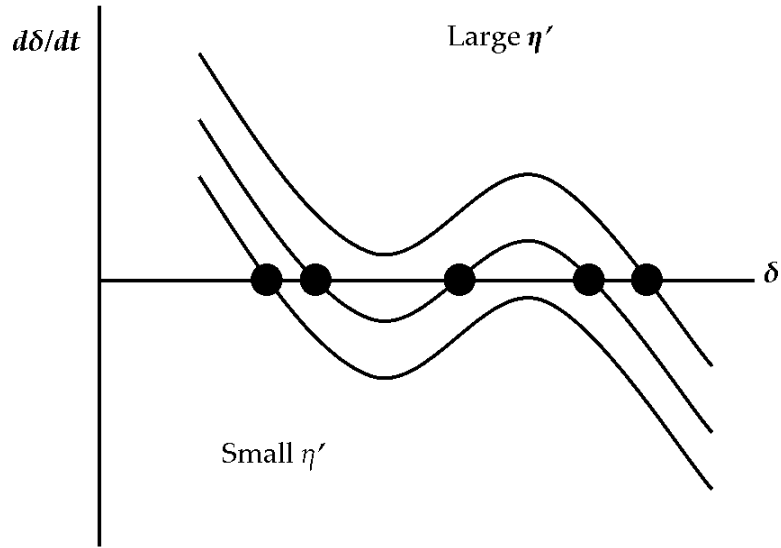


Figure 4.1: Schematic phase portrait of the dissipation region thickness δ , where the curve moves downward as η' decreases. The heavy dots denote steady-state solutions.

4.1 Bifurcation Model of Magnetic Reconnection Dynamics

The simplest bifurcation model reproducing the dynamics of Fig. 3.1 is plotted schematically in Fig. 4.1 as a phase portrait for the current sheet thickness δ (*i.e.*, $d\delta/dt$ versus δ) for various η' . Steady-state equilibria (fixed points), marked by heavy dots, occur where the lines cross the horizontal axis because if a system begins at that δ , it will stay there forever because $d\delta/dt = 0$. The uppermost curve is for large η' , for which the only steady-state solution is at a relatively large δ , corresponding to Sweet-Parker reconnection. This fixed point is stable, as evidenced by the slope

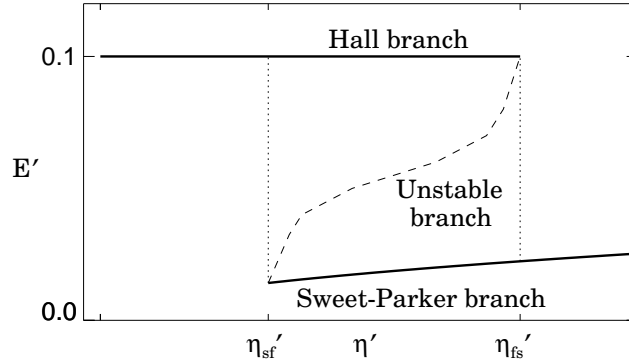


Figure 4.2: Schematic bifurcation diagram for the phase portrait in Fig. 4.1. The dashed line shows the unstable solution. This figure reproduces the salient features of Fig. 3.1.

of the line through the fixed point being negative¹. As η' is lowered continuously, the curve moves down and two new fixed points (one stable, one unstable) are born when the curve crosses the δ axis. This is a saddle-node bifurcation, also known as a “blue sky bifurcation” because the fixed points come into existence from “out of the blue sky” [Strogatz, 1994]. The stable fixed point at a relatively small δ corresponds to the Hall solution. For a range of η' , there are two distinct stable steady-state solutions as shown in the middle curve in Fig. 4.1, *i.e.*, there is bistability. As η' continues to decrease, the curve continues to move lower, and the unstable and Sweet-Parker fixed points approach each other, coalesce, and disappear in a second saddle-node bifurcation. For small η' , the only steady-state solution is the Hall solution, as is shown in the lowest curve in Fig. 4.1.

¹Taylor expanding the function representing the curve near the fixed point gives $d\delta/dt = \gamma\delta$, where γ is the slope of the line. A positive slope implies exponential growth (instability); a negative slope implies exponential decay (stability). The magnitude of γ is the growth or decay rate.

The bifurcation diagram showing the fixed points as a function of the control parameter η' for the system described by Fig. 4.1 is shown in Fig. 4.2. It bears a strong resemblance to Fig. 3.1. In addition to the two stable solutions, it displays the unstable solution shown by the dashed line. This heretofore unidentified steady-state solution must exist in the region of bistability.

4.2 Additional Predictions of the Bifurcation Model

4.2.1 Time Evolution of the Current Sheet Thickness

This simple model makes verifiable predictions about the time evolution of the current sheet thickness δ . Just after the bifurcation which takes the Sweet-Parker solution out of existence, the phase portrait looks like the curve in Fig. 4.3a. Although the Sweet-Parker equilibrium is no longer there, it continues to influence the dynamics. For a system beginning at a large current sheet thickness (denoted by a 1 in the diagram), $d\delta/dt$ is relatively large and negative, meaning the thickness will initially decrease quickly, as depicted schematically in Fig. 4.3b. As δ approaches the point marked 2, where the Sweet-Parker solution had been, $d\delta/dt$ becomes very small and the system spends a longer time there. The point where the fixed point had been is known as a “ghost” or “shadow”, and the tendency for the system to stay near the ghost for a relatively long time is called “bottlenecking” [Strogatz, 1994]. As the system moves away from the ghost, $d\delta/dt$ becomes larger as the system moves through the points marked 3 and 4 on the diagram. If saddle-node bifurcations are present, we would expect δ to evolve in time according to Fig. 4.3b.

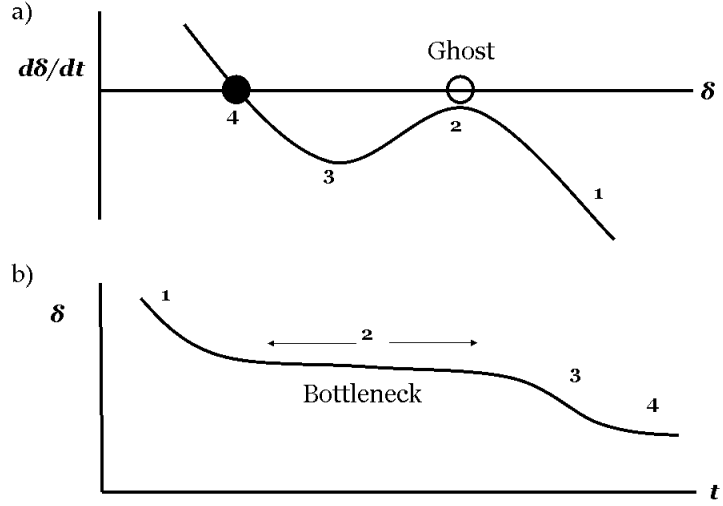


Figure 4.3: (a) Schematic phase portrait for δ just after the saddle-node bifurcation that takes the Sweet-Parker solution out of existence. (b) Schematic plot of the time evolution from points 1 to 4 for the phase portrait in (a). Both plots adapted from Ref. [Strogatz, 1994].

Many previous numerical studies of magnetic reconnection onset found that the system spends time in a Sweet-Parker like (Y-type) configuration before finally reaching the Hall (X-type) configuration [Aydemir, 1992, Horiuchi and Sato, 1994, Ma and Bhattacharjee, 1996]. It would be interesting to revisit such studies in light of the present model.

4.2.2 The Transition Time From Sweet-Parker to Hall Reconnection

The time τ spent in the bottleneck near the Sweet-Parker ghost can be shown in great generality to scale as $\tau \propto (\eta'_{sf} - \eta')^{-1/2}$ [Strogatz, 1994] for η' sufficiently close to η'_{sf} , where η'_{sf} is the value of η' at the saddle-node bifurcation. Just after the saddle-node bifurcation, as is sketched in Fig. 4.3a, the phase portrait near the

ghost is locally parabolic,

$$\frac{d\delta}{dt} = -(r + \kappa\delta^2), \quad (4.1)$$

where $r \propto (\eta'_{sf} - \eta')$ is a measure of the distance between the curve and the horizontal axis and κ is a constant. If the curve is sufficiently close to the horizontal axis, most of the transition time is spent getting through the bottleneck, which can be approximated as

$$\tau = \int dt \simeq \int_{\infty}^0 \frac{d\delta}{d\delta/dt} = \int_0^{\infty} \frac{d\delta}{r + \kappa\delta^2} \propto \frac{1}{\sqrt{r}}. \quad (4.2)$$

Since $r \propto (\eta'_{sf} - \eta')$, we can write this as

$$\tau = \tau_0 \left(\frac{\eta'_{sf} - \eta'}{\eta'_{sf}} \right)^{-1/2} \quad (4.3)$$

where τ_0 is a characteristic time scale required for a transition. Thus, the transition time τ for different η' should obey this scaling law if saddle-node bifurcations occur.

4.3 Simulation Results

In this section, we show that results of numerical simulations are consistent with the predictions discussed in the previous section. First, we show the thickness of the current sheet δ evolves qualitatively as expected after a saddle-node bifurcation. Then, we show the scaling of the transition time τ from Sweet-Parker to Hall reconnection is consistent with Eq. 4.3. Lastly, we numerically demonstrate the existence of an unstable steady-state reconnection configuration using a novel computational technique introduced in Ref. [Skufca et al., 2005].

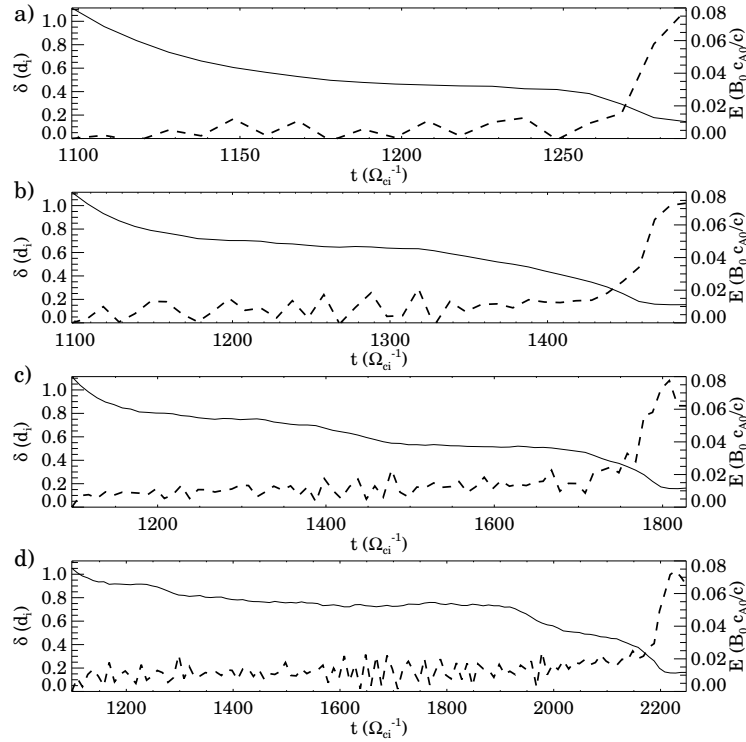


Figure 4.4: Current sheet thickness δ (solid line, left scale) and reconnection rate E (dashed line, right scale) versus time t for simulations in which a transition from Sweet-Parker to Hall reconnection is made when η is lowered from $0.015\eta_0$ to (a) 0.003 , (b) 0.007 , (c) 0.009 , and (d) $0.011\eta_0$. The time evolution of δ is qualitatively similar to that drawn in Fig. 4.3b.

4.3.1 Time Evolution of the Current Sheet Thickness

The temporal evolution of the current sheet thickness δ can be extracted from the numerical simulations used to construct Fig. 3.5 and described in Sec. 3.4.1. Figs. 4.4a - d show δ , measured as the half-width at half-maximum across the X-line of the out of plane current density J_z , as a function of time during the transition from Sweet-Parker to Hall reconnection, corresponding to the closed circles with $\eta = 0.003, 0.007, 0.009$, and $0.011\eta_0$ in Fig. 3.5. The time evolution of δ is strikingly

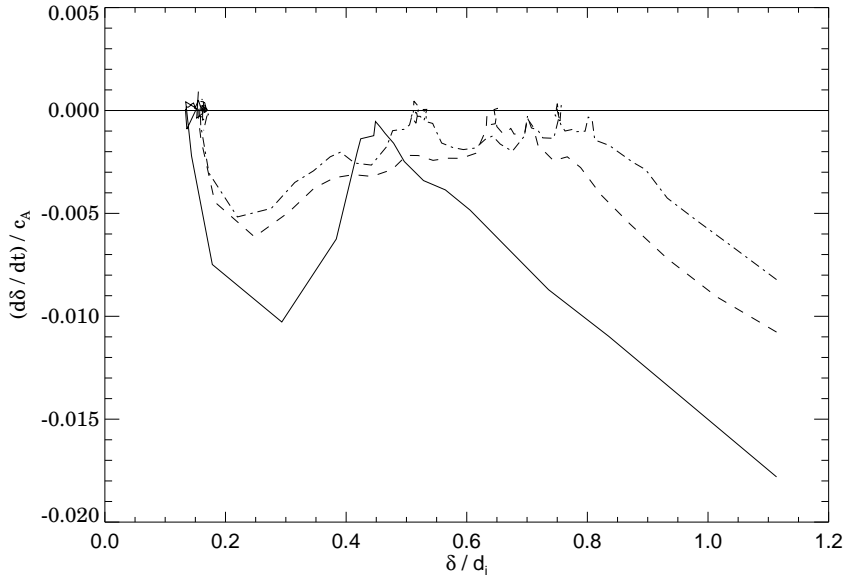


Figure 4.5: Phase portrait for the current sheet thickness δ obtained during the transition from Sweet-Parker to Hall reconnection from the simulations shown in Fig. 4.4a - c. From bottom to top, $\eta = 0.003, 0.007$ and $0.009\eta_0$. Note the similarity to Fig. 4.1.

similar to that pictured in Fig. 4.3b, with the bottleneck behavior one would expect.

The phase portrait of δ can be extracted by plotting the time rate of change of δ versus δ , shown in Fig. 4.5 for three simulations making a transition from Sweet-Parker to Hall reconnection ($\eta = 0.003, 0.007$ and $0.009\eta_0$). They are qualitatively similar to the lowest curve in Fig. 4.1, suggesting that the results are consistent with the presence of saddle-node bifurcations.

The reconnection rate E (calculated as the time rate of change of the flux between the X-line and the O-line) is plotted as a function of time as the dashed lines in Fig. 4.4 with the scale on the right. The system undergoes a prolonged slow increase of E with time before an faster than exponential explosive growth,

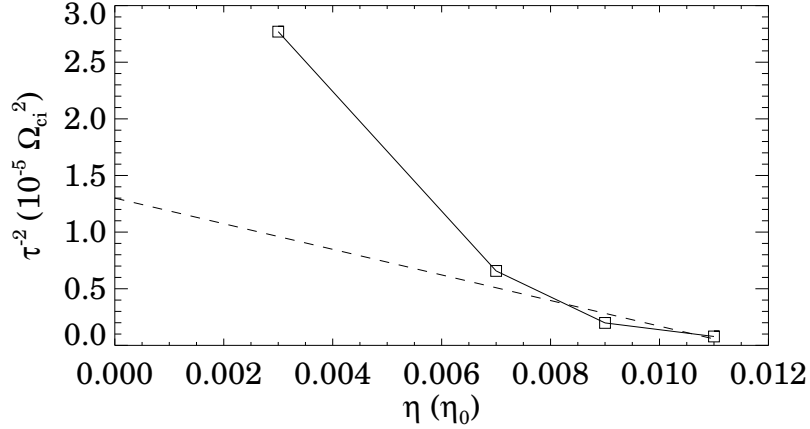


Figure 4.6: A plot of $1/\tau^2$, where τ is the duration of the transitions in Fig. 4.4, as a function of η . Eq. 4.3 predicts a straight line when η is near η_{sf} , drawn as a dashed line.

similar to that observed in previous simulations in which a transition from a long current sheet (Y-type reconnection) to a short current sheet (X-type reconnection) was studied [Aydemir, 1992, Horiuchi and Sato, 1994, Ma and Bhattacharjee, 1996, Shay et al., 2004].

4.3.2 The Transition Time from Sweet-Parker to Hall Reconnection

The time τ elapsed during the transition between Sweet-Parker and Hall reconnection can be read directly off of the plots in Fig. 4.4; $\tau \simeq 190, 420, 710$, and $1130\Omega_{ci}^{-1}$ for $\eta = 0.003, 0.007, 0.009$, and $0.011\eta_0$, respectively. Eq. 4.3 suggests that $1/\tau^2$ should be linear in η' for η' close enough to η'_{sf} , and that the values for η'_{sf} and $1/\tau_0^2$ can be read off from the x - and y -intercepts, respectively. Fig. 4.6 shows $1/\tau^2$ versus η for the four simulations which made a transition from Sweet-Parker

to Hall reconnection in Fig. 4.4. The assumption of proximity to η'_{sf} is dubious for the $\eta = 0.003\eta_0$ simulation. The other three points approximately lie on a straight line, denoted by the dashed line in Fig. 4.6. The x -intercept gives a critical value of $\eta_{sf} \simeq 0.0115$, consistent with the theoretical value in Eq. 3.16. The y -intercept of the best fit curve gives a transition time scale of $\tau_0 = (270 \pm 40)\Omega_{ci}^{-1}$. This compares favorably with the growth time found another way, as we will discuss in Sec. 4.4. The consistency of the scaling of the time required for the transition with Eq. 4.3 lends credence to the interpretation of the disappearance of the Sweet-Parker solution as a saddle-node bifurcation.

4.3.3 The Unstable Steady-State Reconnection Solution

The bifurcation model given in Sec. 4.1 predicts the existence of an unstable steady-state magnetic reconnection solution between the stable, steady-state Sweet-Parker and Hall solutions in the region of bistability. In addition to lending further credence to the model, identifying the unstable configuration can provide further insight into the physical mechanism driving the explosive onset, as we discuss in the next section. However, finding the equilibrium numerically is difficult because systems typically evolve away from unstable equilibria.

A novel iterative technique to numerically approach an unstable equilibrium was recently developed for the onset of chaos in a nine dimensional system of ordinary differential equations [Skufca et al., 2005]. The idea is to take weighted aver-

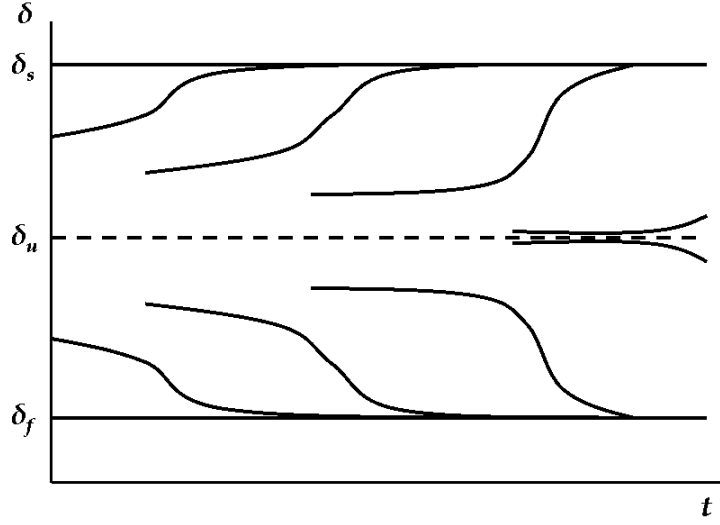


Figure 4.7: Schematic diagram of the expected temporal behavior of the current sheet thickness δ for the iteration scheme to find the unstable equilibrium described in Sec. 4.3.3.

ages of the two stable configurations ψ_f and ψ_s ,

$$\psi_\epsilon = \epsilon\psi_f + (1 - \epsilon)\psi_s, \quad (4.4)$$

where ϵ is a constant weighting factor between 0 and 1, and ψ corresponds to all relevant dynamical variables, which for Hall-MHD are the plasma density n , the ion velocity \mathbf{v}_i and the magnetic field \mathbf{B} . The subscripts f and s refer to fast (Hall) and slow (Sweet-Parker), respectively. By choosing various values of ϵ , one can bracket the unstable configuration, *i.e.*, for one value of ϵ the system returns to one stable state while for another it returns to the other, implying that the unstable configuration is between them. The process is repeated by taking weighted averages of the weighted averaged states, eventually converging to the unstable equilibrium.

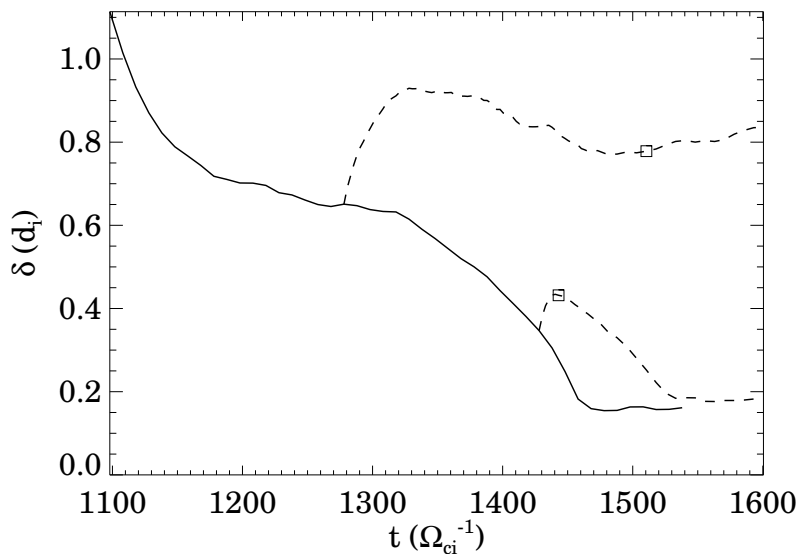


Figure 4.8: Current sheet thickness δ as a function of time t for the procedure to create initial states ψ_f and ψ_s for the iteration technique to find the unstable equilibrium described in the text. Convergence is expedited by using the states denoted by the boxes as initial conditions.

A schematic plot of what the time evolution of a variable would like like using this procedure is given in Fig. 4.7.

To expedite convergence, we construct a set of ψ_f and ψ_s in the process of making a transition to either the Hall or Sweet-Parker solution rather than using the Sweet-Parker and Hall solutions themselves. Since the unstable solution is unique for a given resistivity, the different starting condition is of no consequence. We begin with a system undergoing Sweet-Parker reconnection with $\eta = 0.015\eta_0$ up until $t = 1098\Omega_{ci}^{-1}$. Then, the resistivity is lowered to $\eta = 0.007\eta_0$ and the system makes a transition to Hall reconnection, as shown in the solid line in Fig. 4.8. During the transition (at $t = 1278\Omega_{ci}^{-1}$), we return η to $0.015\eta_0$. The upper dashed

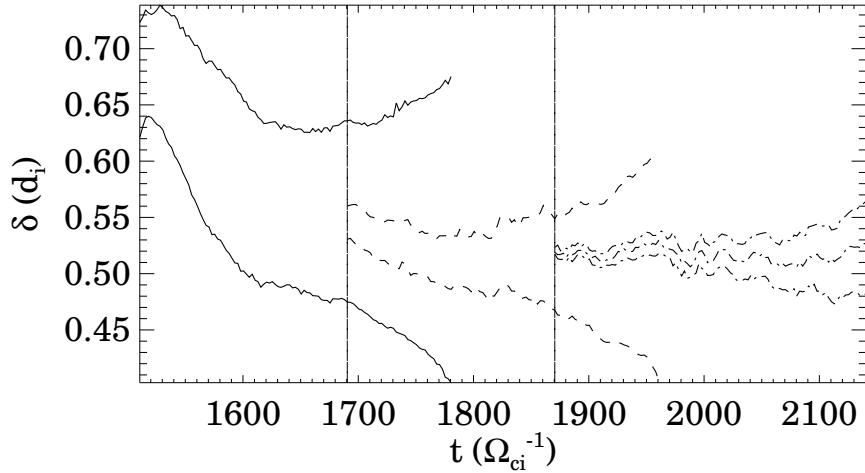


Figure 4.9: Results of the iteration procedure for finding the unstable equilibrium described in the text. The first iteration is shown as the solid lines. The second iteration is shown as the dashed lines, initialized by taking weighted averages of the first iteration states at the first vertical line. The third iteration is shown as the dot-dashed lines, initialized by the states at the second vertical line. The middle dot-dashed state is very close to the unstable configuration.

line indicates that the system reverts back to Sweet-Parker reconnection. However, when we return η to $0.015\eta_0$ later during the transition (at $t = 1428\Omega_{ci}^{-1}$), the system continues to the Hall configuration, as shown in the lower dashed line. As the starting point for the iteration procedure, we take the states marked by the boxes in Fig. 4.8, namely ψ_s at $t = 1510.5\Omega_{ci}^{-1}$ on the upper dashed line (with an initial thickness of $\delta = 0.78d_i$) and ψ_f at $t = 1443\Omega_{ci}^{-1}$ on the lower dashed line (with an initial thickness of $\delta = 0.43d_i$).

Beginning with these initial states, we proceed with the iteration procedure. The upper solid line in Fig. 4.9 shows δ as a function of time for the first iteration

with $\epsilon = 0.7$. After a transient time where δ decreases, it increases back toward the Sweet-Parker solution. The lower solid line is a result of using $\epsilon = 0.9$. After a similar initial transient, the sheet thickness decreases toward the Hall solution.

The second iteration involves using the states on the two solid lines marked by the first vertical line (at $t = 1690.5\Omega_{ci}^{-1}$) as starting points. The upper and lower dashed lines are a result of using $\epsilon = 0.4$ and 0.6 , respectively. Again, after an initial transient, the two states go toward one or the other of the stable configurations, thus bracketing the unstable solution. Note that the system spends more time near the unstable solution in the second iteration than it does for the first, as expected.

The third iteration begins from states defined on the two dashed lines marked by the second vertical line (at $t = 1870.5\Omega_{ci}^{-1}$). The upper and lower dot-dashed lines are the results of using $\epsilon = 0.6$ and 0.7 , respectively. As above, these trajectories bracket the unstable solution and the time spent near the unstable configuration is larger still. One can see that the process is converging.

In principle, this iteration procedure could continue indefinitely. However, our computational domain has periodic boundary conditions and, therefore, only a finite amount of magnetic flux is available to be reconnected. We finish the procedure by taking an intermediate value of $\epsilon = 0.65$ in the third iteration, plotted as the middle dot-dashed line starting at $t = 1870.5\Omega_{ci}^{-1}$. The system stays at a nearly constant δ for an exceedingly long time (about $200\Omega_{ci}^{-1}$, or 7 Alfvén wave transit times down the sheet). During this time, the configuration is almost exactly in the unstable equilibrium.

What are the properties of the unstable steady-state reconnection configura-

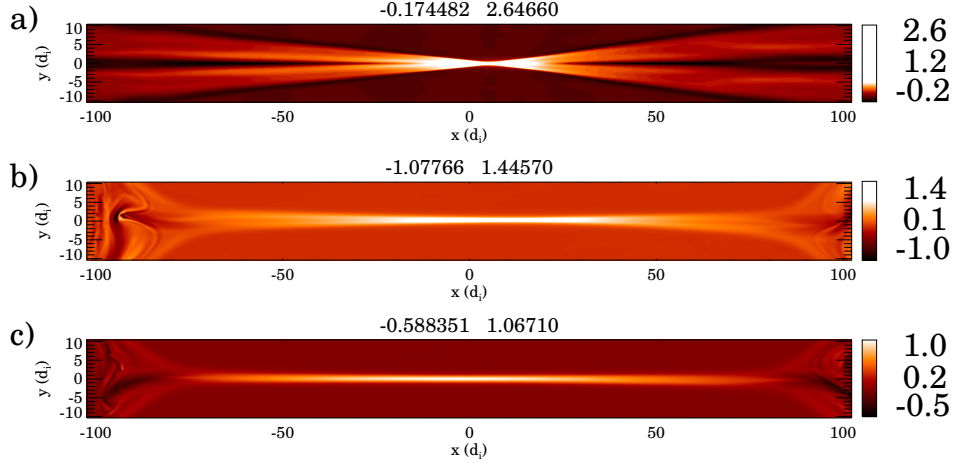


Figure 4.10: Profile of the out of plane current density J_z for the three steady-state magnetic reconnection solutions: (a) Hall, (b) the unstable solution, (c) Sweet-Parker.

tion? For $\eta = 0.015\eta_0$ as done here, the half thickness of the unstable steady-state current sheet is about $\delta = 0.51d_i$, which is clearly distinct from the Sweet-Parker and Hall steady-state values of $1.22d_i$ and $d_e = 0.2d_i$, respectively. This is plotted as the star in Fig. 3.5b. The half-length of the current sheet is about $L \simeq 30d_i$, measured as the half-width at half-maximum of the out of plane current density J_z along the sheet. The steady-state reconnection rate is $E \simeq 0.017E_0$, plotted as the star in Fig. 3.5a. For comparison, the Sweet-Parker and Hall reconnection rates are about 0.014 and 0.06, respectively, as shown in Fig. 3.5a. The reconnection rate of the unstable solution is very close to the Sweet-Parker value at this resistivity. This is likely because the whistler wave is only weakly dispersive for wavelengths comparable to d_i (see Fig. 2.8c), so the Hall effect would be relatively weak for a current sheet of thickness comparable to d_i .

The out of plane current density of the unstable solution at $t = 2055.5\Omega_{ci}^{-1}$ is shown in Fig. 4.10b. For comparison, the Hall and Sweet-Parker solutions are shown in Figs. 4.10a and c, respectively. As is to be expected, the properties of the unstable solution are intermediate between the Sweet-Parker and Hall solutions. The current sheet opens wider than the Sweet-Parker current, but not as wide as the Hall sheet. The current density is more concentrated near the X-line than for the Sweet-Parker layer, but not as much as in the Hall layer. The existence of an unstable steady-state solution has, thus, been demonstrated.

4.4 Linear Properties of the Unstable Solution

Since the solution found in the previous section is unstable, small perturbations should grow exponentially in time. By treating the difference between the upper or lower dot-dashed line of Fig. 4.9 and the unstable state (the middle dot-dashed line) as a perturbation, linear properties of the unstable mode can be studied numerically, resulting in the structure of the most unstable eigenmode and its growth rate.

The difference in δ between the unstable state (the middle dot-dashed line) and the state diverging toward the Hall solution (the lower dot-dashed line) is plotted as a function of time as the thick solid line in Fig. 4.11. The fact that the data fall nicely on a straight line indicates that the system is in a linear regime with one mode dominating the evolution and that the eigenvalue is likely purely real. The slope of the line gives a growth rate $\gamma_u \sim 0.008\Omega_{ci}$ (corresponding to a growth time of $\tau_u = 1/\gamma_u \sim 125\Omega_{ci}^{-1}$). This growth time is about half of the value of the transition

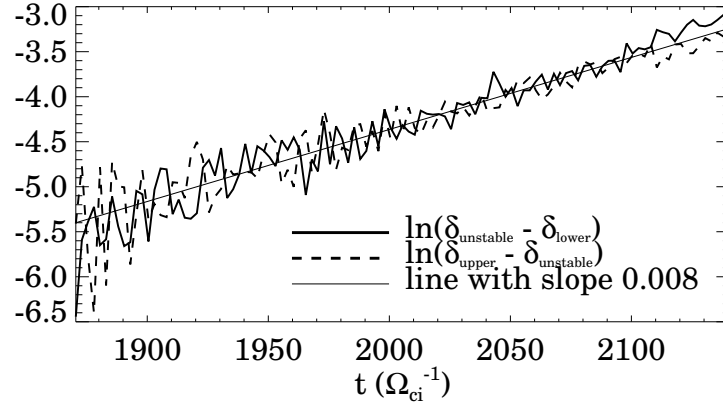


Figure 4.11: Natural logarithm of the difference in δ between the lower (upper) dot-dashed line of Fig. 4.9 and the middle dot-dashed line plotted as a function of time t as the solid (dashed) line. The slope of the line, about $0.008\Omega_{ci}$, gives the eigenvalue (growth rate) for the most unstable linear eigenmode to the unstable equilibrium.

time τ_0 found in Sec. 4.3.2, which is to be expected because τ_0 is the time it takes to go both toward and away from the unstable ghost of the Sweet-Parker fixed point. A similar analysis using the upper dot-dashed line in Fig. 4.9 (plotted as the dashed line in Fig. 4.11) leads to the same linear growth rate, as is to be expected.

What does the most unstable eigenmode look like? Fig. 4.12b-e shows eigenmodes of the three components of the magnetic field $\tilde{\mathbf{B}}$ and the electron inflow velocity \tilde{v}_{ey} zoomed in near the X-line at $t = 2045.5\Omega_{ci}^{-1}$. The eigenmodes are calculated as the difference between the system diverging towards the Hall solution (the lower dot-dashed line of Fig. 4.9) and the unstable solution. Figure 4.12a shows the magnetic field lines of the unstable equilibrium, with B_x positive (negative) below (above) the current sheet and B_y positive (negative) to the left (right) of the X-line. The perturbation reveals that the outflow region is opening out into the Petschek

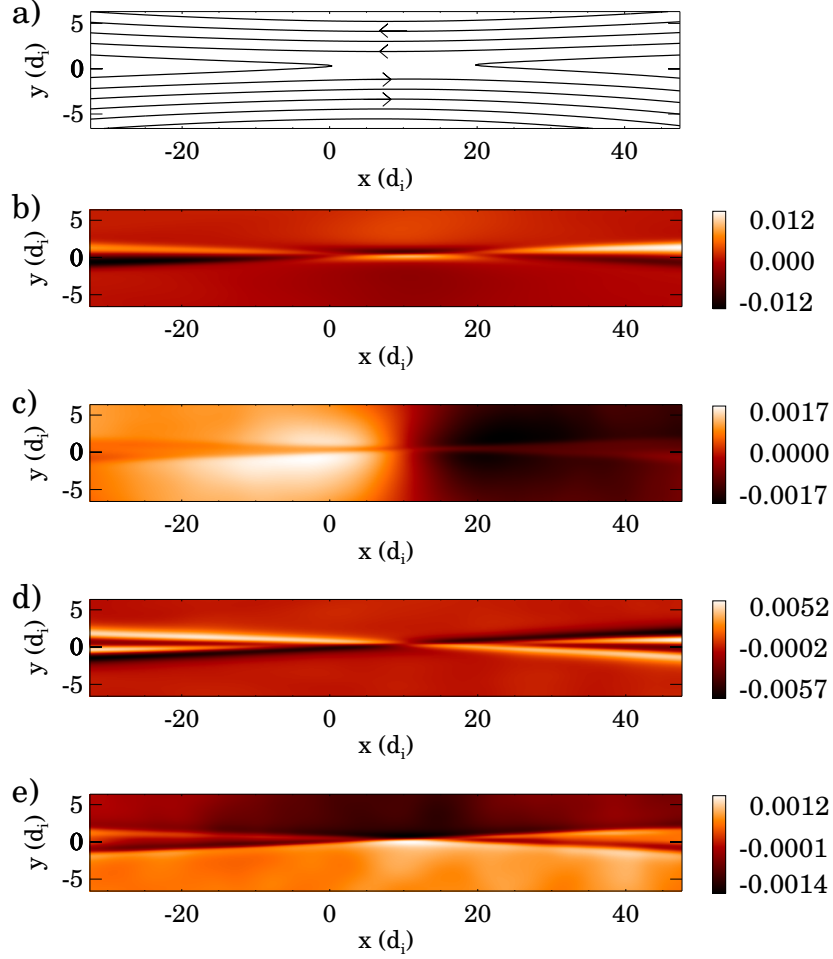


Figure 4.12: (a) Magnetic field lines of the unstable equilibrium and the structure of the most unstable eigenmode of the unstable steady-state configuration, with (b) - (d) the three components of the magnetic field $\tilde{\mathbf{B}}$ and (e) the electron inflow velocity \tilde{v}_{ey} zoomed in at the X-line.

configuration downstream of the dissipation region. This can be seen in Fig. 4.12b and c, where the bands of \tilde{B}_x to the left of $x = 0$ and to the right of $x = 20d_i$ are negative (positive) below (above) the neutral line and \tilde{B}_y is positive (negative) to the left (right) of the X-line, so the field lines downstream of the dissipation region are becoming more vertical as they open out. This opening can also be seen in the positive

and negative bands downstream of the X-line in the \tilde{v}_{ey} perturbation of Fig. 4.12e. The \tilde{v}_{ey} perturbation immediately upstream of the X-line is increasing the inflow speed, showing that the rate of reconnection is increasing. The quadrupole structure of the out of plane magnetic field perturbation \tilde{B}_z , a signature of Hall reconnection [Mandt et al., 1994], is getting stronger, as is shown in Fig. 4.12d. Interestingly, the plot of \tilde{B}_x (as well as the out of plane current density eigenmode \tilde{J}_z and density eigenmode \tilde{n} , not pictured) shows structure around the X-line with an aspect ratio of approximately 0.1. The linear eigenmode of the unstable solution, therefore, seems to contain structure with the 0.1 aspect ratio commonly seen during steady-state Hall reconnection simulations [Shay et al., 1999, Huba and Rudakov, 2004].

The same eigenmodes (with the opposite sign) are found using the upper dot-dashed line in Fig. 4.9 instead of the lower one, as must be the case in the linear regime. By similar reasoning, the perturbations serve to slow the reconnection and collapse the current sheet into the long sheet seen in Sweet-Parker reconnection.

4.5 Summary

In this chapter, we have shown that the bistable nature of magnetic reconnection dynamics can be described as a result of the existence of saddle-node bifurcations. The bifurcation model makes three predictions about the dynamics of reconnection, each of which is borne out by numerical simulations. In the next chapter, we present a physical and analytical model of reconnection dynamics which motivates why saddle-node bifurcations are present in magnetic reconnection.

Chapter 5

Toward an Analytical Theory

The dynamical model presented in Chapter 4, in which steady-state reconnection solutions are brought into and out of existence by saddle-node bifurcations, is supported by qualitative simulation results. However, a quantitative first principles analytical theory displaying saddle-node bifurcations is lacking. In its place, we present a model which motivates that saddle-node bifurcations are a natural consequence of the relevant physics of resistive Hall-MHD reconnection [Cassak et al., 2006c], namely the dispersive nature of the waves mediating the outflow from the dissipation region.

In Sec. 5.1, we present a fluid description of the dynamics of reconnection which augments the static theory of reconnection given in Chapter 2. In Sec. 5.2, we show that the dynamical model possesses saddle-node bifurcations, but only if dispersive waves are taken into account. A linear analysis of the model is performed in Sec. 5.3, in which the steady-state solutions and the eigenvalues (growth rates) of small perturbations are found. Finally, in Sec. 5.4 we make quantitative comparisons of the theoretical results to numerical simulation results, finding good overall agreement.

5.1 Dynamical Model of Magnetic Reconnection

To describe the dynamics of magnetic reconnection, first consider reconnection in the steady-state. As discussed in Sec. 2.1.3, when the rate at which magnetic field lines are convected into the dissipation region is balanced by the rate of diffusion of magnetic field lines within the dissipation region, a steady-state is maintained. Therefore, if there is an imbalance of convective inflow and dissipation, the system will not be in a steady-state. In particular, the thickness of the dissipation region will change; if convection is greater than dissipation, the layer will become thinner, while the layer will broaden if dissipation is greater than convection.

From continuity, the inflow speed is directly related to the outflow speed. What controls the outflow? The outflow is produced when recently reconnected field lines slingshot out of the dissipation region which, as discussed in Sec. 2.4, is mediated by linear waves. In resistive-MHD, the only waves available to the system are Alfvén waves. In Hall-MHD¹, Alfvén waves turn into whistler waves at a length scale on the order of the ion skin depth d_i due to the Hall effect. Whistlers are dispersive, becoming faster at smaller spatial scales.

Therefore, in a dissipation region thicker than d_i , the waves ejecting the plasma from the dissipation region are essentially Alfvén waves, and reconnection obeys the Sweet-Parker model. When the current sheet thickness δ approaches d_i , the electron outflow speed begins to increase as the waves driving the outflow become whistlers. By continuity, an increase in the outflow speed causes an increase in the inflow speed.

¹We consider only anti-parallel reconnection; component reconnection should be similar.

This increase in the inflow speed creates an imbalance of convection and diffusion, contracting the current sheet to an even smaller thickness. The outflow speed for a thinner sheet is faster still due to the dispersive nature of the whistler. This makes the imbalance of convection and dissipation even greater, making the sheet contract even more. This runaway process continues until a different dissipation mechanism, such as electron inertia, becomes important at smaller length scales, stopping the collapse.

To quantify this process, consider the scaling laws defining the steady-state Sweet-Parker model [Sweet, 1958, Parker, 1957], described by a balance of convection and diffusion as shown in Eq. 2.19,

$$\frac{v_{in}}{\delta} \sim \frac{\eta c^2}{4\pi\delta^2},$$

where v_{in} is the inflow speed and η is the resistivity. It is natural, then, to model the time evolution of δ by

$$\frac{d\delta}{dt} = -v_{in} + \frac{\eta c^2}{4\pi\delta}.$$

To allow for the effects of electron inertia, we add a “barrier” term to prevent the sheet from getting thinner than the electron skin depth d_e ,

$$\frac{d\delta}{dt} = -v_{in} + \frac{\eta c^2}{4\pi\delta} + v_{in} \frac{d_e^2}{\delta^2}. \quad (5.1)$$

As a check, simulation data of the left and right hand sides are plotted as a function of time in Fig. 5.1 for the simulation described in Sec. 3.4.1 which made a transition from Sweet-Parker to Hall reconnection when η was lowered from $\eta = 0.015\eta_0$ to $0.007\eta_0$. The agreement is encouraging.

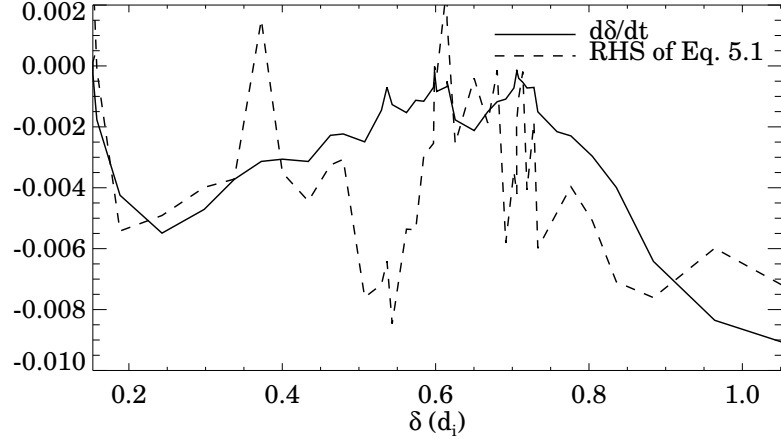


Figure 5.1: Test of Eq. 5.1 using simulation data described in Sec. 3.4.1 in which a transition from Sweet-Parker to Hall reconnection occurred when η was lowered from $0.015\eta_0$ to $0.007\eta_0$.

If one could write v_{in} as a function of δ , Eq. 5.1 equation would completely govern the time evolution of δ . Using the continuity equation (Eq. 2.9) to eliminate v_{in} gives

$$\frac{d\delta}{dt} = -\frac{\delta}{L(\delta)}v_{out}(\delta) \left(1 - \frac{d_e^2}{\delta^2}\right) + \frac{\eta c^2}{4\pi\delta}, \quad (5.2)$$

where $v_{out}(\delta)$ is the outflow speed and $L(\delta)$ is the half-length of the dissipation region.

How do we get $v_{out}(\delta)$? Since the outflow is generated by linear waves, we use the phase speed of the Hall-MHD waves as the outflow speed, evaluated with $k_y \sim 1/\delta$ (see Fig. 2.7). Using the dispersion relation in Eq. 2.61

$$\omega(k_y) = \frac{k_y c_{Ay}}{D} \left(D + \frac{k_y^2 d_i^2}{2} + \sqrt{k_y^2 d_i^2 D + \frac{k_y^4 d_i^4}{4}} \right)^{1/2}, \quad (5.3)$$

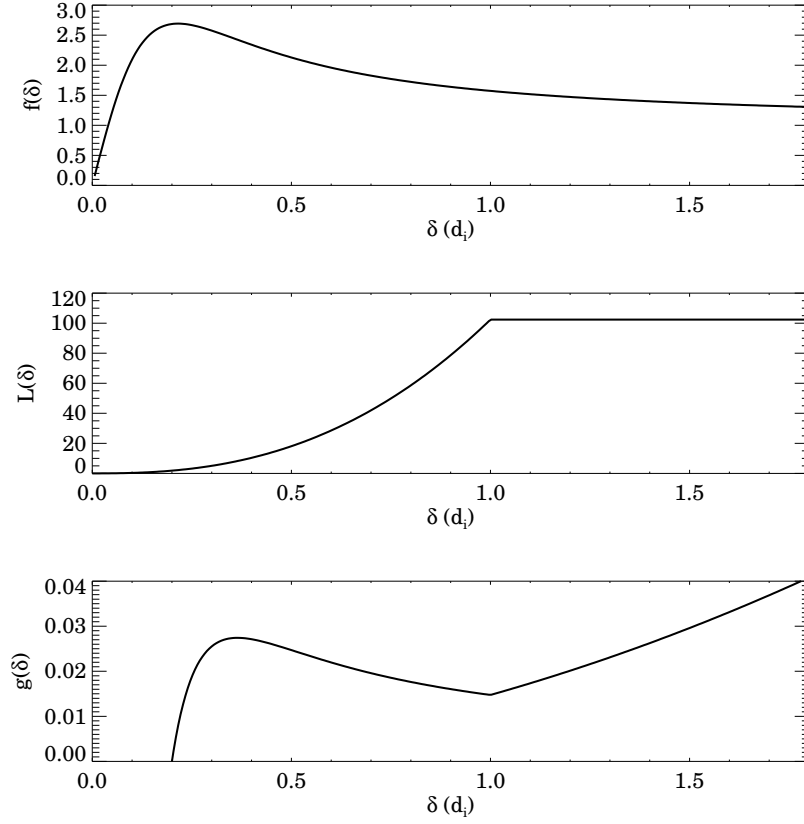


Figure 5.2: (a) Plot of $f(\delta)$, the phase velocity for Hall-MHD waves normalized to the Alfvén speed based on the upstream magnetic field strength, from Eq. 5.6 with $d_i = 1$ and $d_e = 0.2d_i$. (b) Plot of $L(\delta)$ from Eq. 5.7 with $\alpha = 2.5$. (c) Plot of $g(\delta)$ from Eq. 5.8 using $v_{out}(\delta) = c_{Aup}f(\delta)$ and $L(\delta)$ from (b).

where $D = 1 + k_y^2 d_e^2$, we find

$$v_{out}(\delta) = c_{Aup}f(\delta) \quad (5.4)$$

where $f(\delta)$ is the normalized phase speed of the waves, given by

$$f(\delta) = \frac{\omega(k_y)}{k_y c_{Aup}} = \frac{\delta^2}{\delta^2 + d_e^2} \left[1 + \frac{d_e^2}{\delta^2} + \frac{d_i^2}{2\delta^2} + \frac{d_i}{\delta} \sqrt{1 + \frac{d_e^2}{\delta^2} + \frac{d_i^2}{4\delta^2}} \right]^{1/2} \quad (5.5)$$

or in the $d_i \gg d_e$ limit,

$$f(\delta) \simeq \frac{\delta^2}{\delta^2 + d_e^2} \left[1 + \frac{d_i^2}{2\delta^2} + \frac{d_i}{\delta} \sqrt{1 + \frac{d_i^2}{4\delta^2}} \right]^{1/2} \quad (5.6)$$

The function $f(\delta)$ is plotted in Fig. 5.2a for $d_e = 0.2d_i$ as is appropriate for our simulations and in Fig. 2.8c for a realistic mass ratio. It is expected that extending this model to component reconnection can be done by merely replacing Eq. 5.6 with the appropriate phase speed derived from Eq. 2.69.

Finally, we need a model for $L(\delta)$. Unfortunately, developing a realistic functional dependence, in which L changes by a factor of 10^6 while δ changes by a factor of the mass ratio ~ 43 , as would occur for solar flares, has proven elusive. Fortunately, we will see that the gross characteristics of present model are not very sensitive to this relation. It is sufficient to know that L stays at the Sweet-Parker value L_{SP} until a transition to Hall begins, after which it decreases monotonically with δ , doing so faster than linearly. For definiteness, we describe it as a power law, namely

$$L(\delta) = \begin{cases} L_{SP} & \text{if } \delta > d_i \\ L_{SP} \left(\frac{\delta}{d_i} \right)^\alpha & \text{if } \delta < d_i \end{cases} \quad (5.7)$$

with α a constant. Since L decreases faster than δ , the only requirement on α is that it is greater than 1. This function is plotted in Fig. 5.2b for $\alpha = 2.5$. We emphasize that this relation cannot hold for realistic parameters, as it is thought that $L(\delta)$ is independent of L_{SP} during Hall reconnection. Equation 5.2 with Eqs. 5.4, 5.6 and 5.7 give a closed set of evolution equations for the current sheet thickness.

5.2 Existence of Saddle-Node Bifurcations

We now show that the model described in the previous section has saddle-node bifurcations. The steady-state solutions are found by finding the fixed points δ_* which satisfy $d\delta/dt = 0$. Setting the right hand side of Eq. 5.2 to zero gives

$$g(\delta_*) = \frac{\delta_*^2 - d_e^2}{d_i L(\delta_*)} \frac{v_{out}(\delta_*)}{c_{Aup}} = \eta', \quad (5.8)$$

where $\eta' = \eta c^2 / 4\pi c_{Aup} d_i$ as before.

As a check, consider the pure-MHD case. Since the waves generating the outflow are Alfvén waves, which are not dispersive, $v_{out} = c_{Aup}$ for all δ . Using $L(\delta) = L_{SP}$ for all δ as well leaves a quadratic relation for δ_* with one positive root, which we show in the next section is the Sweet-Parker solution. Thus, in MHD, there is only one solution and, therefore, no saddle-node bifurcations.

Returning to the Hall-MHD case, solutions to Eq. 5.8 can be obtained graphically by finding the intersection(s) of $g(\delta)$ as a function of δ with a horizontal line corresponding to a given η' . Using the functional form for $f(\delta) = v_{out}(\delta)/c_{Aup}$ and $L(\delta)$ from Eqs. 5.6 and 5.7, we see that $g(\delta)$ goes to $-\infty$ as δ goes to 0, while $g(\delta)$ goes to ∞ as δ goes to ∞ . Since $g(\delta)$ is continuous, there is always at least one fixed point for any η' . Also, $f(\delta)$ has a local maximum near d_e (see Fig. 5.2a) while $1/L$ goes down from ∞ at $\delta = 0$, reaching its minimum value of $1/L_{SP}$ at $\delta = d_i$. The function $g(\delta) \propto f(\delta)(\delta^2 - d_e^2)/L(\delta)$ must have a local maximum near d_e and a local minimum near d_i . Therefore, the function $g(\delta)$ starts from negative infinity, reaches a peak near d_e , comes back to a minimum near d_i , then continues upward toward positive infinity. For the special case of $\alpha = 2.5$, $g(\delta)$ is plotted in Fig. 5.2c. In the

region between the local maximum near $\delta = d_e$ and the local minimum near $\delta = d_i$, a horizontal line crosses the curve three times, meaning that there are three steady-state solutions for a range of η' and only one outside of this range. The changeover from one solution to three solutions as η' varies past the local maximum or local minimum are saddle-node bifurcations. It is important to note the necessity of the dispersive waves in causing the existence of the saddle-node bifurcations. We will show in the next section that one of the solutions is the Hall solution, so the present model gives a dynamical theory linking dispersive waves and fast Hall reconnection.

5.3 Linear Analysis

A further analysis of the evolution equation presented in Sec. 5.1 can provide theoretical estimates for the linear properties of the system. In particular, we find the current sheet thicknesses δ_* of all steady-state equilibria and the growth rate of small perturbations to these steady-state solutions. We treat the Sweet-Parker ($\delta > d_i$) and Hall ($\delta < d_i$) regimes separately.

5.3.1 Sweet-Parker Regime

In the Sweet-Parker regime, L is set by the system size $L = L_{SP}$, essentially independent of δ , as assumed in Eq. 5.7. The outflow speed is given by the Alfvén speed based on the upstream magnetic field strength, $v_{out} \sim c_{Aup}$, also independent of δ (*i.e.*, $f(\delta) \simeq 1$). Then, Eq. 5.2 reduces to

$$\frac{d\delta}{dt} = -\delta \frac{c_{Aup}}{L_{SP}} \left(1 - \frac{d_e^2}{\delta^2} \right) + \frac{\eta c^2}{4\pi\delta} \simeq -\delta \frac{c_{Aup}}{L_{SP}} + \frac{\eta c^2}{4\pi\delta} \quad (5.9)$$

since $\delta > d_i \gg d_e$. The fixed points δ_{SP} are the points for which the right hand side vanishes. Thus,

$$\frac{\delta_{SP}^2}{L_{SP}^2} = \frac{\eta c^2}{4\pi c_{Aup} L_{SP}}, \quad (5.10)$$

which is the standard Sweet-Parker scaling result of Eq. 3.1.

The stability of the fixed point is found by linearizing Eq. 5.9 about the fixed point δ_{SP} and finding the growth rate γ_{SP} of small perturbations to the Sweet-Parker equilibrium. The result is

$$\gamma_{SP} = -2 \frac{\eta c^2}{4\pi \delta_{SP}^2} = -2 \frac{c_{Aup}}{L_{SP}} \quad (5.11)$$

which shows that the Sweet-Parker fixed point is unconditionally stable ($\gamma_{SP} < 0$) and that perturbations have a decay time of half an Alfvén wave transit time along the Sweet-Parker current sheet. It is important to emphasize that this is not the growth rate of the tearing mode, it is the growth rate of small perturbations to the steady-state Sweet-Parker solution.

5.3.2 Hall Regime

In the Hall regime with $\delta < d_i$, we return to Eq. 5.2 and repeat the above analysis. The fixed points are solutions of Eq. 5.8. A stability analysis can be performed and growth rates obtained by linearizing Eq. 5.2 about each fixed point δ_* . In general, it can be shown that the growth rate γ_* of small perturbations to the equilibria are

$$\gamma_* = -\frac{\eta c^2}{4\pi \delta_*^2} \left(\frac{2\delta_*^2}{\delta_*^2 - d_e^2} + \left. \frac{d \ln v_{out}}{d \ln \delta} \right|_{\delta_*} - \left. \frac{d \ln L}{d \ln \delta} \right|_{\delta_*} \right). \quad (5.12)$$

This equation clearly reduces to Eq. 5.11 in the MHD limit in which v_{out} and L are independent of δ .

From Fig. 5.2c, we see that the leftmost fixed point occurs at relatively small δ , close to d_e . This corresponds to the Hall solution. To find the fixed point δ_H , we assume that δ_H is close to d_e by letting $\delta_H = d_e + \tilde{\delta}$ for small $\tilde{\delta}$ and expanding Eq. 5.8 to first order in $\tilde{\delta}$. This gives

$$\delta_H \sim d_e + \eta' L(d_e). \quad (5.13)$$

Since $L(d_e) \simeq 2d_i$ in the simulations and $\sim 10d_i$ in Nature and $\eta' \ll 1$, the assumption of $\tilde{\delta}$ small compared to d_e is justified.

To find the growth rate γ_H of small perturbations to the Hall equilibrium, we use Eq. 5.12. The first term in the parentheses dominates the other two because it goes like $1/\eta'$, while the second term is close to zero (see Fig. 5.2a at $\delta \sim d_e$), and the third term is merely α , a number of order 1. Thus,

$$\gamma_H \sim -\frac{c_{Aeup}}{L(\delta_H)} \sim -\frac{v_{out}(\delta_H)}{L(\delta_H)}, \quad (5.14)$$

which is independent of the resistivity η to leading order, as expected of Hall reconnection. Note, as with the Sweet-Parker solution, the equilibrium is unconditionally stable ($\gamma_H < 0$).

Finally, we analyze the third solution, corresponding to the middle intersection of $g(\delta)$ by η' , which we will see is unstable to small perturbations. Consider a normalized resistivity η' sufficiently far from the critical values where the bifurcations occur (as in the simulations in Sec. 4.3.3) so that it is safe to assume that the fixed

point δ_u satisfies $d_e \ll \delta_u \ll d_i$. Then, from Eq. 5.6, $f(\delta_u) \sim d_i/\delta_u$, as would be expected in the pure whistler regime. Eq. 5.8 gives a fixed point of

$$\delta_u \sim \eta' L(\delta_u). \quad (5.15)$$

This is not a closed form solution for δ_u , but can be checked for consistency using the value for $L(\delta_u)$ from the simulations, which we do in the following section. The growth rate γ_u of the unstable solution is given by Eq. 5.12. The first term is close to 2 since $\delta_u \gg d_e$, while the second term is close to -1 since $v_{out} \sim 1/\delta$ for the whistler wave. The third term is merely α , so

$$\gamma_u \sim (\alpha - 1) \frac{\eta c^2}{4\pi \delta_u^2} \sim (\alpha - 1) \frac{c_{Aup} d_i}{\eta' L(\delta_u)^2}. \quad (5.16)$$

Since $\alpha > 1$ as discussed in Sec. 5.1, this fixed point is unconditionally unstable. Note, this is the only place that the functional form of $L(\delta)$ enters the linear analysis, but the gross conclusions are insensitive to the precise functional form.

5.4 Comparison to Numerical Results

We now make quantitative comparisons of the linear and nonlinear predictions of the analytical model to the numerical simulations. We use a value of $\alpha = 2.5$ for the exponent in the function $L(\delta)$ because in the simulations, L goes from $\sim 100d_i$ to $\sim 2d_i$ while δ goes from d_i to $d_e = 0.2d_i$, so choosing $\alpha = 2.5$ makes $L(d_e) \simeq 2d_i$. We emphasize that this relationship cannot hold for realistic parameters.

The predictions for the critical normalized resistivities at which bifurcations occur can be read off of Fig. 5.2c, giving $\eta'_{sf} \simeq 0.0148$ and $\eta'_{fs} \simeq 0.0274$. This agrees

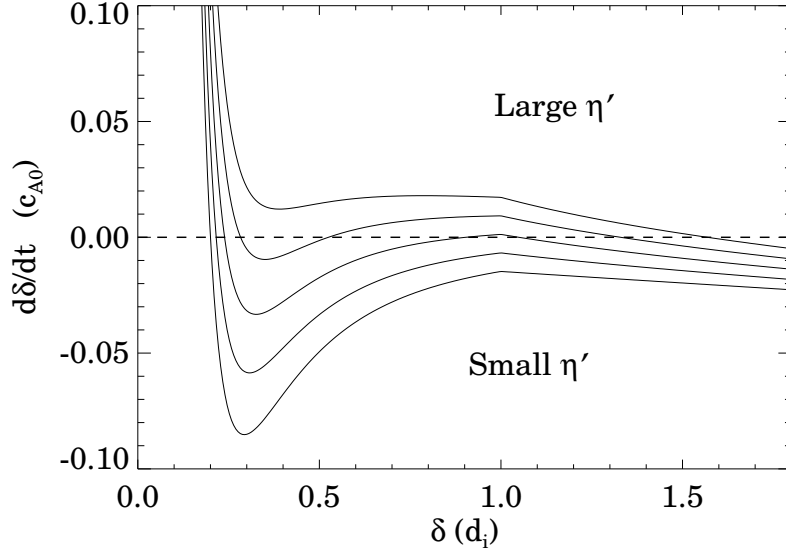


Figure 5.3: Phase portrait for the dynamical model of Eq. 5.2 with $\alpha = 2.5$ for $\eta' = 0.0, 0.008, 0.016, 0.024,$ and 0.032 . The curve moves up for larger η' . This is qualitatively similar to Fig. 4.1.

rather well with the numerical results of $\eta'_{sf} \sim 0.011$ and $\eta'_{fs} \sim 0.024$ found in the simulations discussed in Sec. 3.4.1. The phase portrait for this model is plotted for $\eta' = 0, 0.008, 0.016, 0.024,$ and 0.032 in Fig. 5.3, showing a strong resemblance to the phase portraits in Figs. 4.1 and 4.5.

Comparisons with the simulation results for the equilibrium current sheet thicknesses δ_* and growth rates γ_* can also be made. For the Sweet-Parker solution, we have already shown that the Sweet-Parker prediction of the current sheet thickness is borne out by simulations. For the growth rate, $L_{SP} \sim 90d_i$ and $c_{Aup} \sim 0.93c_{A0}$, so $\gamma_{SP} \simeq -0.02\Omega_{ci}$, corresponding to a decay time of $\tau_{SP} = 1/|\gamma_{SP}| \simeq 50\Omega_{ci}^{-1}$. This compares favorably with the time taken for the sheet to thin to the ghost Sweet-Parker thickness seen in Figs. 4.4a - d.

For the Hall solution, the outflow speed is measured to be $v_{out} \simeq 1.1c_{A0}$ and $L(\delta_H) \simeq 2d_i$, so $\gamma_H \simeq -0.55\Omega_{ci}$, corresponding to a growth time of $\tau_H = 1/|\gamma_H| \simeq 2\Omega_{ci}^{-1}$. This can readily be compared with the slope of the lines going into the Hall fixed point in Fig. 4.5, which gives $\gamma_H \simeq -0.15\Omega_{ci}$. While the agreement is not very strong, it is important that both the measured and theoretical values for τ_H are far shorter than resistive and Sweet-Parker time scales. Furthermore, for the simulation parameters, the α term is not negligible compared to the first term in Eq. 5.12, which would help the agreement.

As a further check of consistency, the model predicts a weak dependence on η' for the thickness of the steady-state Hall current sheet. This is borne out in simulations, as seen in Fig. 4.8, where the dashed line with $\eta = 0.015\eta_0$ asymptotes to $\delta_H \simeq 0.19d_i$, while the solid line with $\eta = 0.007\eta_0$ asymptotes to $\delta_H \simeq 0.16d_i$. The difference of $0.03 d_i$ agrees well with the theoretical difference of $(\Delta\eta')L(\delta_H) \simeq 0.02d_i$.

For the unstable solution, for which $\eta = 0.015\eta_0$, the upstream magnetic field strength is measured to be $0.58B_0$, the outflow speed is $1.2c_{A0}$, and the sheet length is $28d_i$. Eq. 5.15 predicts an equilibrium current sheet thickness of $\delta_u \simeq 0.72d_i$, in reasonably good agreement with the measured value of $0.51d_i$. (Recall, the simulation result for the thickness is obtained using the half-width at half-maximum, which underestimates δ .) For the simulation parameters with $\alpha = 2.5$, Eq. 5.16 gives a growth rate of $\gamma_u \simeq 0.089\Omega_{ci}$. This is an order of magnitude larger than the simulation result of $\gamma_u \sim 0.008$ given in Sec. 4.3, which is not surprising since this value is sensitive to α , which was chosen rather arbitrarily.

The analytical model presented here, therefore, shows encouraging agreement with numerical simulation results, both for quantities describing nonlinear behavior (η'_{sf} and η'_{fs}) and linear behavior (δ_* and γ_* for all three steady-state solutions).

5.5 Summary

In this chapter, we have constructed a physical model of magnetic reconnection dynamics. This simple model predicts the existence of saddle-node bifurcations, which provides a theoretical motivation for the bistability and saddle-node bifurcations predicted and observed in Chapters 3 and 4, and the importance of dispersive waves to their occurrence. Furthermore, linear and nonlinear properties of the analytical model show good agreement with the results of numerical simulations. It is perhaps surprising that a system governed by seven partial differential equations can be described so robustly by a simple model based on a single first order ordinary differential equation with only one parameter. This suggests that two dimensional Hall-MHD reconnection has symmetries and/or similarities greatly reducing the effective dimensionality of the system. In the next chapter, we turn from fundamental questions about the dynamics of reconnection to the Onset Problem to how reconnection begins abruptly in magnetic explosions in Nature.

Chapter 6

Catastrophic Onset of Fast Magnetic Reconnection

The previous three chapters have described results about the dynamics of magnetic reconnection. We now return to the application which motivated this study - what causes the onset of magnetic explosions? In particular, how is it that large amounts of energy can accrue without setting off the trigger for fast magnetic reconnection and under what conditions does the trigger go off? We propose that the onset of fast magnetic reconnection is the result of a catastrophic transition from Sweet-Parker to Hall reconnection. Since Sweet-Parker reconnection is so slow in physical systems of interest, it would appear to an observer that almost no reconnection would be occurring. For example, the Sweet-Parker inflow speed for solar flare parameters was found in Sec. 2.2 to be only ~ 80 cm/s, far too slow to be observed. During Sweet-Parker reconnection, magnetic energy accumulates faster than it is released, leading to the storage of magnetic energy.

In Sec. 6.1, we consider the conditions under which a transition from Sweet-Parker to Hall reconnection occurs. In particular, we show that the catastrophic onset of Hall reconnection can happen spontaneously, *i.e.*, without external influences, first published in Ref. [Cassak et al., 2006b]. This result may be crucial to understanding reconnection in the solar corona, fusion devices and laboratory experiments. In Sec. 6.2, we present the results of numerical simulations which verify

the spontaneous catastrophic onset of Hall reconnection. In Sec. 6.3, we discuss observations of spontaneous onset of magnetic reconnection in laboratory experiments and in “flux emergence reconnection” in the solar corona which are consistent with the model presented here. Finally, in Sec. 6.4, we make qualitative and quantitative comparisons of the model to explosive reconnection events in the solar corona and the laboratory, showing that predictions of the model are quantitatively consistent with observations of eruptions in the solar corona.

6.1 Conditions Under Which a Transition Occurs

The bifurcation model presented in Chapter 4 provides two possible scenarios which produce a sudden onset of fast magnetic reconnection. One way to start Hall reconnection happens at a fixed η' in the region of bistability, as depicted in Fig. 6.1a. If the system is undergoing Sweet-Parker reconnection, a transition would occur if a large enough external force compresses the current layer to a thickness less than the thickness of the unstable solution’s current layer (to its left in the figure). Then, the system would evolve toward the Hall configuration. This suggests the perhaps surprising result that the current sheet has to be compressed somewhat thinner than d_i (as opposed to only d_i) in order to cause a transition to Hall reconnection¹. This is consistent with recent simulations of forced magnetic reconnection [Sullivan et al., 2005]. Onset by forcing is probably not a candidate for reconnection in the solar corona or for the sawtooth crash, so we consider it no further.

¹As before, we treat only anti-parallel reconnection in the discussion, but component reconnection should follow the same arguments with d_i replaced by the ion Larmor radius ρ_s .

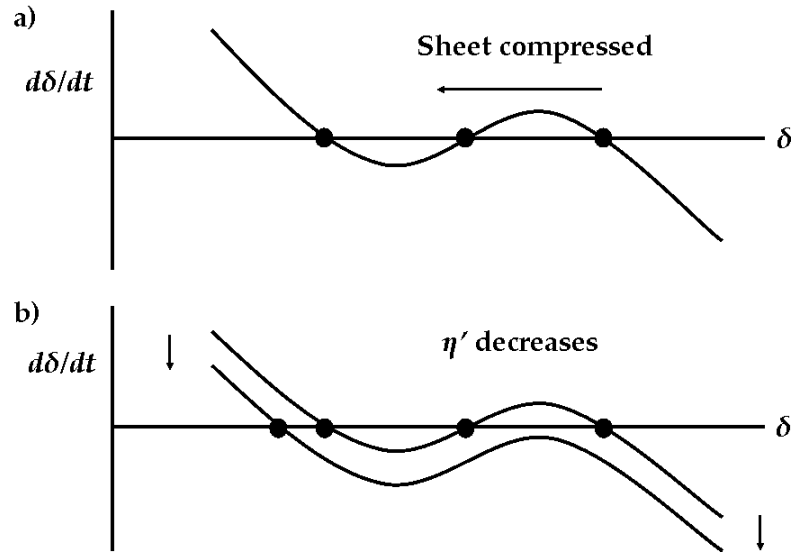


Figure 6.1: Schematic diagram of two possible onset mechanisms. (a) At constant η' in the bistable regime, a compression making the current sheet thinner than the unstable equilibrium will lead to a transition to Hall reconnection. (b) A decrease in η' leads to a saddle-node bifurcation at a critical value, at which the system must go to the Hall solution.

A theoretically more satisfying onset scenario occurs due to a bifurcation caused by a variation in η' . Suppose a system is undergoing Sweet-Parker reconnection with η' dynamically decreasing, *i.e.*, the current sheet thickness δ is shrinking toward the ion skin depth d_i . When η' goes below the critical value η'_{sf} , a saddle-node bifurcation occurs and the Sweet-Parker solution disappears. This is pictured schematically in Fig. 6.1b. The only steady-state solution that remains is the Hall solution, so the system must make a transition to the Hall solution. This transition is catastrophic because a small continuous change in a control parameter causes a discontinuous jump in the equilibrium configuration of the system.

How does $\eta' = \eta c^2 / 4\pi c_{Aup} d_i$ decrease dynamically? One way is if the classical resistivity η decreases. This can occur, for example, through an increase in the ambient temperature, either as a result of reconnection or through external means. This scenario was verified with simulations described in Sec. 3.4.1, with the caveat that the resistivity was changed discontinuously instead of continuously as one would expect in Nature. This mechanism is of potential importance for the onset of the sawtooth crash, which we discuss further in Sec. 6.4.3.

A second mechanism for the decrease of η' is through an increase in the upstream magnetic field strength B_{up} , thereby increasing the upstream Alfvén speed c_{Aup} . While intuitively it might seem that this would require external forcing to bring stronger field lines into the dissipation region, it was shown [Cassak et al., 2006b] that the increase in upstream magnetic field strength is generic to the reconnection process and actually occurs spontaneously.

To see how this works, consider a macroscopic current layer of half-thickness W_s with a small but non-negligible resistivity. If it is unstable to reconnection, it will undergo Sweet-Parker reconnection because without small scale structure on length scales of the ion skin depth d_i , the Hall term in the generalized Ohm's Law (Eq. 2.24) is unimportant. However, since the resistivity is small, the thickness δ_{SP} of the dissipation region (given by Eq. 2.20) will be much smaller than the macroscopic thickness of the current layer W_s , *i.e.*, the Sweet-Parker layer is embedded in the macroscopic current layer (see Fig. 6.2). As such, the magnetic field B_{up} immediately upstream of the dissipation region is much smaller than the asymptotic large scale magnetic field. As reconnection progresses, inflow convects stronger magnetic

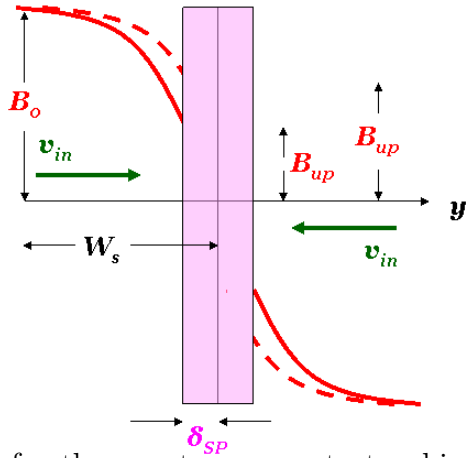


Figure 6.2: Model for the spontaneous catastrophic onset of fast magnetic reconnection. The Sweet-Parker dissipation region is much smaller than global scales, so it is embedded in a wider current sheet. Therefore, it sees a smaller upstream magnetic field strength. The reconnection inflow convects in stronger magnetic fields which thins the layer. If the layer becomes smaller than d_i , a transition to Hall reconnection occurs.

fields into the dissipation region (as shown by the dashed line in Fig. 6.2), even without external forcing. An increase in B_{up} leads to a decrease in the thickness of the dissipation region (from Eq. 2.20). If the asymptotic magnetic field is strong enough to make the dissipation region thinner than d_i , a transition to Hall reconnection eventually ensues. Thus, the inflow from the reconnection itself drives the dissipation region to the critical state at which a transition to Hall reconnection occurs. In the next section, we verify this spontaneous catastrophic onset mechanism with numerical simulations; in Sec. 6.4, we consider applications of this model to reconnection in the solar corona and laboratory plasmas.

6.2 Spontaneous Onset Simulation Results

We perform a simulation of reconnection in a wide current sheet with a small resistivity η such that $\eta' = \eta c^2 / 4\pi c_{Aup} d_i$ is below the critical value η'_{sf} when B_{up} equals the asymptotic magnetic field strength B_0 , but greater than η'_{sf} when B_{up} is somewhat less than B_0 , and let the system evolve without external influence. The computational domain and grid scale parameters are the same as that for the anti-parallel simulations summarized in Sec. 3.3. Unlike the simulations in Chapter 3, however, the initial equilibrium magnetic field is given by one period of a cosine sheet, $B_{x0}(y) = B_0 \cos(2\pi y/L_y)$, where L_y is the size of the domain in the inflow direction, corresponding to an initial current sheet thickness of $w_0 = 102.4d_{i0}$ in order to dramatize the effect of the wider sheet. Pressure balance is enforced by a non-uniform density profile, $n(y) = n_0 + (B_0^2/8\pi T_0) \sin^2(2\pi y/L_y)$, where $T_0 = B_0^2/4\pi n_0$ is the temperature, assumed constant and uniform for simplicity. The initial density at the center of the current sheet is, therefore, $1.5n_0$. Lengths are normalized to the ion skin depth d_{i0} based on the density n_0 at the edge of the computational domain, not the center of the X-line, which we denote as d_{iX} . There is no imposed guide field.

Simulations are performed with $\eta = 0.0025\eta_0$ and $0.0090\eta_0$, both of which exhibit transitions to fast reconnection. We present results from the $\eta = 0.0025\eta_0$ simulation, which was initialized from the $\eta = 0.0090\eta_0$ simulation at $t = 5.364 \text{ k}\Omega_{ci}^{-1}$. Initializing the simulation in this way introduces transient behavior, but it dies away (by $t \sim 11 \text{ k}\Omega_{ci}^{-1}$) before small scale dynamics become important.

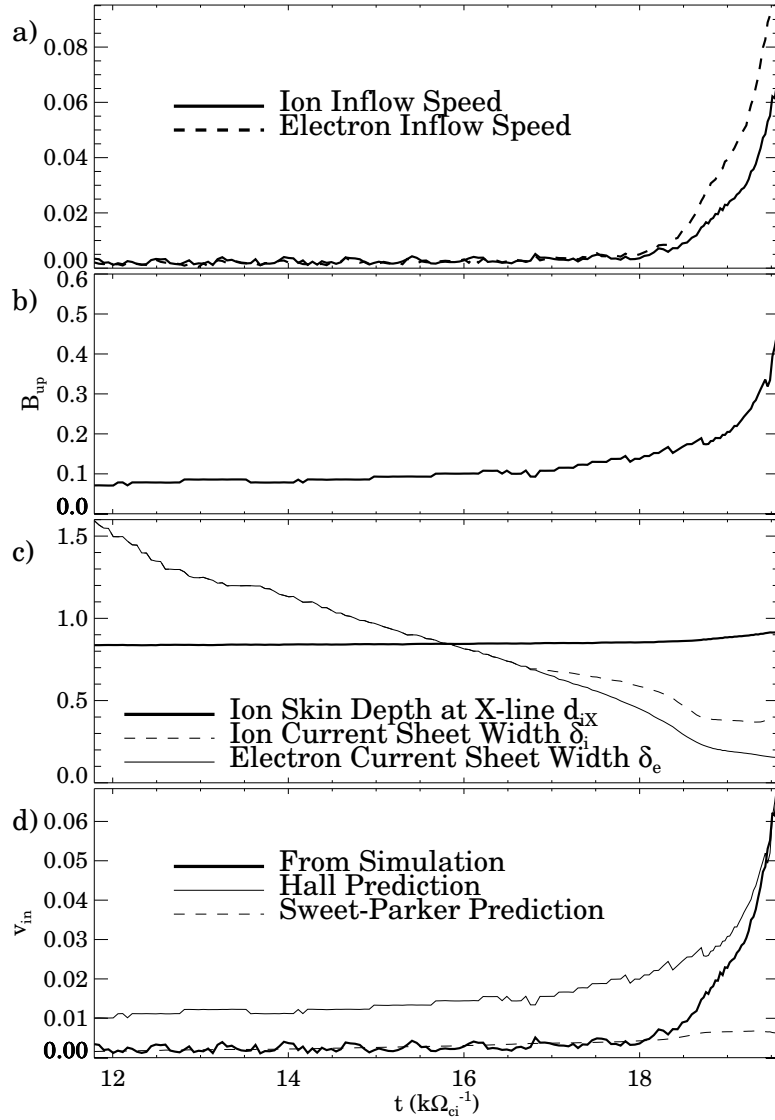


Figure 6.3: Time dependence (in thousands of ion cyclotron times) of the (a) ion (solid) and electron (dashed) inflow velocities, (b) upstream magnetic field strength B_{up} , (c) electron (thin solid) and ion (dashed) current sheet thicknesses δ_e and δ_i and ion skin depth (thick solid) at the X-line d_{iX} , and (d) ion inflow velocity from the simulation (thick solid), with Sweet-Parker theory (dashed, from Eq. [2.19]) and Hall theory (thin solid, from Eq. [2.32] with 0.17 replacing 0.10). ©2006 by The American Astronomical Society.

When the system is evolved in time, the Hall effect is initially very small because the thickness of the current layer $W_s \simeq 102.4d_{i0}$ is large compared to d_{iX} , so the system evolves essentially as it would in pure resistive MHD. A Sweet-Parker current sheet develops, as we will demonstrate later. The ion and electron inflow velocities, measured as the maximum value of the inflow into the X-line for each species, are plotted as a function of time late in the simulation in Fig. 6.3a. Up until $t \sim 18 \text{ k}\Omega_{ci}^{-1}$, the electrons and ions are coupled as expected in MHD. The inflow speed is very small, but slowly rises due to a gradual increase in the upstream magnetic field strength B_{up} as stronger magnetic fields are convected into the dissipation region. Fig. 6.3b shows the slow increase in B_{up} , measured just upstream of the dissipation region.

When the ions decouple from the electrons, the inflow speeds begin to increase dramatically and the system begins a transition to Hall reconnection. This transition initiates when the thickness of the current sheet δ falls below d_{iX} , as is shown in Fig. 6.3c. The thick solid line is d_{iX} as a function of time. After decoupling, one must distinguish between the electron and ion current sheet thicknesses, which we denote as δ_e and δ_i , respectively. The solid line is δ_e , determined by the half-width at half-maximum of the total out of plane current density J_z . The dashed line is δ_i , determined by the greater of δ_e and the half-width at half-maximum of the total inflow current density J_y . The latter becomes non-zero where the electrons and ions decouple, and is therefore a measure of the edge of the ion dissipation region. One can see δ_i decreasing from large scales (larger than d_{iX}) as the upstream magnetic field increases, and the transition begins when it is of the order of d_{iX} .

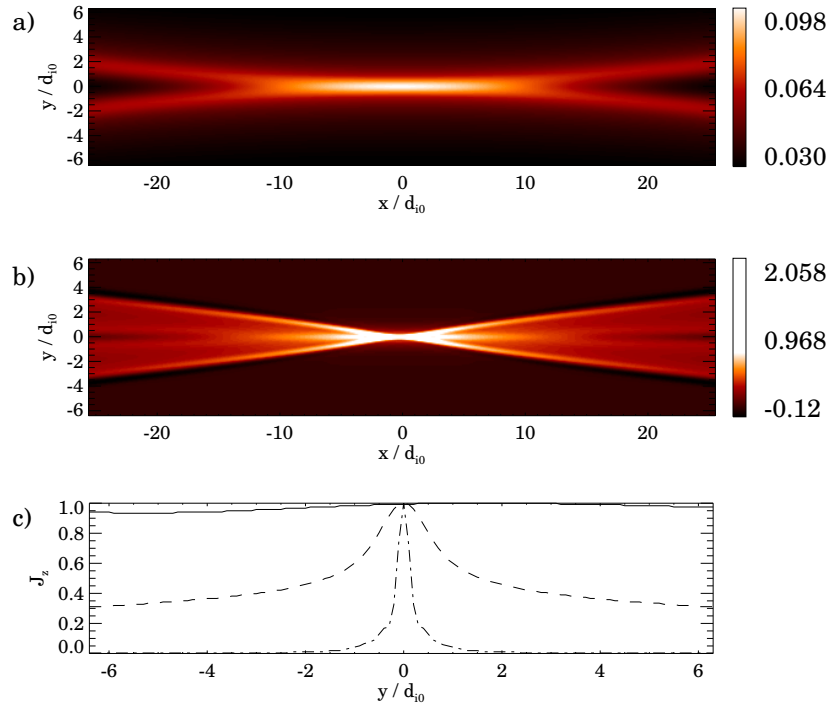


Figure 6.4: Grayscale plot of the current sheet during (a) Sweet-Parker reconnection (at $t = 11.4 \text{ k}\Omega_{ci}^{-1}$) and (b) Hall reconnection (at $t = 19.6 \text{ k}\Omega_{ci}^{-1}$). (c) Cuts across the X-line for the same two sheets (dashed and dot-dashed, respectively) normalized to its maximum value. The initial current sheet profile is the solid line. Notice the color table for (b) has been skewed for greater contrast and the amplitude of the current density is vastly different for the two sheets. ©2006 by The American Astronomical Society.

Finally, to verify that the system is undergoing Sweet-Parker reconnection before the transition and Hall reconnection after, we must check the validity of the inflow speed predictions from Eqs. 2.19 and 2.32. The thick solid line of Fig. 6.3d shows the ion inflow speed v_{in} as a function of time. The dashed line is the Sweet-Parker prediction from Eq. 2.19 ($v_{in} \sim \eta/\delta$ in code units), while the thin solid line is the Hall reconnection prediction with a constant coefficient of 0.17, which

is of the order of ~ 0.10 as expected from Eq. 2.32. Clearly, up until about $t \sim 18 \text{ k}\Omega_{ci}^{-1}$, there is excellent agreement with the Sweet-Parker result. A grayscale plot of the current sheet during the Sweet-Parker phase (at $t = 11.4 \text{ k}\Omega_{ci}^{-1}$) is shown in Fig. 6.4a, showing the characteristic elongated dissipation region (similar to those observed with pure MHD simulations by [Jemella et al., 2004]). After a relatively brief transition time lasting until $t \sim 19.5 \text{ k}\Omega_{ci}^{-1}$, the inflow speed is well modeled by the Hall prediction. A grayscale plot of the current sheet during the Hall phase (at $t = 19.6 \text{ k}\Omega_{ci}^{-1}$) is shown in Fig. 6.4b, showing the Petschek open outflow configuration characteristic of Hall reconnection. We observe a large enhancement of the quadrupolar structure in the out of plane magnetic field, a signature of Hall reconnection [Mandt et al., 1994]. Cuts across the current sheet at the X-line normalized to its maximum value are plotted as the dashed line and dot-dashed lines in Fig. 6.4c, showing that δ_e falls to $d_e = 0.2d_i$ during Hall reconnection, as is expected when electron inertia provides the dissipation. For comparison, the solid line is a cut across the initial equilibrium current sheet.

Therefore, the simulations show that the catastrophic onset of Hall reconnection happens due to an increase in the upstream magnetic field strength, and this occurs spontaneously - without any external forcing.

6.3 Observational Evidence for Spontaneous Catastrophic Onset

We now spotlight two recent observations of spontaneous onset of fast magnetic reconnection; one in a laboratory experiment, one in the solar corona.

6.3.1 Spontaneous Onset at the Versatile Toroidal Facility (VTF)

We revisit the experimental observations of spontaneous reconnection onset at VTF, as discussed in Sec. 1.4.4. It was found that reconnection can begin spontaneously a relatively long time after external forcing has been stopped in a small percentage of shots. From Table 1.2 in Sec. 1.4, the parameters at VTF satisfy $\beta \ll 1 \ll \beta_{rec}$, where $\beta = c_s^2/c_A^2$ and $\beta_{rec} = c_s^2/c_{Aup}^2$, so the system is in the component reconnection (kinetic Alfvén wave) regime as discussed in Sec. 2.4.3. Thus, the present model suggests that a catastrophic onset of Hall reconnection will occur only if the thickness of the dissipation region falls below ρ_s . Preliminary diagnostics suggest that the thickness of the current sheet at onset is very close to the ion Larmor radius $\rho_s \sim 10$ cm [Egedal et al., 2006], consistent with the present model. Future studies at VTF are planned to carefully quantify the conditions under which the transition occurs and to affirm that kinetic Alfvén dynamics are present.

6.3.2 Flux Emergence Reconnection in the Solar Corona

A recent set of observations of non-eruptive reconnection in the corona provides another example of seemingly spontaneous reconnection onset. Using the Transition Region and Coronal Explorer (TRACE) satellite, a high resolution multiple wavelength satellite launched in 1998, researchers [Longcope et al., 2005] watched a flux rope as it emerged into the corona from the chromosphere, not far from a pre-existing active region. Initially, the two active regions were not magnetically connected. However, as time elapsed, the two active regions became magnetically

connected, which is only possible through magnetic reconnection.

The reconnection rate was quantifiable throughout the process as newly reconnected flux tubes became dark in the TRACE images, making them relatively easy to count. Observations showed that reconnection was very slow for the first ~ 24 hr, but measurably non-zero and fairly steady. During this time, magnetic energy accumulated. Then, with no visible trigger [Longcope et al., 2005], fast reconnection began and continued for ~ 3 hr until the accumulated energy was released. The energy released during fast reconnection was shown to be comparable to the energy accumulated during slow reconnection. Based on parameters inferred from the observations ($L \sim 3 \times 10^4$ km, $n \sim 10^9$ cm $^{-3}$, a loop voltage of 10^9 V, a separator length of 2×10^5 km, and a sheet current of $I \sim 1.34 \times 10^{11}$ A [Longcope et al., 2005]), the fast reconnection rate was $E' \sim 0.05$, based on a reconnection electric field of $E \sim 5$ V/m and a reconnecting magnetic field of $B_0 \sim 4$ G, consistent with Hall reconnection. Interestingly, the reconnection rate stayed at a near steady value for most of the 3 hr. These observations provide solid evidence for the accumulation of magnetic energy during a slow reconnection phase followed by a spontaneous onset of fast reconnection, consistent with the model presented here.

6.4 Applications To Reconnection Events in Nature

In this section, we consider applications of the onset model of Sec. 6.1 to the onset of solar eruptions, self-organized criticality models of the solar corona, and the onset of the sawtooth crash.

6.4.1 Onset of Solar Eruptions

A rigorous comparison of this model with flare observations is challenging because the dissipation region is much narrower than can be resolved with satellite or ground-based observations. We can, however, compare some basic predictions with observations.

For the model to be plausible, the parameters must be such that the Sweet-Parker dissipation region thickness δ_{SP} is initially larger than d_i , but must be able to become smaller than d_i as time evolves. From Table 1.2, we see that δ_{SP} based on the asymptotic magnetic field is $\simeq 200$ cm, which is smaller than $d_i \simeq 400$ cm. Since δ_{SP} will be larger for the smaller magnetic field strengths which occur early in reconnection, is it therefore true that the conditions in the solar corona are consistent with this model. Turning this argument around, we can calculate the critical upstream magnetic field strength B_* which would make the thickness of a Sweet-Parker current sheet equal to d_i . Setting $\delta = d_i$ in Eq. 2.20, we find

$$B_* \sim \sqrt{4\pi m_i n} \left(\frac{\eta c^2}{4\pi d_i^2} L \right). \quad (6.1)$$

Using the values from Table 1.1 in Sec. 1.4 gives $B_* \simeq 27$ G. If this value were too large, our model would suggest that a catastrophic onset would never occur; if this value were too small, our model would suggest that enough energy would not have time to accrue. Since the ambient magnetic field strength is on the order of 100 G, this prediction shows that the critical magnetic field is, indeed, accessible during reconnection in the corona².

²It also confirms earlier statements [Priest and Forbes, 2000, Bhattacharjee, 2004] that despite

How much time does it take to convect a magnetic field of the critical strength B_* into the dissipation region? This corresponds to the quiet time τ_q before an eruption during which Sweet-Parker reconnection is active but magnetic energy accumulates. Since the field outside of the dissipation region is frozen-in, τ_q is the time it takes for a field of strength B_* to be convected in by the inflow,

$$\tau_q = \int \frac{d\xi}{v_{in}}, \quad (6.2)$$

where ξ is the distance upstream from the X-line. This can be approximated using $v_{in} \sim c_{Aup}(\eta c^2/4\pi c_A L)^{1/2}$ from Eq. 2.20 and by assuming a linear profile in the magnetic field $B \simeq B_0\xi/W_s$, where W_s is the global magnetic shear length, the characteristic scale length over which coronal magnetic fields change their direction. At present, measuring W_s in the corona is not possible, though observations put an upper bound of 100 km [Dahlburg et al., 2005]. Integrating from $\xi \sim B_*W_s/B_0$ to approximately zero gives

$$\tau_q \sim 2W_s \sqrt{\frac{4\pi L}{\eta c^2 c_{A0}} \frac{B_*}{B_0}}, \quad (6.3)$$

where c_{A0} is the Alfvén speed based on B_0 . Using the values in Table 1.1, we find

$$\tau_q \simeq \left(\frac{W_s}{100 \text{ km}} \right) 1.2 \times 10^5 \text{ sec}, \quad (6.4)$$

The numerical factor is about 34 hours, which is a reasonable length of time for the accumulation of magnetic energy due to footpoint motion in the photosphere [Dahlburg et al., 2005]. Broader initial current layers would, of course, require a the incredibly small scale at which the Hall effect becomes important, it cannot be neglected in the solar corona.

longer time before onset. This provides an upper bound on the quiet time before an eruption (as any external forcing would only speed up the process), and it is of the order of hours or days, consistent with observations.

The time it takes for the transition from Sweet-Parker to Hall reconnection, corresponding to the time from onset until maximum flare signal, can be estimated as the convective time it takes for a Sweet-Parker dissipation region of thickness d_i to reach a thickness of the electron dissipation region of thickness $\sim d_e$. This time is δ/v_{in} , which at the transition time is the same as the resistive time across the sheet $(\eta c^2/4\pi\delta^2)^{-1}$ and the convective time along the sheet L/v_{out} . For the simulations described in Sec. 6.2, the resistive time is $\sim 400\Omega_{ci}^{-1}$, which compares reasonably well with the observed time of the transition (see Fig. 6.3d). For solar flare parameters, the resistive time across the sheet is approximately 11 sec, which is comparable to the onset times seen in flares [Priest and Forbes, 2002]. Therefore, these predicted observable parameters are quite consistent with observations in solar eruptions.

How does this model of the microphysics of reconnection fit in to leading models of the macrophysics of global magnetic fields before a solar eruption? Models of solar eruption onset generally fall into three main categories: sheared arcade [Mikic et al., 1988], catastrophic loss of equilibrium [Forbes and Isenberg, 1991], and magnetic breakout [Antiochos et al., 1999]. (See Refs. [Priest and Forbes, 2002] and [Lin et al., 2003] for recent reviews.) In sheared arcade models, velocity shear in the photosphere stretches a line-tied magnetic arcade, causing it to expand outward. A current sheet forms beneath it. If reconnection in the current sheet becomes fast, the arcade is ejected into interplanetary space. In catastrophic loss of equilibrium

models, a flux rope slowly emerges out of the photosphere and into the corona, forming a current sheet beneath it. The emergent flux rope is in quasi-steady MHD equilibrium until it reaches a critical height above the photosphere. At this point, it loses equilibrium and is ejected if the current sheet undergoes fast reconnection. In breakout models, a low lying arcade in a quadrupolar magnetic field configuration undergoes shear at its footpoints. As in the sheared arcade model, the low lying arcade expands outward. When it reaches the overlying magnetic field, it begins to reconnect. If the reconnection is fast, the arcade is ejected through the partially open magnetic field configuration.

In each of the three classes of models just described, simulations have shown that the eruption does not take place unless something causes fast reconnection to occur [Priest and Forbes, 2002, Lin et al., 2003]. In each model, the global dynamics creates a current sheet. As emphasized by Bhattacharjee and coworkers [Bhattacharjee et al., 1999] and reiterated here, when the current sheet gets to length scales thinner than the ion skin depth, non-magnetohydrodynamic effects become important. That an onset of Hall reconnection occurs at small scales complements the global models by giving the microphysical explanation of the fast reconnection onset. It would be interesting to incorporate the Hall effect into numerical simulations of these models of solar eruptions, but the large separation of length and time scales between Hall physics and the global dynamics makes such simulations extremely challenging.

6.4.2 Self-Organized Criticality Models of the Solar Corona

Much effort has been expended in the compilation and analysis of statistics of solar flares. It is hoped that an analysis of the statistics can provide insight into the underlying physics. Results of these studies show that many quantities, such as the peak photon count rate [Lin et al., 1984], the distribution of flares of a given size [Dennis, 1985], and the wait time between solar flares [Wheatland, 2000], have power law spectra over many orders of magnitude. (See Ref. [Charbonneau et al., 2001] for a recent review.) This suggests that the same mechanism is driving small and large magnetic energy release events.

Lu and Hamilton [Lu and Hamilton, 1991] pointed out that one would expect power laws if the solar corona was in a self-organized critical state. Self-organized criticality (SOC) [Bak et al., 1987] occurs when a system is self-driven to a critical state at which a catastrophe occurs, and the catastrophe induces transitions in nearby near-critical configurations, leading to avalanches and power law statistics. Many models of SOC in the corona exist [Charbonneau et al., 2001], but most are based on cellular automaton models with ad hoc critical conditions; a firm physical foundation describing the behavior is lacking.

The model for spontaneous onset described in Sec. 6.1 may potentially provide the physical mechanism. It was shown that reconnection is self-driven toward its critical state, in the sense that Sweet-Parker spontaneously evolves toward a thinner current layer as stronger magnetic field lines are convected into the dissipation region, where the catastrophic transition to Hall reconnection occurs. If it could be

shown that a transition to Hall reconnection at one location induces a transition in nearby Sweet-Parker reconnection sites, one could argue that the corona is in a self-organized critical state. Future work is required.

6.4.3 Onset of the Sawtooth Crash

As in the case of solar eruptions, we can calculate the critical magnetic field at which a Sweet-Parker dissipation region would reach the critical thickness for onset to occur, which for component reconnection in tokamaks is the ion Larmor radius ρ_s . Setting $\delta = \rho_s$ in Eq. 2.20, we find

$$B_* \sim \sqrt{4\pi m_i n} \left(\frac{\eta c^2}{4\pi \rho_s^2} L \right), \quad (6.5)$$

which, using the values from Table 1.1, gives $B_* \simeq 0.25$ G. Since the asymptotic magnetic field strength is $B_{up} \sim 100$ G, this critical field is much too small to give a viable onset mechanism for the sawtooth crash because the crash would start too easily.

This disagreement is not surprising, as the simple model presented here does not contain all of the relevant physics in a tokamak plasma. There are typically large density gradients near the core, so diamagnetic effects become important. Theory and simulations have shown [Rogers and Zakharov, 1995, Swisdak et al., 2003, Germaschewski et al., 2006] that diamagnetic effects tend to inhibit reconnection. A tokamak plasma undergoing Sweet-Parker reconnection with diamagnetic effects would have a smaller inflow for the same resistivity, leading a thicker dissipation region than the standard Sweet-Parker value. Thus, it would take a stronger mag-

netic field B_* to make δ_{SP} reduce to ρ_s . Thus, the inclusion of diamagnetic effects should improve agreement. This will be the subject of future studies.

6.4.4 Onset of Magnetic Substorms

It is important to emphasize that the model for catastrophic onset presented here does not seem to be applicable to reconnection in the Earth's magnetotail. As is shown in Table 1.2, the Sweet-Parker current sheet thickness begins much smaller than the ion skin depth d_i because the plasma is so rarefied. It is highly unlikely that a Sweet-Parker layer with thickness larger than d_i could exist. In other words, η' is so small for the magnetotail that the system is always less than the critical value for a the catastrophic disappearance of the Sweet-Parker solution.

6.5 Summary

In this chapter, we have explored the nature of the catastrophic onset of Hall reconnection by determining the conditions under which the onset occurs. In particular, we showed that the onset of fast magnetic reconnection can happen spontaneously, which is important for reconnection in remote places such as the solar corona. We also showed that predictions of the model are consistent with observations of eruptions in the solar corona, providing self-consistent quantitative estimates for the quiet time before an eruption and the onset time.

Chapter 7

Summary and Limitations

7.1 Summary of Results

In summary, magnetic reconnection is a physical process in which magnetic energy is converted into particle and flow energy. The change of topology of the magnetic field creates highly bent magnetic field lines which release their energy upon straightening, creating collimated outflow jets of plasma. By continuity, this outflow generates a flow which brings more field lines in, causing them to change their topology, as well. The process continues in a steady-state, releasing magnetic energy all the while. This process occurs in solar eruptions, magnetic substorms in the magnetosphere, and in sawtooth crashes in laboratory plasmas.

There are two independent steady-state configurations in which magnetic reconnection can exist, the (collisional) Sweet-Parker solution which is far too slow to explain the energy release rates observed in Nature, and the (collisionless) Hall reconnection solution, whose energy release rate is fast enough. One of the great outstanding questions about reconnection is why it is explosive, *i.e.*, why it onsets suddenly. To understand the Onset Problem, one needs more than identifying a trigger mechanism which sets reconnection off. One must also explain why the trigger is not set off during the time before an explosion when huge amounts of magnetic energy accumulate.

In this thesis, much has been learned about the dynamics of reconnection and how this impacts the Onset Problem. We summarize the results separately.

7.1.1 The Dynamics of Magnetic Reconnection

We studied the transition from Sweet-Parker to Hall reconnection (and vice versa) as the collisionality of the plasma varies. We found the interesting result that the changeover from collision-dominated to Hall-mediated reconnection is abrupt. In other words, collisional effects and the Hall effect cannot operate simultaneously; one effect or the other controls reconnection. In addition, the changeover from Sweet-Parker to Hall reconnection happens at a different critical resistivity than the changeover from Hall to Sweet-Parker reconnection. This is because the Hall effect is so large during Hall reconnection that it takes a much larger resistivity to dominate than during Sweet-Parker reconnection when the Hall effect is small. As a result, reconnection is bistable, meaning that either solution can occur for a given value of a control parameter, for a wide range of resistivities. Also, reconnection is history dependent, meaning that the solution the system takes depends on its history. This behavior was verified using resistive Hall-MHD numerical simulations.

Then, we developed a dynamical understanding of the bistable behavior of magnetic reconnection. We found that the abrupt disappearance of steady-state solutions can be described as saddle-node bifurcations as a control parameter $\eta' = \eta c^2 / 4\pi c_{Aup} d_i$ varies. Several additional properties of the bifurcation model were borne out by numerical simulations, including the existence of a heretofore uniden-

tified unstable steady-state reconnection solution.

Finally, we developed a theoretical model of the time evolution of the thickness of the dissipation region and showed that saddle-node bifurcations occur in the model as a result of the dispersive nature of the waves mediating the outflow of plasma away from the X-line. Linear and nonlinear properties of the model showed good agreement with numerical simulation results.

7.1.2 The Onset Problem of Magnetic Reconnection

That a saddle-node bifurcation catastrophically taking the Sweet-Parker solution out of existence underlies the dynamics of magnetic reconnection is potentially of profound importance to the Onset Problem. We have proposed that the onset of fast reconnection occurs due to a catastrophic transition from Sweet-Parker to Hall reconnection, the former being so slow that it is as if no reconnection is occurring at all. The bifurcation model provides a natural explanation for why the onset of Hall reconnection, required to explain the fast release of magnetic energy in observed eruptions, happens abruptly. Also, it explains how the system can accumulate energy for extended periods of time without fast reconnection beginning, since the system would begin in Sweet-Parker reconnection and the Hall solution would be accessible but inactive due to the history dependence of reconnection.

Lastly, we have studied the conditions under which the catastrophic onset of Hall reconnection occurs. We showed that a transition is induced by a decrease in the resistivity or an increase in the magnetic field strength immediately upstream of

the dissipation region. The latter effect occurs spontaneously due to the convection of stronger magnetic fields into the dissipation region during reconnection. The viability of this mechanism was verified by numerical simulations.

This model is potentially important for understanding magnetic explosions in Nature, in particular eruptions in the solar corona. We showed that predictions for magnetic field strengths, the quiet time time before a flare, and the onset time are consistent with observations. Applications to self-organized criticality models of the solar corona and the onset of the sawtooth crash were also discussed.

7.2 Limitations of the Model

There are some potentially important simplifying assumptions and limitations of the present model. One major limitation of the present model is that it is only two dimensional. Three dimensional turbulence has been correlated to fast reconnection in laboratory experiments [Ji et al., 2004]. However, simulations [Hesse et al., 2005] suggest that systems initially with three dimensional structure tend to relax into a quasi-two dimensional state, so three dimensional effects may not play a major role.

Secondly, we assumed a constant and uniform resistivity and temperature. It is possible that even two dimensional effects of turbulence could lead to a localized anomalous resistivity. If the onset of anomalous resistivity takes place before the current sheet reaches the critical thickness at which a transition to Hall reconnection occurs, then it would greatly affect our model. However, the generation of anomalous resistivity also requires thin current sheets.

Thirdly, diamagnetic effects have been shown to suppress the rate of reconnection and may impact the condition for onset for component reconnection. These effects are probably important for the onset of the sawtooth crash.

Chapter A

The Tearing Mode - A Primer

A.1 Physics of the Resistive Tearing Mode

The resistive tearing mode is an instability that occurs at oppositely directed magnetic field lines in the presence of a finite resistivity η , as developed by Furth, Killeen, and Rosenbluth [Furth et al., 1963]. Consider an equilibrium magnetic field with a component of the magnetic field that changes directions, $\mathbf{B}_0 = B_{x0}(y)\hat{\mathbf{x}}$, where $B_{x0}(0) = 0$ and $B_{x0}(y)$ is an odd function in y . Common examples are the Harris sheet [Harris, 1962] $B_{x0}(y) = B_0 \tanh(y/a)$ and the sine sheet $B_{x0}(y) = B_0 \sin(y/a)$, where a sets the width of the current layer in the y direction. Fig. A.1a shows a cut across the Harris sheet equilibrium with some representative magnetic field lines shown in Fig. A.1b.

Consider a small sinusoidal perturbation on \mathbf{B}_0 with x dependence and pointing in the y direction, $\mathbf{B}_1 = B_{y1} \sin(k_x x)\hat{\mathbf{y}}$. The resultant magnetic field lines are shown in Fig. A.1c for $B_{y1} = 0.1B_0$ and $k_x a = 1$. Away from the neutral line at $y = 0$, the perturbation merely bends the field lines, as shown by the lines marked B. However, close to the neutral line, a dramatic change has occurred, as shown by the field lines marked A. The topology of the magnetic field has changed into a so-called “island-structure”. Where once all field lines were open (stretching from one end of the domain to the other), now there are closed field lines (which intersect

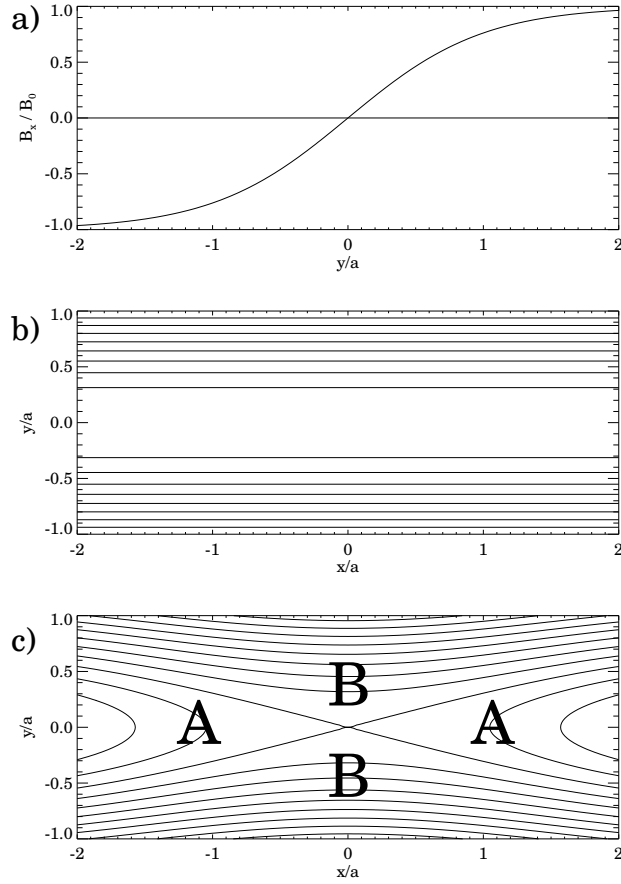


Figure A.1: (a) Harris sheet equilibrium, $B_{x0} = B_0 \tanh(y/a)$. (b) Magnetic field lines for the unperturbed Harris sheet, (c) Magnetic field lines for the perturbed Harris sheet, with $B_{y1} = 0.1B_0 \sin(k_x x)$, where $k_x a = 1$.

the same edge of the domain twice). The field line that separates closed field lines from open ones is called the “separatrix”.

Consider the magnetic tension forces in the perturbed configuration, which work to decrease the curvature of the field lines. For the closed field lines, the curvature force is directed into the island (or “O-line”) and away from the “X-line” at $(x, y) = (0, 0)$. For the open field lines, the curvature force is also into the island

and away from the X-line. The perturbation has set up an interesting battle. If the curvature force due to the open field lines is larger, the open field lines straighten out causing the island to become smaller; the perturbation decays and the system is stable. If the curvature force due to the closed field lines is larger, the field lines become rounder and the island becomes larger; the perturbation grows and the system is unstable. This is the tearing mode instability¹.

Analysis of the tearing mode begins with the equations of resistive-MHD, discussed in Sec. 2.2. We can take the flow to be incompressible (with constant and uniform density n_0) if the flows are much slower than the magnetosonic speed, as is the case when there is a large out of plane (guide) field. From Eqs. 2.42 and 2.43, the magnetic field \mathbf{B} and the bulk flow velocity \mathbf{v} evolve according to

$$\frac{\partial \mathbf{B}}{\partial t} = \nabla \times (\mathbf{v} \times \mathbf{B}) + \frac{\eta c^2}{4\pi} \nabla^2 \mathbf{B} \quad (\text{A.1})$$

$$m_i n_0 \left[\frac{\partial \mathbf{v}}{\partial t} + (\mathbf{v} \cdot \nabla) \mathbf{v} \right] = -\nabla \left(p + \frac{B^2}{8\pi} \right) + \frac{1}{4\pi} (\mathbf{B} \cdot \nabla) \mathbf{B} \quad (\text{A.2})$$

where $\nabla \cdot \mathbf{v} = 0$ because of incompressibility and $\nabla \cdot \mathbf{B} = 0$.

To perform a linear analysis, we need an equilibrium magnetic field. Suppose $B_{x0}(y)$ is a known magnetic field profile. The guide field $B_{z0}(y)$ must satisfy $B_{z0}(y) = \sqrt{B_T^2 - B_{x0}^2(y)}$ where B_T is a constant, so the total initial pressure is uniform. Using a stationary plasma ($\mathbf{v}_0 = 0$) and an equilibrium magnetic field of

$$\mathbf{B}_0 = B_{x0}(y)\hat{\mathbf{x}} + B_{z0}(y)\hat{\mathbf{z}}. \quad (\text{A.3})$$

¹Alternately, one can think of the tearing mode in terms of energies. Bending the open field lines costs energy, but the straightening of closed field lines releases it. If the closed field lines release more energy than bending the open field lines cost, then the perturbation has decreased the system's potential energy, which is the standard criterion for a linear instability.

with perturbed quantities \mathbf{B}_1 and \mathbf{v}_1 in Eqs. A.1 and A.2 and ignoring terms of second order smallness in the perturbations gives

$$\frac{\partial \mathbf{B}_1}{\partial t} = (\mathbf{B}_0 \cdot \nabla) \mathbf{v}_1 - (\mathbf{v}_1 \cdot \nabla) \mathbf{B}_0 + \frac{\eta c^2}{4\pi} \nabla^2 \mathbf{B}_1 \quad (\text{A.4})$$

$$m_i n_0 \frac{\partial \mathbf{v}_1}{\partial t} = -\frac{1}{4\pi} \nabla (\mathbf{B}_0 \cdot \mathbf{B}_1) + \frac{1}{4\pi} (\mathbf{B}_1 \cdot \nabla) \mathbf{B}_0 + \frac{1}{4\pi} (\mathbf{B}_0 \cdot \nabla) \mathbf{B}_1. \quad (\text{A.5})$$

Taking two curls of Eq. A.5 and using the form of \mathbf{B}_0 in Eq. A.3, we find the remarkable property that the equations for the y components of the two perturbed quantities decouple from the other quantities, leaving

$$\frac{\partial B_{y1}}{\partial t} = (\mathbf{B}_0 \cdot \nabla) v_{y1} + \frac{\eta c^2}{4\pi} \nabla^2 B_{y1} \quad (\text{A.6})$$

$$m_i n_0 \frac{\partial}{\partial t} \nabla^2 v_{y1} = \frac{1}{4\pi} \left[(\mathbf{B}_0 \cdot \nabla) \nabla^2 B_{y1} - \left(\frac{d^2 \mathbf{B}_0}{dy^2} \cdot \nabla \right) B_{y1} \right]. \quad (\text{A.7})$$

Notice that if the $d^2 \mathbf{B}_0 / dy^2$ term vanishes (and the η term is neglected), Eqs. A.6 and A.7 reduce to Eqs. 2.47 and 2.48, those for the Alfvén wave, which is stable. Also, since η is exceedingly small for plasmas of interest, it can usually be neglected, but from Eq. A.6 it cannot be neglected where $\mathbf{B}_0 \cdot \nabla v_{y1}$, or where $\mathbf{k} \cdot \mathbf{B}_0$ in Fourier space, goes to zero.

It is instructive to form an energy integral from these equations. Consider modes with no z dependence. Multiplying Eq. A.7 by v_{y1} and integrating over all space, one finds after some algebra that

$$\begin{aligned} \frac{\partial}{\partial t} \int d^3x \left[\frac{1}{2} m_i n_0 (\nabla v_{y1} \cdot \nabla v_{y1}) + \frac{1}{8\pi} (\nabla B_{y1} \cdot \nabla B_{y1}) + \frac{1}{8\pi} \frac{B''_{x0}}{B_{x0}} B_{y1}^2 \right] = \\ - \frac{1}{4\pi} \frac{\eta c^2}{4\pi} \int d^3x \left[\nabla^2 B_{y1} \nabla^2 B_{y1} - \frac{B''_{x0}}{B_{x0}} B_{y1} \nabla^2 B_{y1} \right] \end{aligned} \quad (\text{A.8})$$

where we used Eq. A.6 and defined the shorthand $B''_{x0} = d^2 B_{x0} / dy^2$. The first term on the left hand side plays the role of the kinetic energy of the perturbation. The

other two terms on the left hand side play the role of the potential energy due to the perturbation δW_B ,

$$\delta W_B = \int d^3x \left[\frac{1}{8\pi} (\nabla B_{y1} \cdot \nabla B_{y1}) + \frac{1}{8\pi} \frac{B''_{x0}}{B_{x0}} B_{y1}^2 \right]. \quad (\text{A.9})$$

The first term is positive definite, so it always contributes a positive amount to the energy change; it is stabilizing. However, the second term can be negative, and if its contribution is larger than the first term, then the perturbation has decreased the potential energy, and an instability will occur. Thus, the $d^2 B_{x0}/dy^2$ term drives the instability². Physically, large current gradients drive the tearing mode instability. The magnetic energy due to the perturbation is so important that it is given a special name, the “stability parameter” Δ' , with the following normalization

$$\Delta' = - \left(\frac{8\pi}{\int dx dz [B_{y1}(y=0)]^2} \right) \delta W_B. \quad (\text{A.10})$$

(The dimension of Δ' is inverse length; the reason for this choice of normalization will become clearer later.) If $\Delta' > 0$, the energy perturbation is negative and the system is unstable, if $\Delta' < 0$, the energy perturbation is positive and the system is stable.

There is another important interpretation of Δ' . Far from $y = 0$, the dynamics is controlled mostly by the magnetic field. Neglecting the inertia term in Eq. A.7 and lifting an x derivative gives

$$\nabla^2 B_{y1} = \frac{B''_{x0}}{B_{x0}} B_{y1}. \quad (\text{A.11})$$

²This is reminiscent of Rayleigh’s criterion for fluid instability being that the velocity profile has an inflection point.

Multiplying this by B_{y1} , integrating over the half space $y > 0$, and using a vector identity gives

$$\int_{y>0} d^3x \nabla \cdot (B_{y1} \nabla B_{y1}) = \int_{y>0} d^3x \left[\nabla B_{y1} \cdot \nabla B_{y1} + \frac{B''_{x0}}{B_{x0}} B_{y1}^2 \right]. \quad (\text{A.12})$$

Using Gauss' theorem and noting that B_{y1} must vanish at infinity, this reduces to

$$- \int dxdz \left[B_{y1} \frac{\partial B_{y1}}{\partial y} \right]_{y=0^+} = \int_{y>0} d^3x \left[\nabla B_{y1} \cdot \nabla B_{y1} + \frac{B''_{x0}}{B_{x0}} B_{y1}^2 \right]. \quad (\text{A.13})$$

where $y = 0^+$ means that the term in brackets is evaluated in the limit of $y \rightarrow 0$ coming from positive y . Performing the same analysis for the half space $y < 0$ gives a similar relation:

$$\int dxdz \left[B_{y1} \frac{\partial B_{y1}}{\partial y} \right]_{y=0^-} = \int_{y<0} d^3x \left[\nabla B_{y1} \cdot \nabla B_{y1} + \frac{B''_{x0}}{B_{x0}} B_{y1}^2 \right]. \quad (\text{A.14})$$

Adding the two results and identifying the right hand side with δW_B from Eq. A.9 gives

$$\int dxdz B_{y1}(y=0) \left\{ \left[\frac{\partial B_{y1}}{\partial y} \right]_{y=0^-} - \left[\frac{\partial B_{y1}}{\partial y} \right]_{y=0^+} \right\} = 8\pi \delta W_B. \quad (\text{A.15})$$

where we used $B_{y1}(y=0^+) = B_{y1}(y=0^-) \equiv B_{y1}(y=0)$ because B_{y1} must be continuous. While B_{y1} is continuous, this relation shows that it is not smooth; the first derivative has a non-zero jump across $y=0$. Dividing both sides by $\int dxdz [B_{y1}(y=0)]^2$ and using the definition of Δ' from Eq. A.10 gives

$$\Delta' = \frac{1}{\int dxdz [B_{y1}(y=0)]^2} \times \int dxdz [B_{y1}(y=0)]^2 \left\{ \left[\frac{1}{B_{y1}} \frac{\partial B_{y1}}{\partial y} \right]_{y=0^+} - \left[\frac{1}{B_{y1}} \frac{\partial B_{y1}}{\partial y} \right]_{y=0^-} \right\}. \quad (\text{A.16})$$

Thus, Δ' is also a measure of the jump in the logarithmic derivative of B_{y1} across the $y=0$ surface when averaged in a particular way. The larger Δ' , the larger

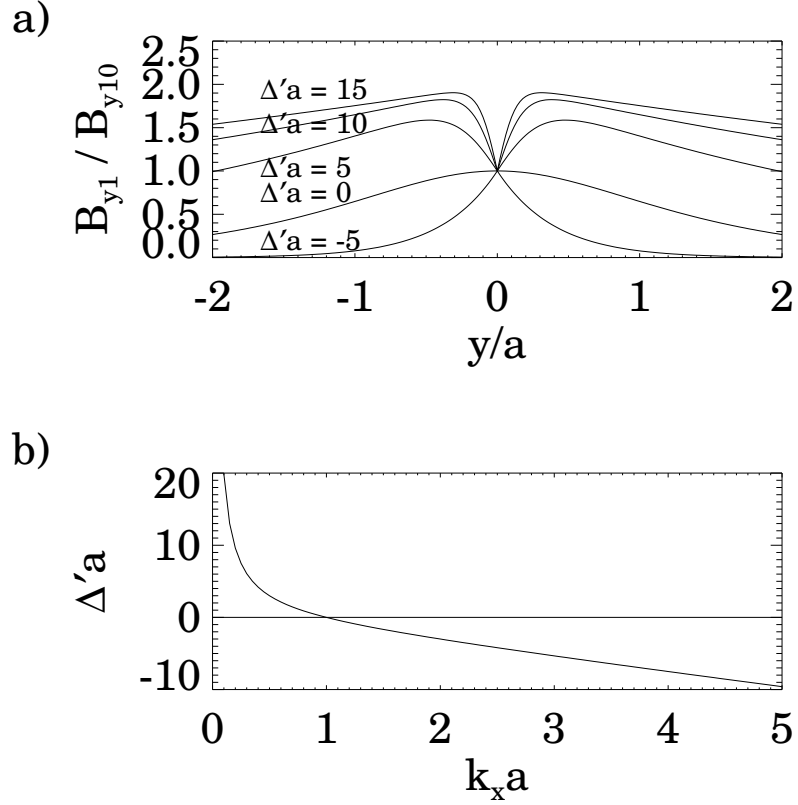


Figure A.2: Outer solution for the magnetic field perturbation for the linear tearing mode problem for a Harris sheet equilibrium for $\Delta' = -5, 0, 5, 10,$ and 15 .

the kink in B_{y1} across the $y = 0$ surface. As an example, for the Harris sheet $B_{x0}(y) = B_0 \tanh(y/a)$ pictured in Fig. A.1a, the exact solution of Eq. A.11 is given by $B_{y1}(y) = B_{y10} \exp(-k|y|)[1 + (1/ka) \tanh(|y|/a)]$, and is plotted in Fig. A.2a for $\Delta'a = -5, 0, 5, 10,$ and 15 . One can see that the kink is larger for larger Δ' . The system is unstable when the kink is positive.

It should be emphasized that Δ' , and therefore the stability of a particular equilibrium, is found for a given equilibrium field $B_{x0}(y)$ and wavenumber k_x of

the perturbation by using Eq. A.11 to solve for B_{y1} , allowing a kink at $y = 0$. In particular, the stability is *not* influenced by the size of the resistivity (although the growth rate is). The stability parameter Δ' is only a function of k_x and a , the sheared field length scale in the y direction of the equilibrium configuration.

Under what conditions is the tearing mode unstable, *i.e.*, for what combination of k_x and a is Δ' positive? Doing a scaling analysis on Eq. A.9 with $\nabla \sim k_x$ and $d^2/dy^2 \sim -1/a^2$, we find instability occurs when

$$k_x a \lesssim 1. \quad (\text{A.17})$$

Thus, in general, small wavenumber (long wavelength) modes are unstable. Physically, this is because short wavelength modes produce much more bending of the open field lines, which stabilizes the mode. For the Harris sheet equilibrium, the exact solution for $\Delta'(k_x, a) = (2/a)(1/k_x a - k_x a)$ is plotted in Fig. A.2b.

Finally, we discuss a useful tool for describing various tearing mode properties, the flux function ψ . In complete generality, the magnetic field can be written as the curl of a vector potential \mathbf{A} . In two dimensions with $\partial/\partial z = 0$, the x and y components of the magnetic field simplify to

$$B_x = \frac{\partial A_z}{\partial y} \quad \text{and} \quad B_y = -\frac{\partial A_z}{\partial x}. \quad (\text{A.18})$$

This can be written as

$$\mathbf{B}_\perp = \hat{\mathbf{z}} \times \nabla \psi \quad (\text{A.19})$$

where \mathbf{B}_\perp is the x and y components of \mathbf{B} and, for historical reasons, A_z is renamed as $-\psi$. The function ψ has many important characteristics. First, $\mathbf{B}_\perp \cdot \nabla \psi = 0$, so

lines of constant ψ are coincident with the magnetic field lines in the plane. Second, near the $y = 0$ surface, we can approximate $B_{x0} \simeq B'y$ and $B_{y1} = B_1 \sin(k_x x)$, so ψ can be written as

$$\psi = -\frac{1}{2}B'y^2 - \frac{B_1}{k_x} \cos(k_x x). \quad (\text{A.20})$$

Expanding this function near $x = 0$ gives $\psi \simeq -B'y^2/2 + B_1 k_x x^2/2$, which is the equation of a hyperbola, forming an X-shaped structure. A surface plot of ψ has a saddle point at the X-line. Expanding ψ near $x = \pi/k_x$ gives $\psi \simeq -B'y^2/2 - B_1 k_x x^2/2$, which is the equation of an ellipse, forming an O-shaped structure. A surface plot of ψ has a maximum or minimum at the O-line. In addition, since the magnetic field lines are lines of constant ψ , Eq. A.20 allows the width of the island to be computed. At the X-line, $\psi(0, 0) = -B_1/k_x$. The half-width of the island is the height $y = w$ above the O-point (where $x = \pi/k_x$) where ψ has the same value as at the X-line. Since $\psi(\pi/k_x, w) = -B'w^2/2 + B_1/k_x$, setting $\psi(0, 0) = \psi(\pi/k_x, w)$ gives

$$w = \sqrt{\frac{4B_1}{k_x B'}}. \quad (\text{A.21})$$

Finally, the magnetic flux $\Phi = \int \mathbf{B} \cdot d\mathbf{S}$ through the $y = 0$ plane is related to ψ . Using Eq. A.19, $\Phi = -\int dz\psi$, so ψ is (the negative of) the flux through the plane per unit length.

This concludes our discussion of the tearing mode. More thorough sources which, for example, evaluate the growth rate of the tearing mode, exist, such as Refs. [Drake, 1985, White, 1986, Biskamp, 1993]. An excellent starting point is Ref. [Goldston and Rutherford, 1995].

Bibliography

- [Antiochos et al., 1999] Antiochos, S. K., DeVore, C. R., and Klimchuk, J. A. (1999). A model for solar coronal mass ejections. *Astrophys. J.*, 510:485.
- [Asano et al., 2003] Asano, Y., Mukai, T., Hoshino, M., Saito, Y., Hayakawa, H., and Nagai, T. (doi:10.1029/2002JA009785, 2003). Evolution of the thin current sheet in a substorm observed by geotail. *J. Geophys. Res.*, 108(A5):1189.
- [Aschwanden, 2005] Aschwanden, M. (2005). *Physics of the Solar Corona*. Springer.
- [Axford, 1984] Axford, W. I. (1984). Magnetic field reconnection. In Edward W. Hones, J., editor, *Magnetic Reconnection in Space and Laboratory Plasmas*, Geophysical Monograph 30, pages 1–8. American Geophysical Union.
- [Aydemir, 1992] Aydemir, A. Y. (1992). Nonlinear studies of $m = 1$ modes in high-temperature plasmas. *Phys. Fluids B*, 4(11):3469–3472.
- [Bak et al., 1987] Bak, P., Tang, C., and Wiesenfeld, K. (1987). Self-organized criticality: An explanation of $1 / f$ noise. *Phys. Rev. Lett.*, 59(4):381–384.
- [Bhattacharjee, 2004] Bhattacharjee, A. (2004). Impulsive magnetic reconnection in the earth’s magnetotail and the solar corona. *Annu. Rev. Astron. Astrophys.*, 42:365–84.
- [Bhattacharjee et al., 2005] Bhattacharjee, A., Germaschewski, K., and Ng, C. S. (2005). Current singularities: Drivers of impulsive reconnection. *Phys. Plasmas*, 12:042305.
- [Bhattacharjee et al., 1999] Bhattacharjee, A., Ma, Z. W., and Wang, X. (1999). Impulsive reconnection dynamics in collisionless laboratory and space plasmas. *J. Geophys. Res.*, 104(A7):14,543–14,556.
- [Birn et al., 2001] Birn, J., Drake, J. F., Shay, M. A., Rogers, B. N., Denton, R. E., Hesse, M., Kuznetsova, M., Ma, Z. W., Bhattacharjee, A., Otto, A., and Pritchett, P. L. (2001). GEM magnetic reconnection challenge. *J. Geophys. Res.*, 106:3715.
- [Biskamp, 1986] Biskamp, D. (1986). Magnetic reconnection via current sheets. *Phys. Fluids*, 29:1520.
- [Biskamp, 1993] Biskamp, D. (1993). *Nonlinear Magnetohydrodynamics*. Cambridge University Press.
- [Biskamp, 2000] Biskamp, D. (2000). *Magnetic Reconnection in Plasmas*. Cambridge University Press, Cambridge, UK.
- [Biskamp et al., 1995] Biskamp, D., Schwarz, E., and Drake, J. F. (1995). Ion-controlled collisionless magnetic reconnection. *Phys. Rev. Lett.*, 75(21):3850.

- [Carrington, 1859] Carrington, R. C. (1859). Description of a singular appearance seen in the sun on september 1, 1859. *MNRAS*, 20:13–15.
- [Cassak et al., 2006a] Cassak, P. A., Drake, J. F., and Shay, M. A. (2006a). Catastrophic onset of fast magnetic reconnection with a guide field. *in preparation*.
- [Cassak et al., 2006b] Cassak, P. A., Drake, J. F., and Shay, M. A. (2006b). A model for spontaneous onset of fast magnetic reconnection. *Ap. J.*, 644:L145–L148.
- [Cassak et al., 2006c] Cassak, P. A., Drake, J. F., Shay, M. A., and Eckhardt, B. (2006c). Bifurcation model for the catastrophic onset of magnetic reconnection. *in preparation*.
- [Cassak et al., 2005] Cassak, P. A., Shay, M. A., and Drake, J. F. (2005). Catastrophe model for fast magnetic reconnection onset. *Phys. Rev. Lett.*, 95:235002.
- [Charbonneau et al., 2001] Charbonneau, P., McIntosh, S. W., Liu, H.-L., and Bogdan, T. J. (2001). Avalanche models for solar flares. *Solar Phys.*, 203:321–353.
- [Chen, 1974] Chen, F. F. (1974). *Introduction to Plasma Physics*. Plenum Press.
- [Choudhuri, 1998] Choudhuri, A. R. (1998). *The Physics of Fluids and Plasmas*. Cambridge University Press.
- [Cothran et al., 2005] Cothran, C. D., Landreman, M., Brown, M. R., and Matthaeus, W. H. (2005). Generalized ohm’s law in a 3-d reconnection experiment. *Geophys. Res. Lett.*, 32(5):L03105, doi:10.1029/2004GL021245.
- [Cowley, 2006] Cowley, S. (2006). Frozen field lines and diffusion. Lecture notes, CMPD & CMSO Winter School.
- [Dahlburg et al., 2005] Dahlburg, R. B., Klimchuk, J. A., and Antiochos, S. K. (2005). An explanation for the “switch-on” nature of magnetic energy release and its application to coronal heating. *Ap. J.*, 622:1191–1201.
- [Daughton et al., 2006] Daughton, W., Scudder, J., and Karimabadi, H. (2006). Fully kinetic simulations of undriven magnetic reconnection with open boundary conditions. *Phys. Plasmas*, 13:072101.
- [Dennis, 1985] Dennis, B. R. (1985). Solar hard x-ray bursts. *Solar Phys.*, 100:465–90.
- [Drake, 1985] Drake, J. F. (1985). Reconnection in sheared magnetic fields in space and astrophysics. In Kundu, M. R. and Holman, G. D., editors, *Unstable current systems and plasma instabilities in astrophysics*, pages 61–81. D. Reidel Publishing Co.

- [Drake, 1995] Drake, J. F. (1995). Magnetic reconnection: a kinetic treatment. In Sonnerup, B. U. Ö., Song, P., and Thomsen, M., editors, *Physics of the Magnetopause*, volume 90 of *Geophysical Monograph*, page 155. American Geophysical Union.
- [Drake and Lee, 1977] Drake, J. F. and Lee, Y. C. (1977). Kinetic theory of tearing instabilities. *Phys. Fluids*, 20(8):1341.
- [Drake and Shay, 2006] Drake, J. F. and Shay, M. A. (expected 2006). The fundamentals of collisionless reconnection. In Birn, J. and Priest, E., editors, *Reconnection of Magnetic Fields: Magnetohydrodynamics and Collisionless Theory and Observations*. Cambridge University Press.
- [Drake et al., 2003] Drake, J. F., Swisdak, M., Shay, M. A., Rogers, B. N., Zeiler, A., and Cattell, C. (2003). Formation of electron holes and particle energization during magnetic reconnection. *Science*, 299:873.
- [Duncan and Thompson, 1992] Duncan, R. C. and Thompson, C. (1992). Formation of very strongly magnetized neutron stars: implications for gamma-ray bursts. *Ap. J.*, 392:L9–L13.
- [Dungey, 1953] Dungey, J. W. (1953). Conditions for the occurrence of electrical discharges in astrophysical systems. *Phil. Mag.*, 44:725.
- [Dungey, 1958] Dungey, J. W. (1958). *Cosmic Electrodynamics*. Cambridge University Press.
- [Dungey, 1961] Dungey, J. W. (1961). Interplanetary magnetic field and the auroral zones. *Phys. Rev. Lett.*, 6:47.
- [Edwards et al., 1986] Edwards, A. W., Campbell, D. J., Engelhardt, W. W., Farhabach, H. U., Gill, R. D., Granetz, R. S., Tsuji, S., Tubbing, B. J. D., Weller, A., Wesson, J., and Zaslowski, D. (1986). Rapid collapse of a plasma sawtooth oscillation in the jet tokamak. *Phys. Rev. Lett.*, 57:210–213.
- [Egedal et al., 2006] Egedal, J., Fox, W., Katz, N., and Porkolab, M. (2006). Experimental observations of spontaneous magnetic reconnection. *submitted to Phys. Rev. Lett.*
- [Fitzpatrick, 2004] Fitzpatrick, R. (2004). Scaling of forced magnetic reconnection in the Hall-magnetohydrodynamic Taylor problem. *Phys. Plasmas*, 11(3):937.
- [Forbes and Isenberg, 1991] Forbes, T. G. and Isenberg, P. A. (1991). A catastrophe mechanism for coronal mass ejections. *Astrophys. J.*, 373(1):294–307.
- [Furno et al., 2005] Furno, I., Intrator, T. P., Hemsing, E. W., Hsu, S. C., Abbate, S., Ricci, P., and Lapenta, G. (2005). Coalescence of two magnetic flux ropes via collisional magnetic reconnection. *Phys. Plasmas*, 12:055702.

- [Furth et al., 1963] Furth, H. P., Killeen, J., and Rosenbluth, M. N. (1963). Finite-resistivity instabilities of a sheet pinch. *Phys. Fluids*, 6(4):459.
- [Germaschewski et al., 2006] Germaschewski, K., Bhattacharjee, A., Ng, C. S., Wang, X., and Chacon, L. (2006). Compressible resistive and hall mhd dynamics of the m=1 sawtooth instability. In *Bull. Am. Phys. Soc.*, volume 51, page 312.
- [Giovanelli, 1947] Giovanelli, R. G. (1947). Magnetic and electric phenomena in the sun's atmosphere associated with sunspots. *MNRAS*, 107(4):338–355.
- [Goldston and Rutherford, 1995] Goldston, R. J. and Rutherford, P. H. (1995). *Introduction to Plasma Physics*. Institute of Physics Publishing.
- [Grasso et al., 1999] Grasso, D., Pegoraro, F., Porcelli, F., and Califano, F. (1999). Hamiltonian magnetic reconnection. *Plasma Phys. Control. Fusion*, 41:1497–1515.
- [Griffiths, 1998] Griffiths, D. J. (1998). *Introduction to Electrodynamics*. Prentice Hall.
- [Guzdar et al., 1993] Guzdar, P. N., Drake, J. F., McCarthy, D., Hassam, A. B., and Liu, C. S. (1993). Three-dimensional fluid simulations of the nonlinear drift-resistive ballooning modes in tokamak edge plasmas. *Phys. Fluids B*, 5(10):3712–3727.
- [Harris, 1962] Harris, E. G. (1962). On a plasma sheath separating regions of oppositely directed magnetic field. *Nuovo Cimento*, 23:115.
- [Hassam, 1984] Hassam, A. B. (1984). Collisional tearing in field-reversed configurations. *Phys. Fluids*, 27:2877.
- [Hesse et al., 2001] Hesse, M., Birn, J., and Kuznetsova, M. (2001). Collisionless magnetic reconnection: Electron processes and transport modeling. *J. Geophys. Res.*, 106(A3):3721–3735.
- [Hesse et al., 2004] Hesse, M., Kuznetsova, M., and Birn, J. (2004). The role of electron heat flux in guide-field magnetic reconnection. *Phys. Plasmas*, 11(12):5387–5397.
- [Hesse et al., 2002] Hesse, M., Kuznetsova, M., and Hoshino, M. (2002). The structure of the dissipation region for component reconnection: Particle simulations. *Geophys. Res. Lett.*, 29:1563.
- [Hesse et al., 2005] Hesse, M., Kuznetsova, M., Schindler, K., and Birn, J. (2005). Three-dimensional modeling of electron quasiviscous dissipation in guide-field magnetic reconnection. *Phys. Plasmas*, 12(100704).
- [Hesse et al., 1999] Hesse, M., Schindler, K., Birn, J., and Kuznetsova, M. (1999). The diffusion region in collisionless magnetic reconnection. *Phys. Plasmas*, 6(5):1781.

- [Hodgson, 1859] Hodgson, R. (1859). On a curious appearance seen in the sun. *MNRAS*, 20:15–16.
- [Horiuchi and Sato, 1994] Horiuchi, R. and Sato, T. (1994). Particle simulation study of driven magnetic reconnection in a collisionless plasma. *Phys. Plasmas*, 1(11):3587.
- [Horiuchi and Sato, 1997] Horiuchi, R. and Sato, T. (1997). Particle simulation study of collisionless driven reconnection in a sheared magnetic field. *Phys. Plasmas*, 4(2):277–289.
- [Hoshino et al., 2001] Hoshino, M., Mukai, T., Terasawa, T., and Shinohara, I. (2001). Suprathermal electron acceleration in magnetic reconnection. *J. Geophys. Res.*, 106:25979.
- [Hoyle, 1949] Hoyle, F. (1949). *Some Recent Researches in Solar Physics*. Cambridge University Press.
- [Huba, 1995] Huba, J. D. (1995). Hall magnetohydrodynamics in space and laboratory plasmas. *Phys. Plasmas*, 2(6):2504–2513.
- [Huba, 2005] Huba, J. D. (2005). Hall magnetic reconnection: Guide field dependence. *Phys. Plasmas*, 12:012322.
- [Huba et al., 1977] Huba, J. D., Gladd, N. T., and Papadopoulos, K. (1977). The lower-hybrid-drift instability as a source of anomalous resistivity for magnetic field reconnection. *Geophys. Res. Lett.*, 4:125.
- [Huba and Rudakov, 2004] Huba, J. D. and Rudakov, L. I. (2004). Hall magnetic reconnection rate. *Phys. Rev. Lett.*, 93:175003.
- [Jemella et al., 2004] Jemella, B. D., Drake, J. F., and Shay, M. A. (2004). Singular structure of magnetic islands resulting from reconnection. *Phys. Plasmas*, 11(12):5668–5672.
- [Jemella et al., 2003] Jemella, B. D., Shay, M. A., Drake, J. F., and Rogers, B. N. (2003). Impact of frustrated singularities on magnetic island evolution. *Phys. Rev. Lett.*, 91(12):125002.
- [Ji et al., 2004] Ji, H., Terry, S., Yamada, M., Kulsrud, R., Kuritsyn, A., and Ren, Y. (2004). Electromagnetic fluctuations during fast reconnection in a laboratory plasma. *Phys. Rev. Lett.*, 92(11):115001.
- [Kadomtsev, 1975] Kadomtsev, B. B. (1975). Disruptive instability in tokamaks. *Sov. J. Plasma Phys.*, 1:389–391.
- [Kivelson and Russell, 1995] Kivelson, M. G. and Russell, C. T., editors (1995). *Introduction to Space Physics*. Cambridge University Press.

- [Kleva et al., 1995] Kleva, R., Drake, J., and Waelbroeck, F. (1995). Fast reconnection in high temperature plasma. *Phys. Plasma*, 2:23.
- [Klimchuk, 2006] Klimchuk, J. A. (2006). On solving the coronal heating problem. *Solar Phys.*, 234:41–77.
- [Knoll and Chacon, 2006] Knoll, D. A. and Chacon, L. (2006). Coalescence of magnetic islands in the low resistivity, hall mhd, regime. *Phys. Rev. Lett.*, 96(13):135001.
- [Krall and Trivelpiece, 1973] Krall, N. A. and Trivelpiece, A. W. (1973). *Principles of Plasma Physics*. McGraw-Hill.
- [Kuznetsova et al., 2001] Kuznetsova, M. M., Hesse, M., and Winske, D. (2001). Collisionless reconnection supported by nongyrotropic pressure effects in hybrid and particle simulations. *J. Geophys. Res.*, 106(A3):3799.
- [Lazarus et al., 2006] Lazarus, E. A., Waelbroeck, F. L., Luce, T. C., Austin, M. E., Burrell, K. H., Ferron, J. R., Hyatt, A. W., Osborne, T. H., Chu, M. S., Brennan, D. P., Gohil, P., Groebner, R. J., Hsieh, C. L., Jayakumar, R. J., Lao, L. L., Lohr, J., Makowski, M. A., Petty, C. C., Politzer, P. A., Prater, R., Rhodes, T. L., Scoville, J. T., Strait, E. J., Turnbull, A. D., Wade, M. R., Wang, G., Reimerdes, H., and Zhang, C. (2006). A comparison of sawtooth oscillations in bean and oval shaped plasmas. *Plasma Phys. Control. Fusion*, 48:L65–L72.
- [Lin et al., 2003] Lin, J., Soon, W., and Baliunas, S. L. (2003). Theories of solar eruptions: a review. *New Astron. Rev.*, 47:53–84.
- [Lin et al., 1984] Lin, R. P., Schwartz, R. A., Kane, S. R., Pelling, R. M., and Hurley, K. C. (1984). Solar hard x-ray microflares. *Ap. J.*, 283:421–425.
- [Longcope et al., 2005] Longcope, D. W., McKenzie, D. E., Cirtain, J., and Scott, J. (2005). Observations of separator reconnection to an emerging active region. *Ap. J.*, 630:596.
- [Lu and Hamilton, 1991] Lu, E. T. and Hamilton, R. J. (1991). Avalanches and the distribution of solar flares. *Ap. J.*, 380:L89–L92.
- [Ma and Bhattacharjee, 1996] Ma, Z. W. and Bhattacharjee, A. (1996). Fast impulsive reconnection and current sheet intensification due to electron pressure gradients in semi-collisional plasmas. *Geophys. Res. Lett.*, 23:1673.
- [Mandt et al., 1994] Mandt, M. E., Denton, R. E., and Drake, J. F. (1994). Transition to whistler mediated magnetic reconnection. *Geophys. Res. Lett.*, 21:73.
- [McPherron, 1999] McPherron, R. L. (1999). “What are they arguing about” SUBSTORMS! GEM Workshop, Student Tutorial, <http://www-ssc.igpp.ucla.edu/gem/tutorial/index.html>.

- [Mikic et al., 1988] Mikic, Z., Barnes, D. C., and Schnack, D. D. (1988). Dynamical evolution of a solar coronal magnetic field arcade. *Astrophys. J.*, 328:830–847.
- [Miller et al., 1997] Miller, J. A., Cargill, P. J., Emslie, A. G., Holman, G. D., Dennis, B. R., LaRosa, T. N., Winglee, R. M., Benka, S. G., and Tsuneta, S. (1997). Critical issues for understanding particle acceleration in impulsive solar flares. *J. Geophys. Res.*, 102:14631.
- [Mishin et al., 1997] Mishin, V. M., Block, L. P., Bazarzhapov, A. D., Saifudinova, T. I., Lunyushkin, S. B., Shirapov, D. S., Woch, J., Eliasson, L., Marklund, G. T., Blomberg, L. G., and Opgenoorth, H. (1997). A study of the cdaw 9c substorm of may 3, 1986, using magnetogram inversion technique 2, and a substorm scenario with two active phases. *J. Geophys. Res.*, 102(A9):19,845–19,859.
- [Mitchell et al., 1990] Mitchell, D. G., Williams, D. J., Huang, C. Y., Frank, L. A., and Russell, C. T. (1990). Current carriers in the near-earth cross-tail current sheet during substorm growth phase. *Geophys. Res. Lett.*, 17:583.
- [Mozer et al., 2002] Mozer, F., Bale, S. D., and Phan, T. D. (2002). Evidence of diffusion regions in a subsolar magnetopause crossing. *Phys. Rev. Lett.*, 89:015002.
- [Øieroset et al., 2001] Øieroset, M., Phan, T. D., Fujimoto, M., Lin, R. P., and Lepping, R. P. (2001). In situ detection of collisionless reconnection in the earth’s magnetotail. *Nature*, 412:417.
- [Parker, 1957] Parker, E. N. (1957). Sweet’s mechanism for merging magnetic fields in conducting fluids. *J. Geophys. Res.*, 62:509.
- [Parker, 1963] Parker, E. N. (1963). The solar-flare phenomenon and the theory of reconnection and annihilation of magnetic fields. *Ap. J.*, 8:177.
- [Parker, 1983] Parker, E. N. (1983). Magnetic neutral sheets in evolving fields. ii. formation of the solar corona. *Ap. J.*, 264:642–647.
- [Parker, 1988] Parker, E. N. (1988). Nanoflares and the solar x-ray corona. *Ap. J.*, 330:474–479. July.
- [Petschek, 1964] Petschek, H. E. (1964). Magnetic field annihilation. In Ness, W. N., editor, *AAS/NASA Symposium on the Physics of Solar Flares*, page 425. NASA, Washington, DC.
- [Phan et al., 2006] Phan, T. D., Gosling, J. T., Davis, M. S., Skoug, R. M., Oieroset, M., Lin, R. P., Lepping, R. P., McComas, D. J., Smith, C. W., Reme, H., and Balogh, A. (2006). A magnetic reconnection x-line extending more than 390 earth radii in the solar wind. *Nature*, 439:175.
- [Porcelli et al., 2002] Porcelli, F., Borgogno, D., Califano, F., Grasso, D., Ottaviani, M., and Pegoraro, F. (2002). Recent advances in collisionless magnetic reconnection. *Plasma Phys. Control. Fusion*, 44:B389–B405.

- [Priest and Forbes, 2000] Priest, E. and Forbes, T. (2000). *Magnetic Reconnection*. Cambridge University Press.
- [Priest and Forbes, 2002] Priest, E. R. and Forbes, T. R. (2002). The magnetic nature of solar flares. *Astron. Astrophs. Rev.*, 10:313–377.
- [Pritchett, 2001] Pritchett, P. L. (2001). Geospace environmental modeling magnetic reconnection challenge: simulations with a full particle electromagnetic code. *J. Geophys. Res.*, 106:3783.
- [Pritchett and Coroniti, 2004] Pritchett, P. L. and Coroniti, F. V. (2004). Three-dimensional collisionless magnetic reconnection in the presence of a guide field. *J. Geophys. Res.*, 109:1220,doi10.1029/2003JA009999.
- [Quataert, 2006] Quataert, E. (2006). Accretion disk plasma physics. Lecture notes, CMPD & CMSO Winter School.
- [Ren et al., 2005] Ren, Y., Yamada, M., Gerhardt, S., Ji, H., Kulsrud, R., and Kuritsyn, A. (2005). Experimental verification of the hall effect during magnetic reconnection in a laboratory plasma. *Phys. Rev. Lett.*, 95(5):005003.
- [Ricci et al., 2004] Ricci, P., Brackbill, J. U., Daughton, W., and Lapenta, G. (2004). Collisionless magnetic reconnection in the presence of a guide field. *Phys. Plasmas*, 11(8):4102–4114.
- [Ricci et al., 2002] Ricci, P., Lapenta, G., and Brackbill, J. U. (doi: 10.1029/2002GL015314, 2002). Gem reconnection challenge: Implicit kinetic simulations with the physical mass ratio. *Geophys. Res. Lett.*, 29(23):2088.
- [Rogers and Zakharov, 1995] Rogers, B. and Zakharov, L. (1995). Nonlinear ω_* stabilization of the $m=1$ mode in tokamaks. *Phys. of Plasmas*, 2:3420.
- [Rogers et al., 2001] Rogers, B. N., Denton, R. E., Drake, J. F., and Shay, M. A. (2001). Role of dispersive waves in collisionless magnetic reconnection. *Phys. Rev. Lett.*, 87(19):195004.
- [Rossi and Olbert, 1970] Rossi, B. and Olbert, S. (1970). *Introduction to the Physics of Space*. McGraw-Hill Book Company.
- [Runov et al., 2003] Runov, A., Nakamura, R., Baumjohann, W., Treumann, R. A., Zhang, T. L., Volwerk, M., Vörös, Z., Balogh, A., Glabmeier, K.-H., Klecker, B., Réme, H., and Kistler, L. (doi: 10.1029/2002GL016730, 2003). Current sheet structure near magnetic x-line observed by cluster. *Geophys. Res. Lett.*, 30(11):1579.
- [Sato and Hayashi, 1979] Sato, T. and Hayashi, T. (1979). Externally driven magnetic reconnection and a powerful magnetic energy converter. *Phys. Fluids*, 22:1189.

- [Scholer, 1989] Scholer, M. (1989). Undriven magnetic reconnection in an isolated current sheet. *J. Geophys. Res.*, 94(A7):8805–8812.
- [Scudder et al., 2002] Scudder, J. D., Mozer, F. S., Maynard, N. C., Puhl-quinn, P. A., Ma, Z. W., and Russell, C. T. (2002). Fingerprints of collisionless reconnection i: Evidence for hall mhd scales. *J. Geophys. Res.*, 107, doi:10.1029/2001JA000126:2002.
- [Shay, 1998] Shay, M. A. (1998). *The Dynamics of Collisionless Magnetic Reconnection*. PhD thesis, University of Maryland-College Park.
- [Shay and Drake, 1998] Shay, M. A. and Drake, J. F. (1998). The role of electron dissipation on the rate of collisionless magnetic reconnection. *Geophys. Res. Lett.*, 25:3759.
- [Shay et al., 1998] Shay, M. A., Drake, J. F., Denton, R. E., and Biskamp, D. (1998). Structure of the dissipation region during collisionless magnetic reconnection. *J. Geophys. Res.*, 25:9165.
- [Shay et al., 1999] Shay, M. A., Drake, J. F., Rogers, B. N., and Denton, R. E. (1999). The scaling of collisionless, magnetic reconnection for large systems. *Geophys. Res. Lett.*, 26:2163.
- [Shay et al., 2001] Shay, M. A., Drake, J. F., Rogers, B. N., and Denton, R. E. (2001). Alfvénic collisionless reconnection and the Hall term. *J. Geophys. Res.*, 106:3751.
- [Shay et al., 2006] Shay, M. A., Drake, J. F., and Swisdak, M. (2006). Private communication.
- [Shay et al., 2004] Shay, M. A., Drake, J. F., Swisdak, M., and Rogers, B. N. (2004). The scaling of embedded collisionless reconnection. *Phys. Plasmas*, 11(5):2199.
- [Skufca et al., 2005] Skufca, J. D., Yorke, J. A., and Eckhardt, B. (2005). The edge of chaos in a parallel shear flow. *Phys. Rev. Lett.*
- [Sonnerup, 1979] Sonnerup, B. U. Ö. (1979). Magnetic field reconnection. In Lanzetta, L. J., Kennel, C. F., and Parker, E. N., editors, *Solar System Plasma Physics*, volume 3, page 46. North Holland Pub., Amsterdam.
- [Strogatz, 1994] Strogatz, S. H. (1994). *Nonlinear Dynamics and Chaos*. Addison-Wesley Publishing Company.
- [Sullivan et al., 2005] Sullivan, B. P., Rogers, B. N., and Shay, M. A. (2005). The scaling of forced collisionless reconnection. *Phys. Plasmas*, 12:122312.
- [Sweet, 1958] Sweet, P. A. (1958). The neutral point theory of solar flares. In Lehnert, B., editor, *Electromagnetic Phenomena in Cosmical Physics*, page 123. Cambridge University Press, New York.

- [Swisdak et al., 2005] Swisdak, M., Drake, J. F., Shay, M. A., and McIlhargey, J. G. (2005). The transition from antiparallel to component magnetic reconnection. *J. Geophys. Res.*, 110:A05210.
- [Swisdak et al., 2003] Swisdak, M., Drake, J. F., Shay, M. A., and Rogers, B. N. (2003). Diamagnetic suppression of component magnetic reconnection at the magnetopause. *J. Geophys. Res.*, 108(A5):1218.
- [Tanaka, 1996] Tanaka, M. (1996). Asymmetry and thermal effects due to parallel motion of electrons in collisionless magnetic reconnection. *Phys. Plasmas*, 3:4010.
- [Terasawa, 1983] Terasawa, T. (1983). Hall current effect on tearing mode instability. *Geophys. Res. Lett.*, 10:475.
- [Trintchouk et al., 2003] Trintchouk, F., Yamada, M., Ji, H., Kulsrud, R. M., and Carter, T. A. (2003). Measurement of the transverse spitzer resistivity during collisional magnetic reconnection. *Phys. Plasmas*, 10(1):319–322.
- [ud Doula et al., 2006] ud Doula, A., Townsend, R. H. D., and Owocki, S. P. (2006). Centrifugal breakout of magnetically confined line-driven stellar winds. *Ap. J.*, 640:L191–L194.
- [Ugai and Tsuda, 1977] Ugai, M. and Tsuda, T. (1977). Magnetic field line reconnection by localized enhancement of resistivity, 1, evolution in a compressible mhd fluid. *J. Plasma Phys.*, 17:337.
- [Uzdensky and Kulsrud, 2000] Uzdensky, D. A. and Kulsrud, R. M. (2000). Two-dimensional numerical simulation of the resistive reconnection layer. *Phys. Plasmas*, 7(10):4018.
- [Vasyliunas, 1975] Vasyliunas, V. M. (1975). Theoretical models of magnetic field line merging, 1. *Rev. Geophys.*, 13(1):303.
- [von Goeler et al., 1974] von Goeler, S., Stodiek, W., and Sautoff, N. R. (1974). Studies of internal disruptions and $m=1$ oscillations in tokamak discharges with soft-x-ray techniques. *Phys. Rev. Lett.*, 33:1201.
- [Wang et al., 2000] Wang, X., Bhattacharjee, A., and Ma, Z. W. (2000). Collisionless reconnection: Effects of Hall current and electron pressure gradient. *J. Geophys. Res.*, 105(A12):27633–27648.
- [Wang et al., 2001] Wang, X., Bhattacharjee, A., and Ma, Z. W. (2001). Scaling of collisionless forced reconnection. *Phys. Rev. Lett.*, 87(26):265003.
- [Wheatland, 2000] Wheatland, M. S. (2000). The origin of the solar flare waiting-time distribution. *Ap. J.*, 536:L109–L112.
- [White, 1986] White, R. B. (1986). Resistive reconnection. *Reviews of Modern Physics*, 58(1):183–207.

- [White et al., 2003] White, S. M., Krucker, S., Shibasaki, K., Yokoyama, T., Shimajo, M., and Kundu, M. R. (2003). Radio and hard x-ray images of high-energy electrons in an x-class solar flare. *Ap. J.*, 595:L111–L114.
- [Yamada et al., 1994] Yamada, M., Levinton, F. M., Pomphrey, N., Budny, R., Manickam, J., and Nagayama, Y. (1994). Investigation of magnetic reconnection during a sawtooth crash in a high-temperature tokamak plasma. *Phys. Plasmas*, 1:3269–3276.
- [Yamada et al., 2006] Yamada, M., Ren, Y., Ji, H., Breslau, J., Gerhardt, S., Kulsrud, R., and Kuritsyn, A. (2006). Experimental study of two-fluid effects on magnetic reconnection in a laboratory plasma with variable collisionality. *Phys. Plasmas*, 13:052119.
- [Zalesak, 1979] Zalesak, S. T. (1979). Fully multidimensional flux-corrected transport algorithms for fluids. *J. Comput. Phys.*, 31:335–362.
- [Zweibel, 2006] Zweibel, E. (2006). Reconnection in astrophysics: The interstellar medium. Lecture notes, CMPD & CMSO Winter School.